

Rheinisch-Westfälische Technische Hochschule Aachen
Institut für Eisenhüttenkunde

- Werkstoff- und Bauteilintegrität -

Masterarbeit

des

cand.ing. Yao Yao

Matr.-Nr. 374161

Thema: Experimentelle und numerische Studie zu
Großeneffekten bei der Nanoindentation

*Topic: Experimental and numerical study on size effects in
Nanoindentation*

Durchgeführt in der Abteilung Schädigungstoleranz
vom 01.07.2019 bis 16.12.2019

Betreuer: Univ. Prof. Dr.-Ing. Sebastian Münstermann
Dr. Ude Hangen
M.Sc. Michael Dölz
M.Sc. Wensi Liu

Hiermit versichere ich, dass ich die vorliegende Arbeit selbstständig verfasst habe und keine anderen als die angegebenen Quellen und Hilfsmittel benutzt habe, sowie Zitate kenntlich gemacht habe.

cand.-ing. Yao Yao

Hiermit erlaube ich, dass meine Arbeit nach der Abgabe durch weitere Personen als meine Prüfer eingesehen werden darf.

cand.-ing. Yao Yao

Abstract	1
1 Introduction and aim	2
2 Theoretical background	4
2.1 Nanoindentation	4
2.1.1 Indenter tips	5
2.1.2 Load Displacement Curve	6
2.1.3 Test errors	9
2.1.3.1 Thermal drift	9
2.1.3.2 Instrument compliance	10
2.1.3.3 Pile-up and sink-in	10
2.1.3.4 Sample roughness	12
2.1.4 Scanning Probe Microscope	12
2.2 Indentation size effect	13
2.2.1 Introduction	13
2.2.2 Theory	15
2.3 Crystal Plasticity Finite Element Modelling	19
2.3.1 Overview	19
2.3.2 Local model	21
2.3.2.1 Dislocation slip controlled plasticity	21
2.3.2.2 Flow kinematics	22
2.3.2.3 Phenomenological constitutive laws	24
2.3.3 Non-local model	25
2.3.4 Crystal plasticity models in nanoindentation	26
3 Material	28
3.1 Chemical composition	28
3.2 Microstructure	28
3.3 Mechanical properties	31
4 Nanoindentation test	32
4.1 Sample preparation and test setup	32
4.2 Loading function	34

4.3 Experiment program	37
5 Size effect in nanoindentation tests	41
5.1 Load-displacement curve	41
5.2 Pile-up	52
5.3 Hardness	60
6 Size effect study with crystal plasticity models	63
6.1 Simulation setup.....	63
6.2 Local model	65
6.2.1 Parameterization.....	65
6.2.2 Validation	72
6.2.3 Formulation.....	76
6.3 Non-local model.....	77
7 Conclusions.....	80
Appendices	I
Literature.....	II

Abstract

Nanoindentation has been developed into a mature tool to measure the mechanical properties of materials at small length scales. The indentation size effects (ISE) in different indenter types leads to the validation problems of experiment results. In order to investigate the ISE of spherical indenters, a series of nanoindentation tests with indenters of the different radius (1, 2, 5, 20 μm) on a cold-rolled ferritic stainless steel (AISI 439) sheet are performed. For each tip, three groups of tests with indentation strain of 0.2, 0.3 and 0.4 are conducted. Grains with crystallographic orientations close to [100], [111], in the normal direction the inverse pole figure on the [100]-[110]-[111] unit triangle are selected. The load-displacement curves and the surface topographies are recorded, and the hardness value is analyzed as well. A local crystal plasticity (CP) model is used for the numerical study of indentation tests. The CP parameter, initial critical resolved shear stress (τ_0), is varied for different indenter radius to fit the load-displacement curves and pile-up patterns from experiments.

The nanoindentation experiment results show a prominent size effect, where the hardness increases with decreasing indenter radius. The slight decrease of hardness with increasing indentation strain for the same indenter indicates the ISE as well. The increase in τ_0 with decreasing indenter radius after calibration in the local model shows the same trend with the hardness results from experiments, which proves the ISE can be captured by adjusting τ_0 . The relationship of the indenter radius and τ_0 is given by a Boltzmann equation.

1 Introduction and aim

Nanoindentation is the leading technique for evaluating the mechanical properties of materials at micrometer and nanometer length scales. It can extract hardness and modulus value of the interested areas with high accuracy and effectiveness. In addition, as the penetration load and depth are relatively small, which is nondestructive to the surface, nanoindentation tests have been widely used in bulk materials and thin films. However, during nanoindentation tests, diverse errors can appear, which affect the validity of the results. Indentation size effect (ISE) is one kind of errors that attracts great interest. It is found that the measured hardness increases with decreasing penetration depth for the pyramid and conical indenter. As for spherical indenter, the ISE is related to the indenter radius in the way that smaller radius leading to higher hardness.

Various phenomenological models have been developed to explain the ISE. Fleck and Hutchinson have introduced a material length scale in their model to describe the strain gradient plasticity [1]. Nix and Gao [2] take the geometrically necessary dislocations (GND) that originated from the strain gradient into account for the conical indenter. Swadener [3] has extended the Nix-Gao Model to the spherical indenter. Huang et al. [4] have captured the ISE at a very small depth by introducing a maximum allowable GND density.

The crystal plasticity finite element modeling (CPFEM) has been widely utilized to predict the mechanical behavior of single- and polycrystalline metals at micro and mesoscale. By incorporating phenomenological models with various constitutive formulations, CPFEM is able to study the stress-strain relationship, texture evolution, phase transformation, damage initiation, etc. However, for a standard local model, it fails to describe the size effect problems as the strain gradient is not considered. To capture the size effects, various non-local models are developed, which take variables that related to strain gradient or dislocation densities into account.

The aim of this work is to study the ISE with spherical indenters in both experimental and numerical methods. First, nanoindentation tests are performed on a ferritic

stainless steel AISI 439 using four spherical indenters with the radii of 1, 2, 5 and 20 μm . For the spherical indenter, the hardness value is comparable under the same indentation strain, a/R , where a is the radius of the circle of contact and R is the indenter radius. Indentation tests with the strain of 0.2, 0.3 and 0.4 are performed for each indenter respectively.

A numerical simulation of ISE is proposed with a local CP model. The parameterization of crystal parameters is achieved by comparing the load-displacement curves and surface topography of the experiment and simulation results. In order to reflect the ISE, the initial critical resolved shear stress, τ_0 is adapted for different indenters. The variety of τ_0 is reasonable, as ISE is directly related to GNDs, which influence the shear strength of materials. After parameter calibration, the change of τ_0 is supposed to have a relationship with the indenter radius.

2 Theoretical background

2.1 Nanoindentation

For more than a century, researchers in the mechanical sciences have recognized that surface contacts between materials are highly dependent on their mechanical properties. Many different indentation and impression tests have been developed in an effort to measure such mechanical properties from a contact with known geometry. In the past two decades, a veritable revolution has occurred in indentation testing, owing to the development of new sensors and actuators that allow instrumented indentations to be routinely performed on submicron scales [5]. The resulting technique, termed nanoindentation, has now attracted considerable interest in the mechanical characterization of materials with various indenters, especially for thin film systems and small volumes of materials.

Usually, the principal goal of the nanoindentation test is to obtain elastic modulus and hardness of the specimen material from experimental readings of indenter load and depth of penetration. The forces involved are usually in the millinewton range and are measured with a resolution of a few nano newtons. The depths of penetration are in the order of nanometers, hence the term ‘nanoindentation’. In addition to the extraction of elastic modulus and hardness of materials, nanoindentation techniques can also be used to obtain strain hardening exponent, fracture toughness and viscoelastic properties. Besides tests on bulk materials, one of the most popular applications of nanoindentation is the determination of the mechanical properties of thin films. Comparing to other techniques, the properties of the film may be measured without removing the film from the substrate in nanoindentation. The spatial distribution of properties, in both lateral and depth dimensions, can be measured [6].

The principal components in a nanoindentation experiment are the test material, the mechanical load and indenter displacement which can be measured by the sensors, actuators, and indenter tips.

2.1.1 Indenter tips

As the core part of nanoindentation tests, the material properties and geometry of indenter tips have a great influence on the testing results. Normally the diamond is used for indenter tip due to its high hardness which can be regarded as a rigid body during the test. The probe types include Vickers, Berkovich, cube corner, conical and spherical-conical indenters, which are shown in Fig. 2.1 [7].

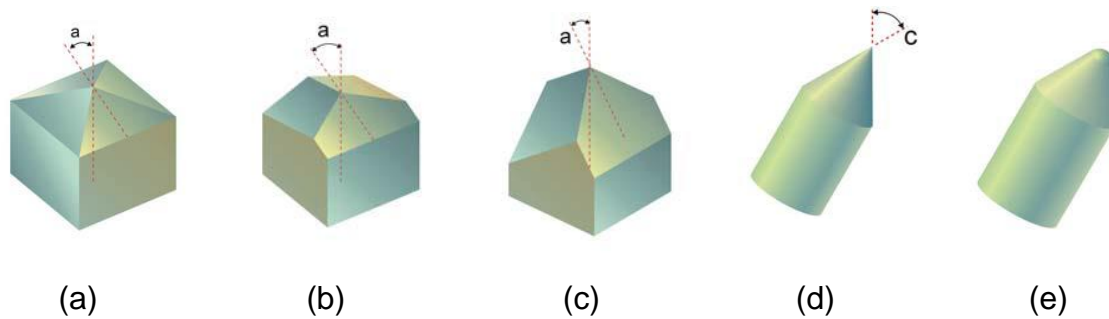


Fig. 2.1 Indenter types: (a) Vickers indenter (b) Berkovich indenter (c) Cube corner indenter (d) Conical indenter (e) Spherical-conical indenter [7].

The Vickers tip is a four-sided pyramid with a centerline-to-face angle (a as shown in Fig. 2.1) of 68° . It is suitable for bulk materials, films and foils. The Berkovich tip is a three-sided pyramid. The angle between the centerline and the three faces is 65.3° . The three-face design allows grinding the tip to a sharp point. It is suitable for bulk materials, thin films, polymers, scratch testing, wear testing, and imaging. As the name implies, the cube corner is a three-sided pyramidal tip with perpendicular faces like the corner of a cube. The centerline-to-face angle is 35.3° . It is much sharper compared to the Berkovich tip, which is suitable for thin film, scratch testing, fracture toughness, wear testing. Conical indenter possesses axial symmetry, the conical angle (c) varies from 20° to 140° . It excludes the tip geometry effect during the deformation of materials around the indenter, e.g. pile-up structure development. Spherical-conical indenter provides a smooth transition from elastic to elastic-plastic contact, which is particularly suitable for testing on soft materials.

2.1.2 Load Displacement Curve

Nanoindentation is widely used to extract elastic modulus and hardness of the specimen. These properties are obtained from the indenter load and depth of penetration during one cycle of loading and unloading.

A schematic representation of a typical data set obtained with a Berkovich indenter is presented in Fig. 2.2, where the parameter P designates the load and h is the displacement relative to the initial undeformed surface. There are three important quantities that must be measured from the P-h curves: the maximum load P_{\max} , the maximum displacement, h_{\max} , and the elastic unloading stiffness S , defined as the slope of the upper portion of the unloading curve during the initial stages of unloading. Another important quantity is the final depth h_f , the permanent depth of penetration after the indenter is fully unloaded.

The hardness H , which is also referred to as the mean contact pressure, is given by the indenter load divided by the contact area A as:

$$H = \frac{P_{\max}}{A} \quad \text{Eq. 2.1}$$

Experiments have shown that unloading curves are distinctly curved and usually well approximated by the power law relation:

$$P = \alpha(h - h_f)^m \quad \text{Eq. 2.2}$$

where α and m are power law fitting constants and can be obtained from unload fitting curve.

Measurement of the elastic modulus follows from its relationship to contact area and the measured unloading stiffness through the relation:

$$S = \frac{dP}{dh} = \frac{2}{\sqrt{\pi}} E_r \sqrt{A} \quad \text{Eq. 2.3}$$

where E_r is the reduced modulus, which has a relationship with elastic modulus by:

$$\frac{1}{E_r} = \frac{1-\nu^2}{E} + \frac{1-\nu_i^2}{E_i} \quad \text{Eq. 2.4}$$

where E and ν are Young's modulus and Poisson's ratio of the specimen and E_i and ν_i are Young's modulus and Poisson's ratio of the indenter respectively.

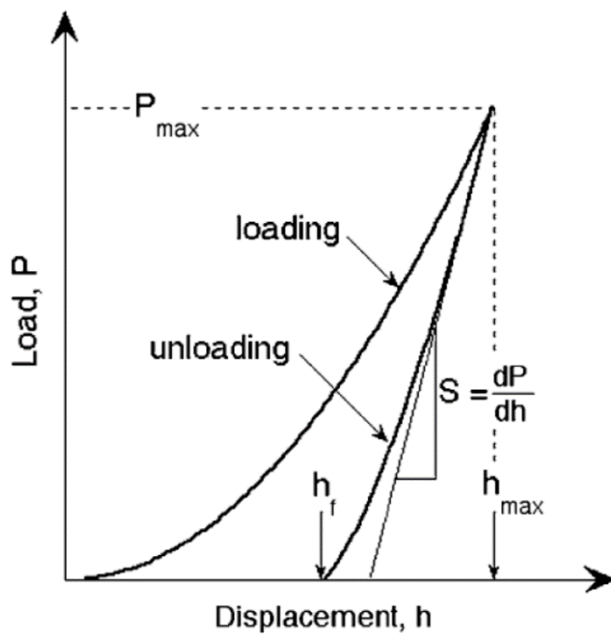


Fig. 2.2 Schematic illustration of indentation load–displacement data showing important measured parameters [8].

Fig. 2.3 illustrates the parameters during unloading process of indenter which characterizing the contact geometry. The contact depth between the indenter and the specimen is:

$$h_c = h_{max} - h_s = \epsilon \frac{P_{max}}{S} \quad \text{Eq. 2.5}$$

where h_s shows the amount of sink-in and ϵ is a constant that depends on the geometry of the indenter.

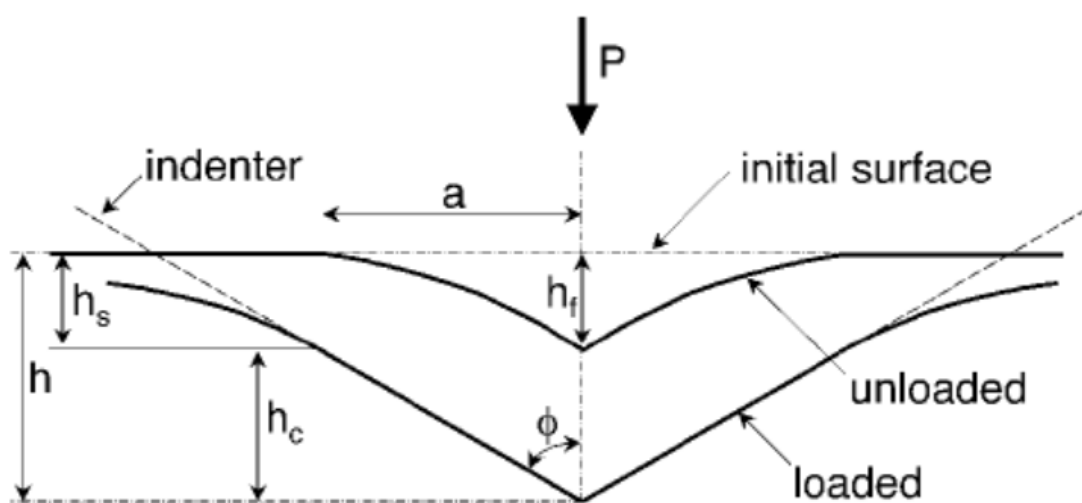


Fig. 2.3 Schematic illustration of geometrical parameters during unloading process [9].

The contact area is related to the contact depth h_c which can be calculated according to the geometry of the indenter.

For Berkovich Indenter, the projected area is given by:

$$A=24.5 h_c^2 \quad \text{Eq. 2.6}$$

For cube corner indenter,

$$A=2.598 h_c^2 \quad \text{Eq. 2.7}$$

For a spherical indenter with indenter radius R , as shown in Fig. 2.4, the radius of the circle of contact is given by:

$$a = \sqrt{2Rh_c - h_c^2} \approx \sqrt{2Rh_c} \quad \text{Eq. 2.8}$$

The contact depth can be calculated by:

$$h_c = (h_{\max} + h_p)/2 \quad \text{Eq. 2.9}$$

Where h_p is the residual depth of the impression after unloading.

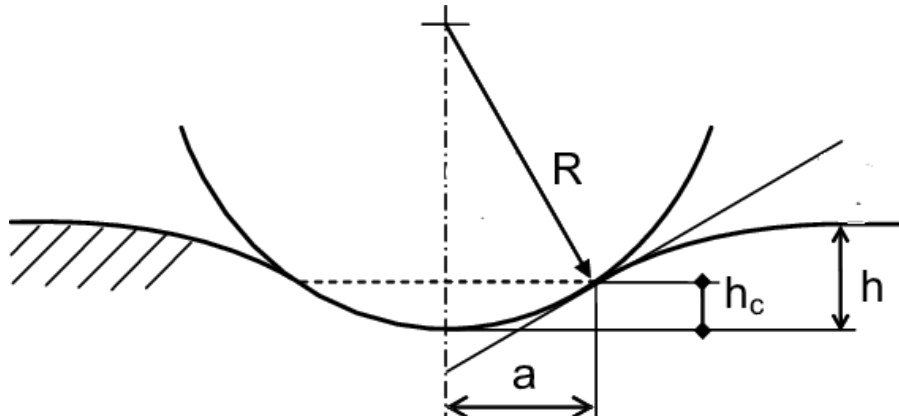


Fig. 2.4 Schematic illustration of geometrical parameters of spherical indenter [10].

In nanoindentation tests, the discontinuities in the load-displacement curves are commonly observed. Generally, there are two kinds of discontinuities as illustrated in Fig. 2.5. The first one is a sudden displacement excursion into the target materials during the load-controlled nanoindentation tests. The second type of discontinuity is a 'load drop' found during a displacement-controlled experiment. This phoneme, which is called 'pop-in' event, can be explained by the dislocation nucleation, or the sudden

onset of plasticity, which indicates the transition from pure elastic deformation to plastic-elastic deformation.

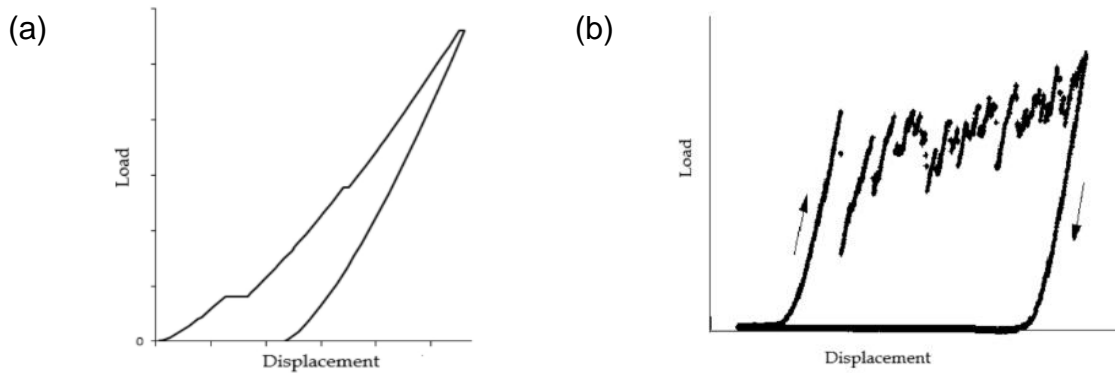


Fig. 2.5 Pop-in in (a) Load-controlled indentation test; (b) displacement controlled indentation test [11].

The pop-in events are also caused by cracks formation around indents or phase transformation. For a hard brittle film on an elastic-plastic substrate, the rupture can lead to the pop-in as well. The pop-in events are function of the indenter shape [12, 13], the temperature [14] and the strain rate [15].

2.1.3 Test errors

In conventional indentation tests, the area of contact at maximum load is usually calculated from the size of residual impressions after unload, which neglect the elastic recovery. During nanoindentation tests, the elastic recovery is significant at nanoscale, which cannot neglect. To determine the contact area of indents, it is usual to measure the load and depth of penetration during loading and unloading, and various errors are associated with this procedure. In addition to the above, there are several materials related issues that affect the validity of the results.

2.1.3.1 Thermal drift

During the nanoindentation tests, both specimens and instruments can experience drift behavior, which can influence the result of displacement. The dimensions of the

instrument can change due to thermal expansion or contraction caused by the temperature change of the environment. For specimen, the creep within the material as a result of plastic flow happens when the load is held constant.

If the rate of change of displacement recording with time is measured at some point during the indentation test, for example at the beginning of test or at the end of the unloading where there is no displacement of test material, then the thermal drift of instrument can be calculated and the following depth reading procedure can be corrected.

2.1.3.2 Instrument compliance

The results of measurement are influenced to some extent by the compliance of the device. The force acting on the indenter causes not only its penetration into the specimen, but also the deformation of the indenter shaft, the specimen holder and other parts of the device, all denoted together as the instrument frame. The total measured compliance C , the compliance of specimen C_s and the instrument frame C_f has a relationship:

$$C = C_s + C_f \quad \text{Eq. 2.9}$$

Since the specimen compliance during elastic contact is the inverse of contact stiffness, combining Eq. 2.3 and Eq. 2.9 to yield:

$$C = C_f + \frac{\sqrt{\pi}}{2E_r} \frac{1}{\sqrt{A}} \quad \text{Eq. 2.10}$$

when the modulus is constant, the C vs $A^{1/2}$ is linear and the intercept of the line can be used to calculate the instrument frame. Thus, to calculate the instrument compliance C_f , a series of indents with different penetration depths are performed in the standard sample whose elastic modulus is known [6].

2.1.3.3 Pile-up and sink-in

When the contact between Indenter and material involves plastic deformation during the indentation test, the material may either sink-in or pile-up around the indenter (as shown in Fig. 2.6). If the pile-up occurs, the actual contact area is larger than the

apparent values, and the material seems to be stiffer. If no correction for pile-up is done, the calculated hardness and elastic modulus are higher than the real value. For sink-in behavior, the inverse results occur.

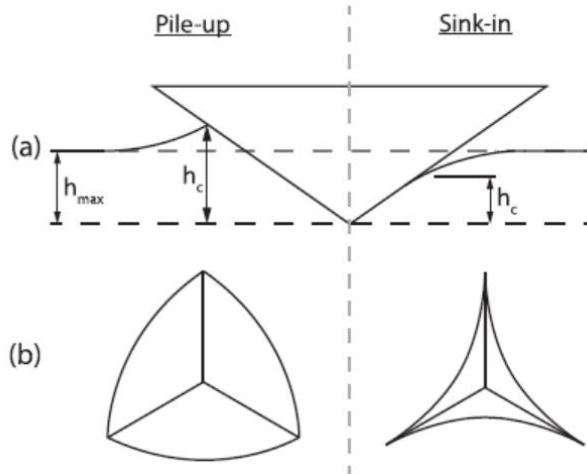


Fig. 2.6 Pile-up and sink-in behavior (a) side profile of indentation, (b) geometry of projected contact areas of each case [16].

The pile-up and sink-in behavior are dependent on the ratio of elastic modulus and yield strength of the material E/Y . For non-strain-hardening materials with a large value of E/Y , a big plastic zone is observed, since most of the plastic deformation occurs in the near indenter, which could be displaced by plastic flow upwards, the pile-up is expected to happen. For materials with low E/Y , the plastic zone is small and contained within the boundary of the contact circle, the volume of the material displaced by the indenter can be accommodated by the elastic deformations of the material around, sink-in is more likely to happen [17]. For materials exhibit strain-hardening, the yield stress increases during plastic deforming. The intensively deformed surface layer around the indenter becomes harder and constrains the upward flow of the material, the pile-up is not likely to happen.

2.1.3.4 Sample roughness

The overall effect of surface roughness is to reduce the mean contact pressure due to an increase in contact radius. Thus, the penetration depth is decreased under a given load.

Surface roughness can be quantified by a roughness parameter α by [18]:

$$\alpha = \frac{\sigma_s R}{a_0^2} \quad \text{Eq. 2.11}$$

where σ_s is equal to the maximum asperity height, R is the indenter radius and a_0 is the contact radius that under the same load for smooth surfaces. It can be seen from Eq. 2.11 that the roughness parameter increases with larger indenter radius and smaller size of the contact circle. Therefore, the roughness effect is significant at the beginning of loading process with blunt indenters. For sharper indenter, the effects of surface roughness are less severe. Before nanoindentation tests, the sample should be well prepared by metallurgical methods to reach the acquired surface roughness.

2.1.4 Scanning Probe Microscope

For nanoindentation technique, detection of the surface roughness before tests is essential. Atomic force microscope (AFM) has been widely used for the characterization of surface topography. In recent years, a new method has been developed that allows surface scanning directly using the nanoindentation machine. In-situ Scanning probe microscope (SPM) utilizes the same probe that used to perform tests to image the sample surface, allowing images to be quickly gathered on-site without leaving the test location. SPM imaging provides high-resolution sample surface topography images and test positioning accuracy at the scale of nanometer, which increases the reliability, efficiency and repeatability of nanomechanical tests. Sample roughness can be calculated according to the images. Additionally, post-test SPM imaging provides a quantitative characterization of material deformation behavior (fracture, pile-up, etc.) and verification of the test position.

The SPM imaging is realized by the combination work of tip, transducer and piezo scanner (as shown in Fig. 2.7). The tip moves along the sample surface with a pre-

defined contact force between tip and surface. The X-Y piezo drives the probe over the sample surface, while the Z displacement of the piezo is utilized to maintain a constant imaging force, and the topology signal is recorded by the scanner. The instrument supplies a maximal scan image resolution at 2048×2048 pixels. The scan size, which depends on the properties of the piezo scanner, can reach up to 100 by 100 μm . The scan rate determines the speed of the scanned image and is changeable from 0.01 Hz up to 12 Hz. Slower scan rates will offer less image distortion while higher scan rates may cause noise or artifacts depending on the sample.

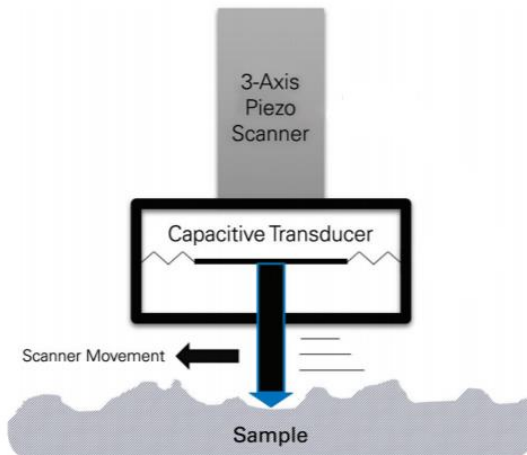


Fig. 2.7 The schematic illustrates the basic principles of SPM [19].

2.2 Indentation size effect

2.2.1 Introduction

In materials science, effects of size on mechanical properties of materials are always of great interest. At scales of specimen dimensions, no size effect is observed. However, at smaller scales, the size-dependent mechanical properties are observed in experiments, e.g. the Hall-Patch effect [20] and the size-dependent strength of torsion tests of thin wires [1]. These plasticity phenomena display a size effect that the smaller is the size the stronger is the response.

In indentation tests, it is expected to have only one value of hardness in a homogeneous, isotropic material. With a pyramidal or conical indenter, the ratio of the

length of the diagonal or radius of contact to the depth of the indentation, a/δ remains constant despite the load P , as shown in Fig. 2.8. Indentations of this type are called ‘geometrical similarity’, which the strain within the material is constant, independent of the load. As for spherical indents, the ratio a/δ increases with increasing load, indentations in this case are not geometrically similar. However, geometrically similar indentations can be obtained with spherical indenters of different radii when the ratio of the radius of circle of contact to the indenter radius, a/R , also referred to indentation strain, is maintained constant. In this case, the mean contact pressure or hardness stays constant.

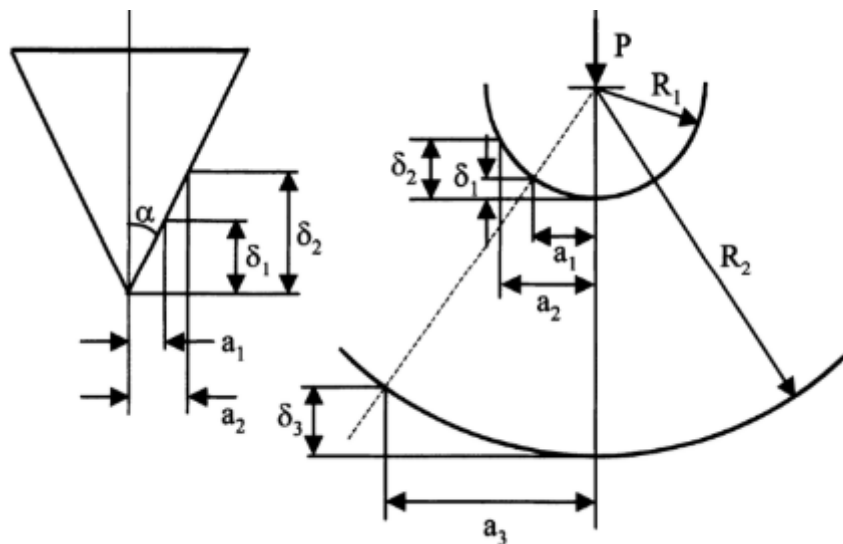


Fig. 2.8 Geometrical similarity for (a) pyramid or conical indenter (b) spherical indenter [6].

However, experimental results often give a variety of hardness in an isotropic material, even if other effects mentioned in 2.1.2 are minimized. Much of the early work has shown a greater increase in hardness with decreasing penetration depth (as shown in Fig. 2.9) measured by pyramid indenters on metals [21, 22]. This so-called indentation size effect (ISE) becomes observable for penetration depth smaller than several micrometers. ISE can also appear in spherical indenter. This is demonstrated by Swadener et al. [3], who conducted indentation experiments on an Ir alloy specimen with a series of spherical indenters ranging in size from 14 μm to 1600 μm . As spherical

indenter has no self-similarity, the hardness is plotted with as a function of indentation strain a/R . It can be observed that as the radius of the indenter decreases, the hardness increases (as shown in Fig. 2.10). In this case, smaller is stronger once again, but smaller refers to the radius of the sphere rather than to the depth of penetration.

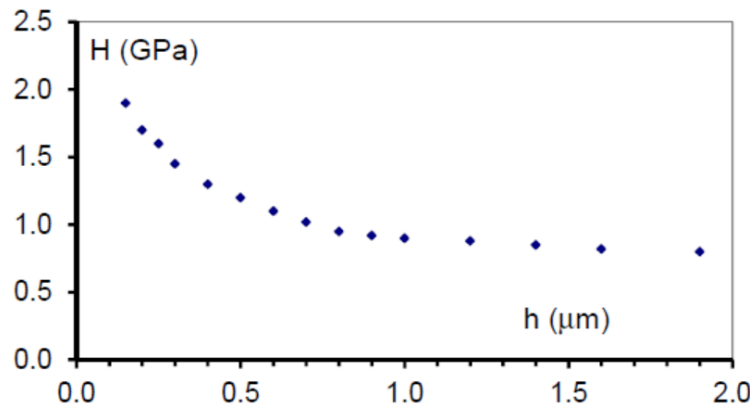


Fig. 2.9 Depth dependence of hardness of a single crystal copper [2].

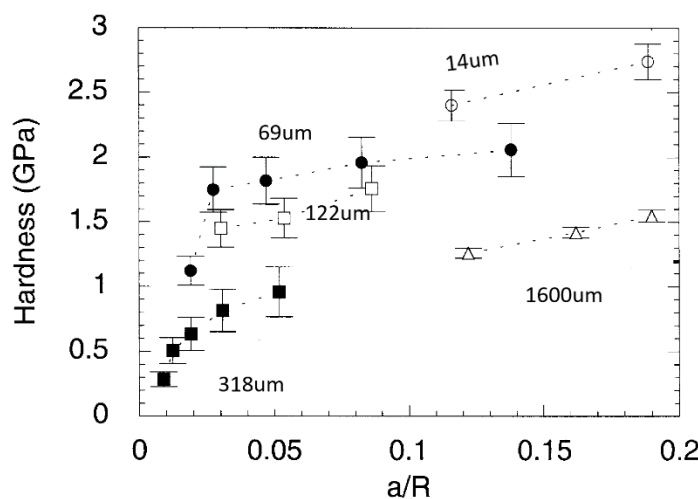


Fig. 2.10 Variation of hardness in annealed Ir sample with a/R for spherical indenters [3].

2.2.2 Theory

Conventional plasticity theory is built based on the motion of dislocations and associated activated slip systems. In such theory, the plasticity flow at one certain point is uniquely related to the strain at that point and has no relation to strain gradient, which

makes it difficult to explain the ISE on crystalline materials as Fleck et al. [23] have pointed out that the ISE can be understood by taking the large strain gradients inherent in small indentations into account.

Fleck and Hutchinson [23] developed a strain gradient plasticity model by introducing a material length scale into a phenomenological model. By considering the geometrically necessary dislocations (GND) that originated from the strain gradient generated by a conical indenter, Nix and Gao [2] developed a model that matches the indentation test results. The Nix and Gao model assumes that dislocation loops are generated below the deformed surface during penetration of indenters. These dislocation loops lie under an approximately hemispherical volume below the region in contact, as shown in Fig. 2.11. The material originally sitting in the indent region are pushed into the underneath substrate material and store as geometrically necessary dislocations.

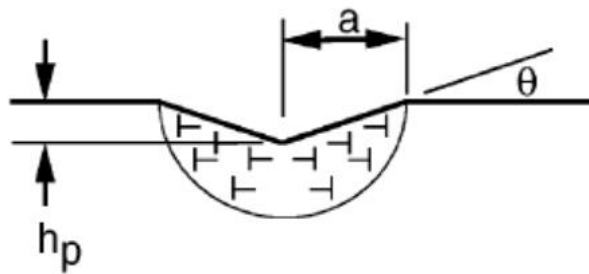


Fig. 2.11 Geometrical necessary dislocations under a conical indenter [3].

For a self-similar conical indenter, the angle between the surface and the indenter θ stays constant as:

$$\tan\theta = \frac{h_p}{a} \quad \text{Eq. 2.12}$$

where h_p is the penetration depth, a is the contact radius. The number of geometrical necessary dislocations loops is then h_p/b , where b is the Burger's vector. The total length of all the dislocations loops is:

$$\lambda = \pi h_p a / b \quad \text{Eq. 2.13}$$

The model assumes that the dislocations are distributed uniformly under a hemispherical volume with volume of:

$$V = 2\pi a^3 / 3 \quad \text{Eq. 2.14}$$

Therefore, the density of the dislocations is:

$$\rho_G = \frac{\lambda}{V} = \frac{3}{2bh_p} \tan^2 \theta \quad \text{Eq. 2.15}$$

According to Taylor relation, the shear strength is related to the density of geometrical necessary dislocations and statistically stored dislocations by:

$$\tau = \alpha \mu b \sqrt{\rho} = \alpha \mu b \sqrt{\rho_G + \rho_S} \quad \text{Eq. 2.16}$$

Where α is the geometric constant, μ is the shear modulus, τ is the shear strength and ρ_S is the statistically stored dislocations density.

Assuming the flow stress is related to the shear strength by the Mises flow rule:

$$\sigma = \sqrt{3}\tau \quad \text{Eq. 2.17}$$

and the hardness is related to flow stress by the Tabor factor [24] :

$$H = 3\sigma \quad \text{Eq. 2.18}$$

Combining Eq. 2.12 to Eq. 2.18, the model gives the relationship between the hardness and the depth as:

$$H = H_0 \sqrt{1 + \frac{h^*}{h_p}} \quad \text{Eq. 2.19}$$

Where $H_0 = 3\sqrt{3}\alpha\mu b \sqrt{\rho_S}$ is the macroscopic hardness of material, and $h^* = \frac{81}{2} \alpha^2 b \tan^2 \left(\frac{\mu}{H_0} \right)$ is the length scale for the depth dependence of hardness.

As for spherical indenters, the ISE is manifested not through the depth of penetration but rather through the radius of the sphere, Swadener derived an expression according to the Nix-Gao Model by modifying the geometry of spherical contact but leaving the other assumptions the same, which is:

$$H = H_0 \sqrt{1 + \frac{R^*}{R}} \quad \text{Eq. 2.20}$$

H_0 is defined the same as before, the length scale of depth h^* is replaced by a characteristic radius R^* , where $R^* = 1/b\rho_S$. R is the indenter radius. This expression

has been proved being able to match the experiments results of indentation tests with spherical indenters [3].

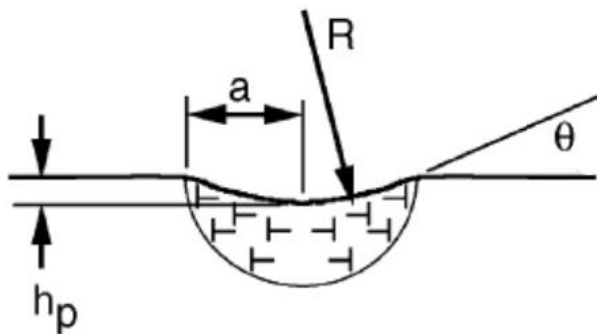


Fig. 2.12 Geometrical necessary dislocations under a spherical indenter [3].

Huang et al. [25] established a conventional theory of mechanism-based strain gradient plasticity (CMSG) to model size effects observed in indentation tests. A strain gradient term is included into the constitutive model based on the Nix-Gao mechanistic framework. The basic material input needed to implement the model is the macroscopic tensile stress-strain curve. Predictions of the model assuming a Taylor hardening coefficient $\alpha=1/3$ are included. The theory results show generally good agreement between theory and experiment (as illustrated in Fig. 2.13), with the exception of the smallest indenter, $R= 14 \mu\text{m}$, for which the model significantly overestimates the experimental observations. Although Nix-Gao model has been confirmed for a wide range of indentation depths, this observation has led some researchers to suggest that the Nix-Gao model breaks down when the contact size is very small [26].

Huang et al. [4] mentioned one possible reason for the deviation is that the GNDs are not evenly distributed in the hemisphere area under the contact area. By introducing a maximum allowable GND density, they developed a new relationship between hardness and depth which agrees well with the nanoindentation results of Iridium [4].

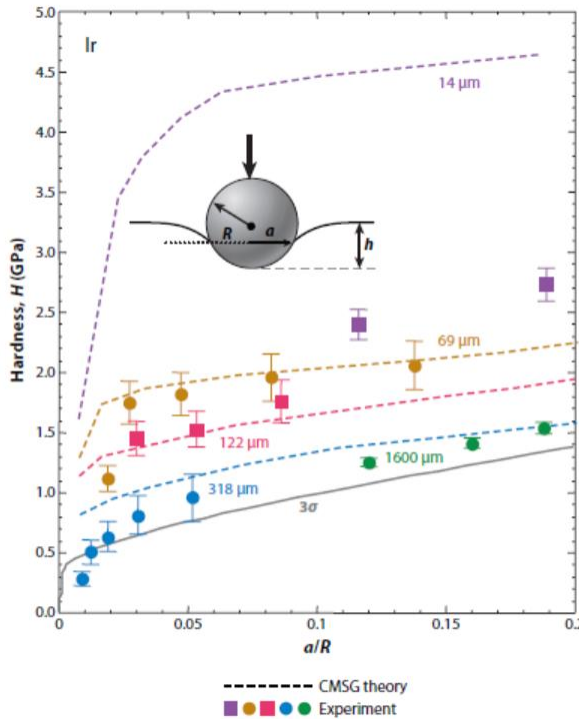


Fig. 2.13 Prediction of size effect of spherical indenter with CMSG theory [27].

2.3 Crystal Plasticity Finite Element Modelling

2.3.1 Overview

Crystal plasticity models have been intensively used to understand and predict the microstructure evolution and stress-strain response of crystalline metals at micro and mesoscale.

In crystal plasticity theory, the dislocations are regarded as the fundamental carriers of plasticity. The motion of dislocations along slip systems, concerning the plastic slip rates and the slip system geometry, dominate the plastic deformation of metals. Due to the orientation dependence of activated slip systems and anisotropy of elastic tensor, the elastic-plastic deformation of crystalline metals depends on the loading direction, which leads to the orientation dependence of mechanical properties such as strength, strain-hardening and crystallographic texture. Therefore, to predict the mechanical behavior of crystalline metals, a comprehensive theory should include both the

deformation mechanisms and the orientations relation to the applied boundary conditions (loading directions, rolling plane) [28].

Various methods [29, 30] have been developed to predict the plasticity behavior of materials over the last several decades. However, these methods were built under simple boundary conditions and failed to capture the mechanical interactions among the crystals in a polycrystal. For that reason, crystal plasticity finite element modeling (CPFEM) has drawn great interests as its ability to cope with complex boundary conditions. The total sample is separated into elements, the solution of the constitutive equation which connect the force and displacement are given in such elements.

In addition to the advantage of solving complicated boundary conditions, CPFEM also provides possibilities to incorporate various constitutive formulations, including phenomenological models and physics-based models of plasticity. This gives access to introduce size effect models into CPFEM by using phenomenological strain gradient theories [1, 2].

For phenomenological models, a critical resolved shear stress τ_c^α , is used as state variable for each slip system α . The total deformation gradient is decomposed into elastic and plastic parts, and the constitutive behavior can be fully described from the loading history. These models are classified as local models and have shown great power for mechanical strength and texture evolution of polycrystals. However, local models are insufficient to describe the size effects, which can occur in nanoindentation or micropillar compression.

As mentioned in 2.2.2, the size effects can be explained by strain gradient theory. The strain gradient leads to an extra increment of dislocation densities (GNDs) which increase the slip resistance. In phenomenological strain gradient models, the GNDs are integrated into the constitutive models. The calculation of strain gradients renders a constitutive model non-local, which means the calculations need to converge for a set of neighboring material points in the same time increment.

CPFEM simulations can be used in a great variety of fields, at both microscopic and macroscopic scales. Typical applications include surface roughening, texture evolution,

grain boundary mechanics, creep, martensitic transformation, damage initiation, micromechanical experiments simulation, etc. In summary, CPFEM has been proved to be an effective modeling platform that can deal with mechanical problems at different scales with complex boundary conditions.

2.3.2 Local model

2.3.2.1 Dislocation slip controlled plasticity

During plastic deformation, the crystal structure does not change, complete blocks of a crystal are translated parallel to crystallographic planes by integer multiples of the atomic spacing in those planes. Plastic deformation is mainly caused by dislocation slip, mechanical twinning and martensite transformation, and dislocation slip is the most important and dominant deformation mechanism in ductile materials.

In the slip system, it is the resolved shear stress that causes dislocation motion. This resolved shear stress τ is defined by [31]:

$$\tau = \sigma \cos\kappa \cos\lambda = m\sigma \quad \text{Eq. 2.21}$$

where κ is the angle between tensile direction and slip plane normal and λ the angle between tensile direction and slip direction (as shown in Fig. 2.14). The factor $m = \cos\kappa \cos\lambda$ is called Schmid-factor.

With Schmid's law the active slip systems of a single crystal can be determined. The slip system with the highest Schmid-factor will reach the critical resolved shear stress first and carry the plastic deformation. For fcc crystal there are 12 slip systems with the slip system $\{111\} <110>$, whereas in bcc crystal, 48 slip systems exist without unique defined slip plane, but with a defined slip direction $\{hkl\} <111>$, $\{hkl\}$ could be $\{110\}$, $\{112\}$ and $\{123\}$.

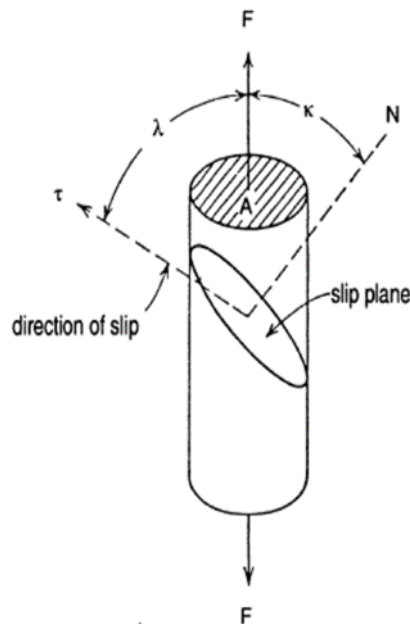


Fig. 2.14 Determining of Schmid factor [31].

2.3.2.2 Flow kinematics

The kinematics is the study of the displacement and motions of the material body without consideration of the forces that cause them.

To begin with, reference (or undeformed) configuration and current (or deformed) configuration are defined as B_0 and B respectively. As shown in Fig. 2.15. The locations of points (infinite material points) of the reference configuration and current configuration are expressed as position vector x and y respectively. The relationship between x and y can be expressed by the displacement vector $u = y - x$.

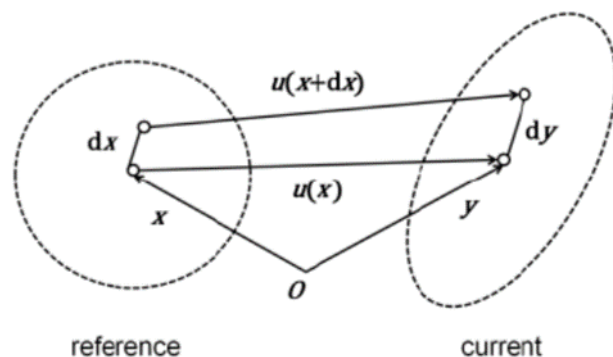


Fig. 2.15 Schematic representation of reference and current configuration [32].

Similarly, the infinitesimal positions of neighboring material points in the reference and current configuration are dx and dy , while dy is mapped from dx with $dy = du + dx$. The second rank tensor, F , which is named as the deformation gradient, can be expressed as,

$$dy = \left(\frac{\partial y}{\partial x} \right) dx = \left(I + \frac{\partial u}{\partial x} \right) dx = F dx \quad \text{Eq. 2.22}$$

where I is the second-rank identity tensor.

After definition of displacement vector v , the motion of a body or time-dependent displacement v can be given by the time derivative of the corresponding displacement field as,

$$v = \frac{d}{dt} u = \dot{u} = \dot{y} \quad \text{Eq. 2.23}$$

The total deformation gradient could be decomposed into elastic and plastic deformation gradient as,

$$F = F_e F_p \quad \text{Eq. 2.24}$$

Where F_e is the elastic deformation component, which is the reversible response of the lattice to external loads and displacements, and F_p is the plastic deformation component, which is irreversible permanent deformation part (as shown in Fig. 2.16).

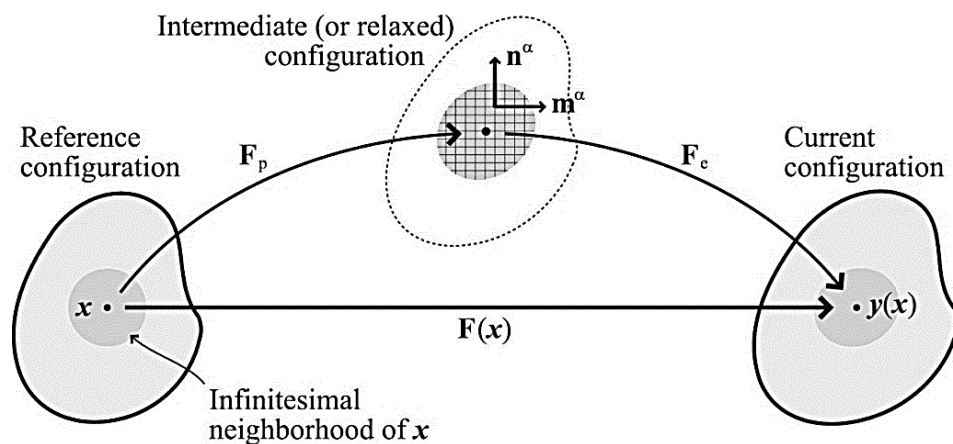


Fig. 2.16 Decomposition of the total deformation gradient [32].

Therefore, according to the deformation gradient, the spatial gradient of the total velocity, i.e. the velocity gradient L is:

$$\mathbf{L} = \dot{\mathbf{F}}\mathbf{F}^{-1} = \frac{\partial \mathbf{v}}{\partial \mathbf{y}} \quad \text{Eq. 2.25}$$

As total deformation gradient could be decomposed into elastic and plastic part, Eq.2.15 can be transformed into,

$$\mathbf{L} = \dot{\mathbf{F}}\mathbf{F}^{-1} = \dot{\mathbf{F}}_e\mathbf{F}_e^{-1} + \dot{\mathbf{F}}_e(\dot{\mathbf{F}}_p\mathbf{F}_p^{-1})\mathbf{F}_e^{-1} = \mathbf{L}_e + \dot{\mathbf{F}}_e\mathbf{L}_p\mathbf{F}_e^{-1} \quad \text{Eq. 2.26}$$

Where \mathbf{L}_e is the elastic velocity gradient, and \mathbf{L}_p is the plastic velocity gradient.

2.3.2.3 Phenomenological constitutive laws

After definition of deformation gradient \mathbf{F} and velocity gradient \mathbf{L} , the plastic deformation evolves as,

$$\dot{\mathbf{F}}_p = \mathbf{L}_p\mathbf{F}_p \quad \text{Eq. 2.27}$$

If only the deformation process is involved for dislocation slip, L_p can be defined as,

$$\mathbf{L}_p = \sum_{\alpha=1}^N \dot{\gamma}_\alpha \mathbf{m}^\alpha \mathbf{n}^\alpha \quad \text{Eq. 2.28}$$

Where \mathbf{m}^α and \mathbf{n}^α are the unit vector describing the slip direction and normal direction to the slip plane of the slip system α respectively. N is the number of the active slip system and $\dot{\gamma}_\alpha$ is the shear rate for the active slip system.

The shear rate is determined by the resolved shear stress τ_α and the critical resolved shear stress τ_α^c . For fcc single crystal, this kinetic law on the slip system is given as,

$$\dot{\gamma}_\alpha = \dot{\gamma}_0 \left| \frac{\tau_\alpha}{\tau_\alpha^c} \right|^m \operatorname{sgn}(\tau_\alpha) \quad \text{Eq. 2.29}$$

$\dot{\gamma}_\alpha$ is the shear rate for the active slip system α . $\dot{\gamma}_0$ and m are the reference shear rate and rate sensitivity of slip system respectively.

The micromechanical interaction between different slip systems should also be taken into consideration by,

$$\dot{\tau}_\alpha^c = \sum_{\beta=1}^N h_{\alpha\beta} |\dot{\gamma}_\beta| \quad \text{Eq. 2.30}$$

Where $h_{\alpha\beta}$ is the hardening matrix and given by,

$$h_{\alpha\beta} = q_{\alpha\beta} \left[h_0 \left(1 - \frac{\tau_\beta^c}{\tau_s^c} \right)^a \right] \quad \text{Eq. 2.31}$$

In this equation, h_0 , a , and τ_s^c are slip hardening parameters. The value $q_{\alpha\beta}$ incorporates the effect of self-hardening ($\alpha = \beta$) and latent hardening ($\alpha \neq \beta$) and is assigned as 1.0 for coplanar slip and 1.4 otherwise.

2.3.3 Non-local model

Non-local models are used to treat problems at smaller scale and describe mechanical size effects. Various non-local models have been developed which are based on different internal variables such as dislocation densities and plasticity strain gradients. In this work, the nonlocal model is based on a visco-plastic strain gradient developed by Wulffinghoff and Böhlke [33]. An equivalent plastic strain $\dot{\gamma}_{eq}$ is introduced by the expression:

$$\dot{\gamma}_{eq} = \sum_{\alpha} \dot{\gamma}_{\alpha} \quad \text{Eq. 2.32}$$

With the idea of Peerlings and Engelen [34, 35], a non-local equivalent plastic strain rate $\dot{\gamma}$ is introduced as:

$$\dot{\gamma}(\mathbf{x}) = \frac{1}{\Psi(\mathbf{x})} \int_{\Omega} \psi(\mathbf{y}; \mathbf{x}) \dot{\gamma}_{eq}(\mathbf{y}) dV(\mathbf{y}) \quad \text{Eq. 2.33}$$

where Ω is the domain occupied by the body, and Green's weight function is defined as:

$$\psi(\mathbf{y}; \mathbf{x}) = \frac{1}{4\pi|\mathbf{x}-\mathbf{y}|\ell^2} \exp\left(-\frac{|\mathbf{x}-\mathbf{y}|}{\ell}\right) \quad \text{Eq. 2.34}$$

$$\Psi(\mathbf{x}) = \int_{\Omega} \psi(\mathbf{y}; \mathbf{x}) dV(\mathbf{y}) \quad \text{Eq. 2.35}$$

where ℓ is a material parameter that has dimensions of length. The length parameter determines the size of the volume, which effectively contributes to the nonlocal quantity and which is related to the scale of the microstructure.

Combining Eq.2.32 and Eq.2.33 leads to a Helmholtz-type partial differential equation in the form:

$$\dot{\gamma} - \dot{\gamma}_{eq} = \ell^2 \nabla^2 \dot{\gamma} \quad \text{Eq. 2.36}$$

The evolution of the critical shear stress on each slip system α is defined from an equation of the form

$$\dot{\tau}_{\alpha}^c = \sum_{\beta} h_{\alpha\beta} |\dot{\gamma}_{\beta}| - \ell^2 Z \nabla^2 \dot{\gamma} \quad \text{Eq. 2.37}$$

where Z is a material parameter that has dimensions of stress. With Eq.2.36, it can be written as:

$$\dot{\tau}_\alpha^c = \sum_\beta h_{\alpha\beta} |\dot{\gamma}_\beta| + Z(\dot{\gamma}_{eq} - \dot{\gamma}) \quad \text{Eq. 2.38}$$

Where the first part refers to local critical resolved shear stress $\dot{\tau}_\alpha^{\text{local}}$ and the latter part refers to non-local critical resolved shear stress $\dot{\tau}_\alpha^{\text{non-local}}$. The material length parameter ℓ and material stress parameter Z are referred as non-local parameters. The definition of boundary conditions plays an important role in the behavior of the solution. When $\frac{\partial \dot{\gamma}}{\partial n} = 0$, where n is the outward unit normal vector on $\partial\Omega$, then:

$$\int_\Omega \dot{\tau}_\alpha^{\text{non-local}} dV = Z \int_\Omega (\dot{\gamma} - \dot{\gamma}_{eq}) dV = -\ell^2 Z \int_\Omega \nabla^2 \dot{\gamma} dV = -\ell^2 Z \int_{\partial\Omega} \frac{\partial \dot{\gamma}}{\partial n} dA = 0 \quad \text{Eq.2.39}$$

the average values of $\dot{\gamma}$ and $\dot{\gamma}_{eq}$ on Ω are equal and the average contribution on Ω of the non-local hardening vanishes, the result of non-local models will be the same as local models. When $\dot{\gamma} = 0$, the non-local parameters are implemented into the model.

2.3.4 Crystal plasticity models in nanoindentation

Nanoindentation is a powerful tool to characterize and measure mechanical properties of materials on micro- and nanometer length scales. Simulation of nanoindentation has become an important application field of CPFEM.

Non-local crystal plasticity models can be used to capture the size effects in nanoindentation. Engels et al. [36] used a non-local crystal plasticity model proposed by Ma et al. [37] to quantify ISE of spherical indenters and determine the non-local crystal plasticity parameters. The flow rule and the hardening law can be expressed as:

$$\dot{\gamma}_\alpha = \dot{\gamma}_0 \left| \frac{\tau_\alpha + \tau_\alpha^{\text{GNDk}}}{\tau_\alpha^{\text{c}} + \tau_\alpha^{\text{GNDi}}} \right|^{p1} sgn(\tau_\alpha + \tau_\alpha^{\text{GNDk}}) \quad \text{Eq.2.40}$$

$$\widehat{\dot{\tau}_\alpha} = \sum_{\beta=1}^N h_0 q_{\alpha\beta} \left(1 - \frac{\widehat{\tau}_\alpha}{\widehat{\tau}_{sat}}\right)^{p2} |\dot{\gamma}_\beta| \quad \text{Eq.2.41}$$

Where $\tau_\alpha^{\text{GNDk}}$ and $\tau_\alpha^{\text{GNDi}}$ are kinematic hardening part and isotropic hardening part of back stress generated by GNDs, $p1$ is the inverse value of the strain rate sensitivity, $\widehat{\tau}_{sat}$ is the saturation slip resistance, and $p2$ is a fitting parameter.

During indentation test, the material may either sink-in or pile-up around the indenter, which change the actual contact area between the indenter and the specimen. These differences lead to the error of hardness and modulus measurement. Therefore, a better understanding of the deformation zone is of great interest. Wang *et al.* [38] indicated a coupled effect of crystallographic orientation of indented material and indenter geometry on surface pile-up behavior through the CPFEM simulation results. The shape of contact area around the Berkovich indenter at various indented crystallographic orientation leads to different activated slip systems and pile-up patterns.

In addition, CPFEM are applied in many other nanoindentation problems such as the detection of the dislocation patterns below indents area [39], orientation dependent deformation by slip and twinning in magnesium [40], crystallographic texture evolution under indents [41], exploration of strain localization and damage in steels [42] etc.

3 Material

3.1 Chemical composition

In this thesis, a ferrite-stainless steel AISI 439 is investigated. AISI 439 is a cold-rolled, titanium stabilized low carbon alloyed steel. With the excellent resistance to stress corrosion cracking, good weldability, high thermal conductivity and low thermal expansion characteristics, this steel has been applied in sinks, heat exchanger tubes, exhaust systems, where the material must resist corrosion in a variety of oxidizing environments.

The normal chemical composition is shown in Tab. 3.1. The carbon content is relatively low as carbon is a strong austenite former and can reduce both toughness and corrosion resistance strongly. Chromium is the most important alloying in ferritic stainless steel, as it can significantly improve the corrosion resistance of steel. In addition, Chromium also increases the resistance of oxidation at high temperature.

Titanium can improve corrosion resistance and toughness of the steel by bonding with carbon or nitrogen in the form of highly stable compounds. The formed titanium-nitride particles are randomly distributed in the ferrite matrix and act as a stabilizer to maintain the structure through a large range of temperatures.

The small amount of Nickel is used to improve the low temperature toughness and reduce the corrosion rate. Manganese can stabilize ferrite at high temperature and improve the hot ductility. Silicon is added as a ferrite stabilizer as well.

Tab. 3.1 The chemical composition of AISI 439 (mass content in %).

C	Cr	Ti	Ni	Mn	Si	S	P
≤0.05	16.0- 18.0	0.15- 0.80	≤0.30	≤1.00	≤1.00	≤0.015	≤0.04

3.2 Microstructure

AISI 439 is a single-phase ferritic steel with bcc crystal structure at all temperatures below the melting point. Fig. 3.1 gives the microstructure of the material from EBSD measurement.

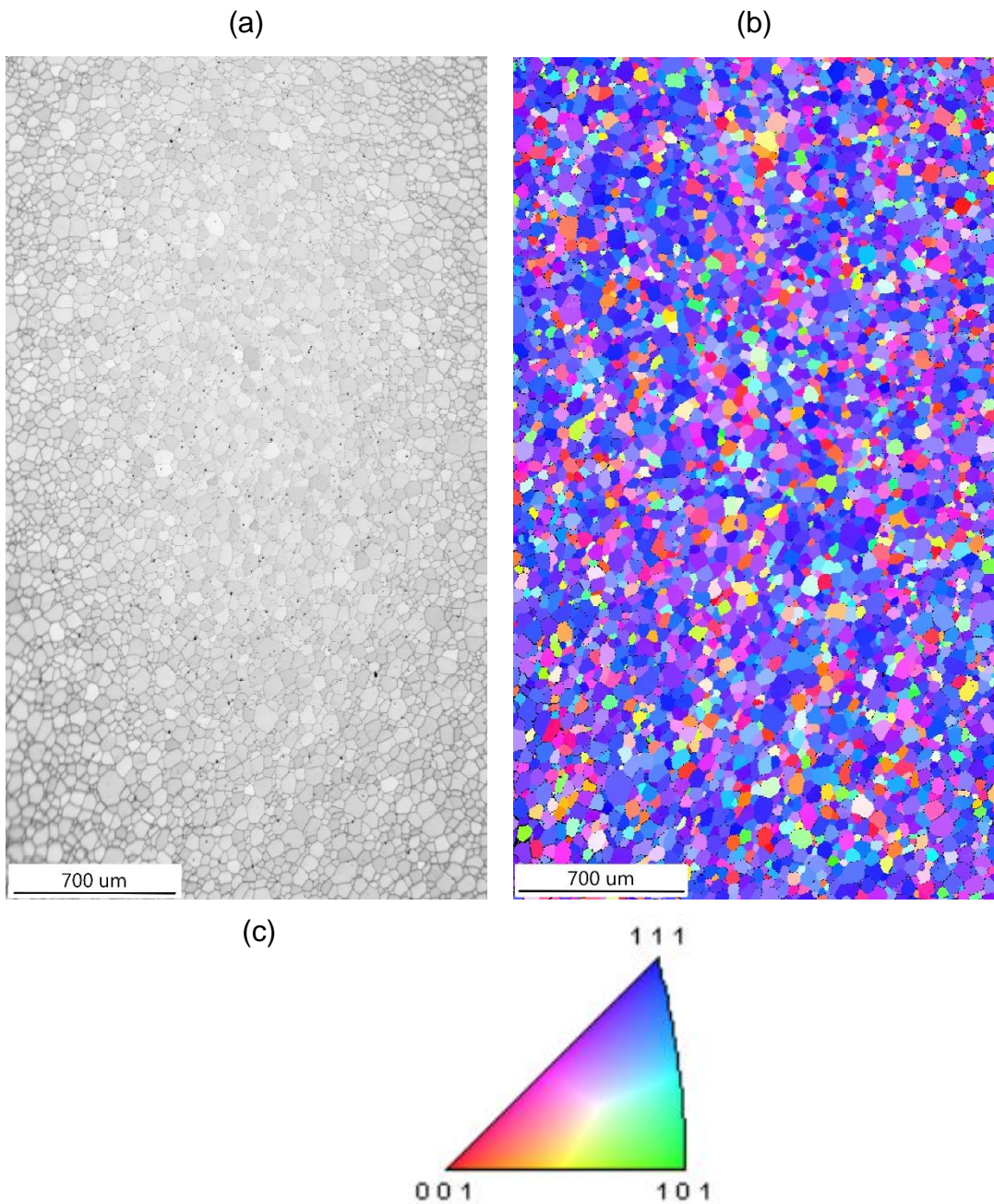


Fig. 3.1 Scanning maps of AISI 439 from EBSD measurements: (a) Image quality (IQ) map; (b) Orientation map coloring by inverse pole figure of normal direction (ND).

Fig. 3.2 shows the average grain diameter of ferrite phase in number fraction and area fraction, which are 42 μm and 54 μm respectively. By analysis of the EBSD scattering point data, the Orientation Distribution Function (ODF) and the pole figures of the material in rolling direction (RD) – transverse direction (TD) plane are plotted as shown

in Fig. 3.3. It can be observed that AISI 439 possess the typical bcc texture, which is the α -fiber $<110>$ // RD and γ -fiber $\{111\}$ // ND [43]. The most common texture, γ -fiber, can be found in both ODF figure and $\{111\}$ pole figure. It corresponds to the pole at the center of $\{111\}$ pole figure.

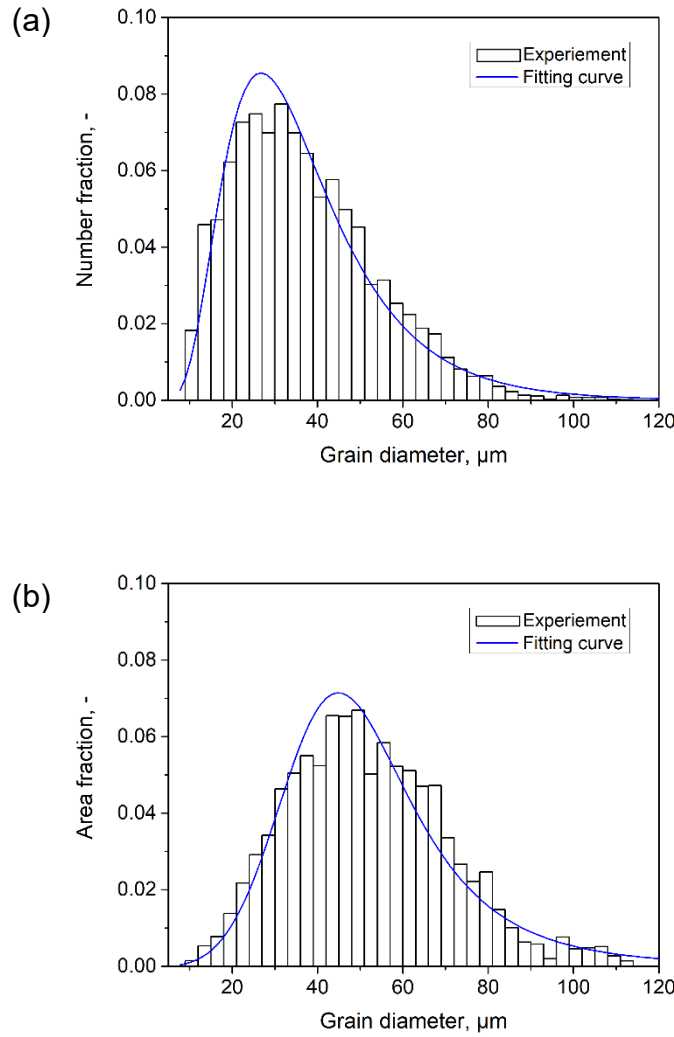


Fig. 3.2 Grain size distribution of AISI 439: (a) number fraction; (b) area fraction.

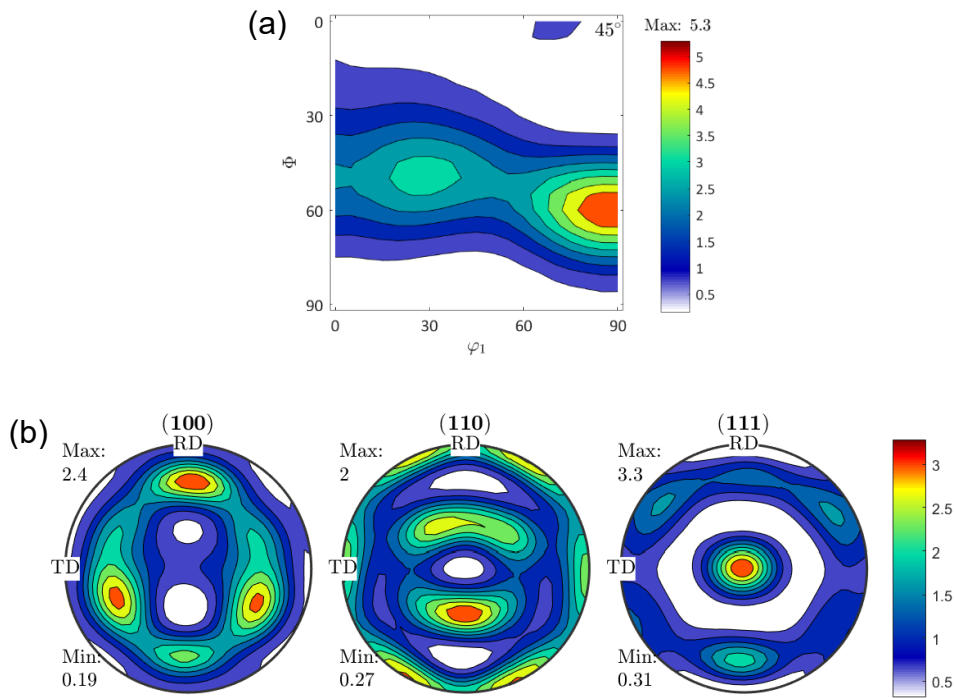


Fig. 3.3 Grain orientation distribution in RD-TD plane: (a) ODF figures with $\varphi_2=45^\circ$; (b) the $\{100\}$, $\{110\}$ and $\{111\}$ pole figures.

3.3 Mechanical properties

The main characteristic of AISI 439 is its anisotropic plastic flow behavior. Fig. 3.4 shows the flow curves of AISI 439 from different loading angles at room temperature (RT) and quasi-static (QS) loading conditions from the uniaxial tensile test.

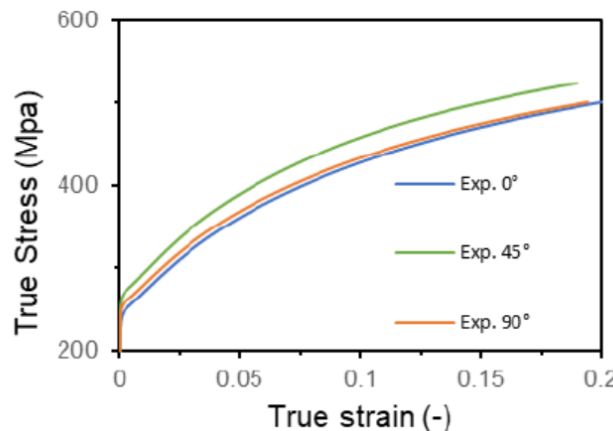


Fig. 3.4 Flow curves of AISI 439 with different loading angles of experiments at RT and QS.

4 Nanoindentation test

4.1 Sample preparation and test setup

To prepare the sample, a steel sheet of AISI 439 is cut into a small piece with a dimension of 25mm (RD) x 10mm (TD) x 1mm (ND). It is firstly grinded, mechanical polished and electropolished for EBSD measurement. The EBSD measurement is used for microstructure characterization and grain selection during the nanoindentation test. After EBSD measurement, the sample is etched with Nital solution for better observation of grain boundaries under the light microscope, which is essential for navigation of interested positions in nanoindentation tests.

All of the nanomechanical tests are conducted in the Bruker's Hysitron TI980 TribolIndenter. The force and displacement control during experiments are realized by the component named transduce. There are two kinds of transducers, low load and high load, which gives the possibility of indentation tests at both nano- and micro scale. The maximum load for low load transducer can reach to 10 mN. For high load, the maximum load is up to 10 N. Either of the transducer possesses a minimum displacement noise floor of 0.2 nm.

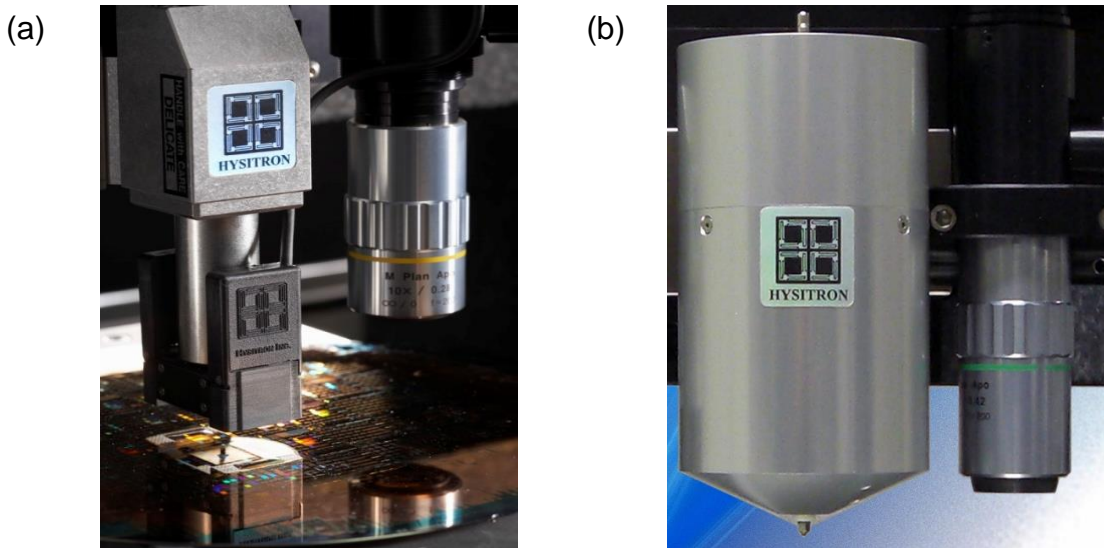


Fig. 4.1 Dual heads of the TribolIndenter: (a) Low load transducer; (b) High load transducer [19].

The first step for the test is properly mounting of tips and testing samples, making sure the tips are connected tightly and the samples are well-fixed on the stage. The sample is mounted on the stage (as shown in Fig. 4.2) by magnetic force provided by the stage at several positions.

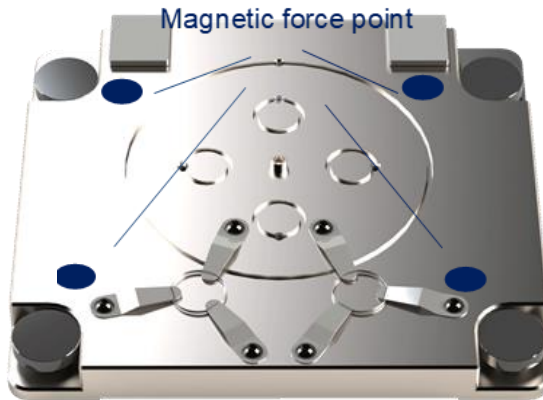


Fig. 4.2 Sample stage of nanoindentation machine [19].

After sample mounting, the calibrations of the system are necessary. Calibrations are important to maintain a safe operating environment and obtain accurate testing results.

- 1) Transducer calibration: The Transducer calibration is performed with the nanoindentation probe installed in the transducer and the transducer installed in the instrument. It is performed in the air, far from any sample. An indent is performed in the air to check and compare the transducer values with default values.
- 2) Optical-Tip probe offset calibration: Each time after mounting of new transducer or new tip, there will be a tiny change of the spatial distance between the focus of optical lens and the end of tip, which is caused by the geometry of different tips, the incline of tip during mounting and other reasons. So optical-tip offset calibration is necessary for accurate positioning and protection of the system. Usually the calibration is realized by automatically performing of seven indents in the shape of

- an “H”. The relative distance between optical and tip is confirmed by superposition the center of focus on the center of the “H” pattern.
- 3) Tip calibration: Performing a tip calibration for each tip will compensate for non-perfect tip shape. The tip radius of curvature and normal dulling of the tip can both be corrected by recalibrating the tip. To begin the calibration of the probe, install the tip and fused quartz sample provided with the instrument. Several indents are performed in the standard sample. After analysis of indentation tests, fitting the contact depth- contact area curve and calculate the new area function of tip.
 - 4) Machine compliance calibration: As the displacement during nanoindentation tests is at nanometer scale, the compliance of the machine itself cannot be neglected. The machine compliance calibration can calculate the compliance of the machine during indentation tests and correct the recorded displacement value. The calibration is more important for high load test, where the high machine compliance can lead to a significant deviation of displacement from the real value.

4.2 Loading function

Loading function should also be set in advance. There are mainly two types of loading modes, which are load-controlled and displacement-controlled respectively. In load-controlled mode, the indenter will apply a certain force on the sample, while in displacement-controlled mode, the indenter will penetrate the sample by a pre-defined displacement.

In this work, the loading functions are all displacement controlled, quasi-static with constant strain rate tests. Quasi-static nanoindentation tests are typically applied on bulk materials, where a standard load function with loading, holding, unloading segments in quasi-static state are conducted.

In nanoindentation tests, the constant strain rate tests are fulfilled based on the equation:

$$\dot{\varepsilon} = \frac{\dot{h}}{h} = \text{constant} \quad \text{Eq. 4.1}$$

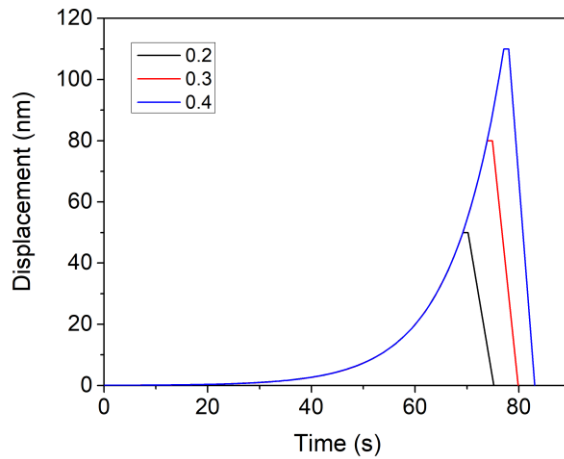
Where \dot{h} is the penetration rate, h is the penetration depth. All the tests are conducted with constant strain rate of 0.1 s^{-1} .

To achieve the indentation strain rate of 0.2, 0.3 and 0.4, the peak displacements of different tests are set as shown in Tab. 4.1. The holding time is 1 s and the unloading time is 5 s. Fig. 4.3 gives all the loading functions which show the relationship between time and displacement.

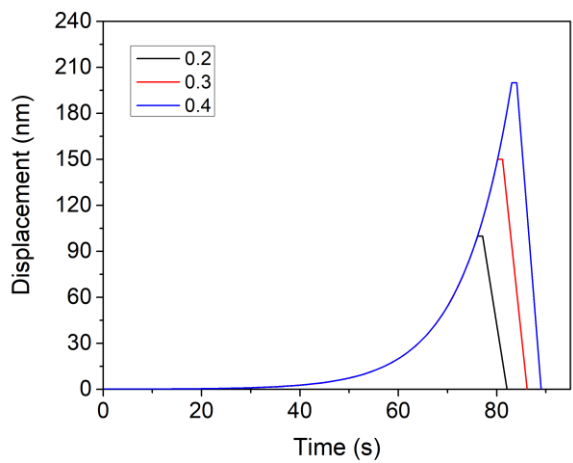
Tab. 4.1 Peak displacements of experiments with different tip radius.

Peak Displacement (nm)	Indentation strain		
	0.2	0.3	0.4
Tip radius (μm)	1	50	80
	2	100	150
	5	200	350
	20	300	500

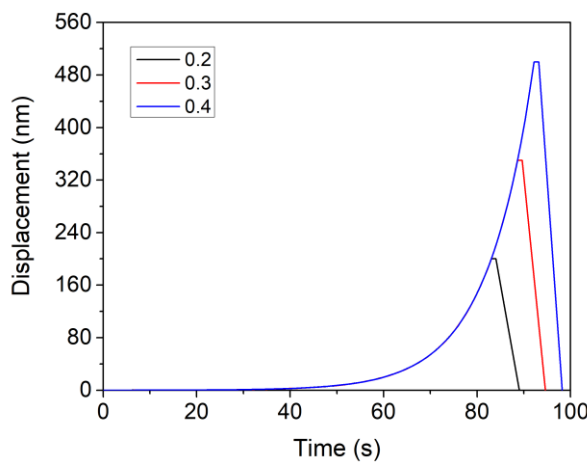
(a)



(b)



(c)



(d)

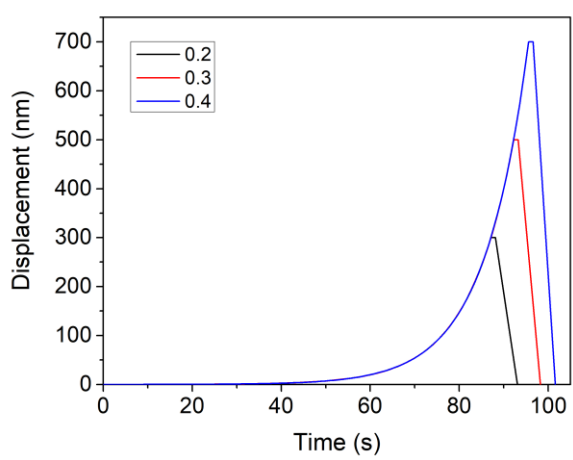


Fig. 4.3 Loading function of experiments at constant strain rate of 0.1 s^{-1} with: (a) tip radius $1 \mu\text{m}$; (b) tip radius $2 \mu\text{m}$; (c) tip radius $5 \mu\text{m}$; (d) tip radius $20 \mu\text{m}$.

4.3 Experiment program

For spherical tips, the size effects are more pronounced with various tip radius. In order to investigate the size effects of nanoindentations, four conical-spherical tips with different tip radius, 1 μm , 2 μm , 5 μm and 20 μm are used. The 1 μm and 2 μm tips own a cone angle of 90 degree, while 5 μm and 20 μm tips have a cone angle of 60 degree. The 1 μm and 2 μm tips are mounted into low load transducer and the 5 μm and 20 μm tips are mounted into the high load transducer. The mechanical strength of steel depends on the crystallographic orientation of grains. In addition, the grain boundary strengthening can also lead to higher load under deformation. To avoid the influence of grain boundary and orientation on the hardness of material, all the tests are performed within one single crystal with relatively large grain diameter. For each tip, three sets of indentations tests are performed with indentation strain a/R equal to 0.2, 0.3 and 0.4. As spherical indents are not geometrical self-similarity, which means the strain within the material varies with different penetration depth. For comparison of hardness values with different spherical tips, the indentation strain should keep the same.

As all the indentations tests are supposed to located within one grain, the first criterion is the diameter of grains. The grain size should be as big as possible to avoid interaction between indents or grain boundary effects. For the purpose of validation of crystal plasticity parameters and exploration of the capability of CPFEM models in different crystallographic orientations, two grains with crystallographic orientations close to {100} and {111} orientations in the [001] unit triangle of the inverse pole figure were chosen, as shown in Fig. 2.1. The Euler angles and grain diameter of the grains are listed in Tab. 4.2Tab. 4.2. It should be mentioned that as there are only few grains with crystallographic orientations close to {110} orientation, it is difficult to find a proper grain with large enough area and clean sample surface, so only two grains are selected in the test.

Tab. 4.2 Euler angles and grain diameters of selected grains.

Grain ID	Euler angles			Grain diameter (μm)
	ϕ_1	φ	ϕ_2	
4833	154.734	111.641	331.94	96.95
4200	288.993	89.121	190.58	70.44

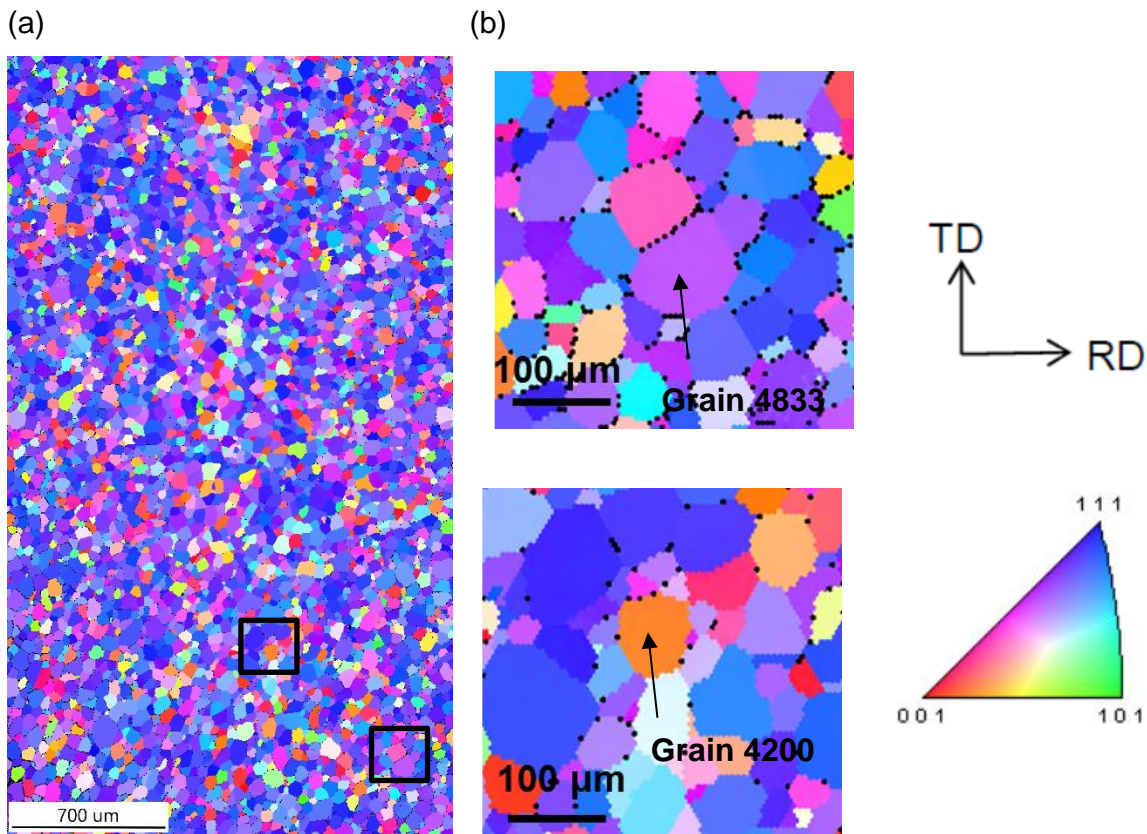


Fig. 4.4 Crystallographic orientations of selected grains for experiments: (a) Locations in the whole EBSD map (b) after zoom in.

Before experiments, the sample should be mounted on the stage and all the calibrations of the system, including transducer calibration, Optical-Tip probe offset calibration and tip calibration, should be performed. The in-situ SPM module of the machine is utilized in order to navigate the interested positions precisely. In addition,

post-test SPM imaging provides quantitative characterization of the pile-up patterns after deformation.

After confirmation of the position, the experiment can be performed with the pre-set loading functions. Each time when the tip is changed, the calibrations should be performed again. After all the experiments are finished, a cube corner tip is mounted to perform post-SPM imaging as cube corner tip is much sharper than conical-spherical tip, which can capture the topography of the residual indents and the pile-up around the indents. The whole experiment process is given in Fig. 4.5.

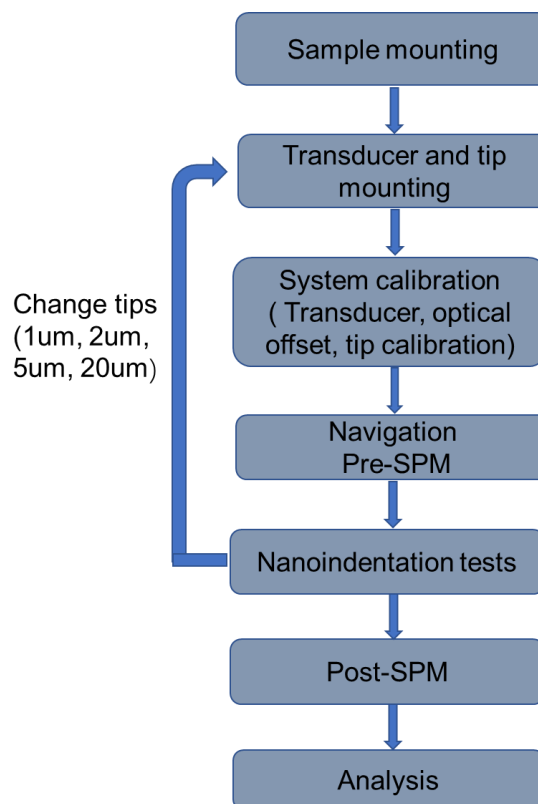


Fig. 4.5 Experiment flow diagram.

After test, the recorded displacement and load data should first be corrected by offsetting the starting point to the zero point of the coordinate. The contact depth h_c are calculated from the maximum depth h_{\max} and the final depth after unloading h_f , which

are directly recorded by the machine. The area function after tip calibration gives the relationship between h_c and contact area A , so the hardness value can be calculated.

5 Size effect in nanoindentation tests

5.1 Load-displacement curve

All the experiments are performed within two grains whose orientations are close to {111} and {100} in the [001] unit triangle of the inverse pole figure respectively. The pre in-situ SPM images of the two grains are shown in Fig. 5.1. The Nital solution etches the grain boundaries, which can be observed easily in the SPM images.

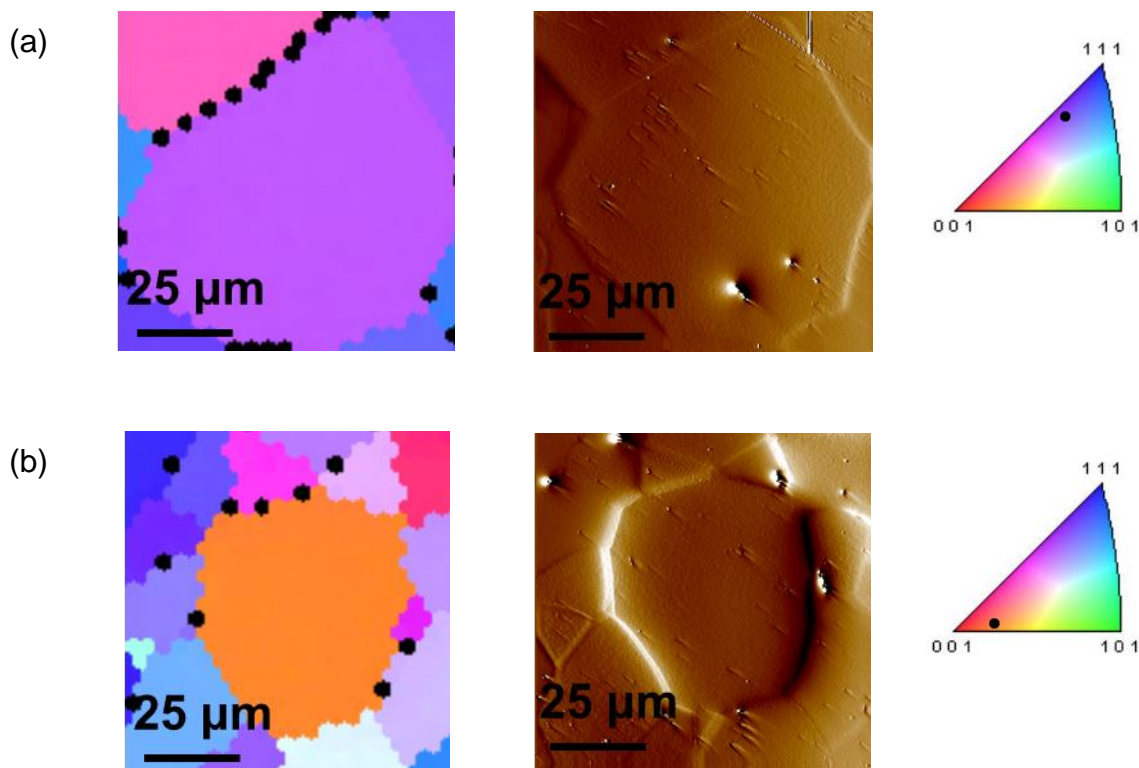


Fig. 5.1 EBSD IPF plots and corresponding in-situ SPM images of tested grains: (a) grain 4833; (b) grain 4200.

After indentation tests, a post in-situ SPM scanning is performed to validate the position of residual indents and capture the pile-up around indents as well. Fig. 5.2 to Fig. 5.6 display the force-displacement curves (P-H curves) of the indentation tests within grain 4833 and their corresponding positions in post SPM images.

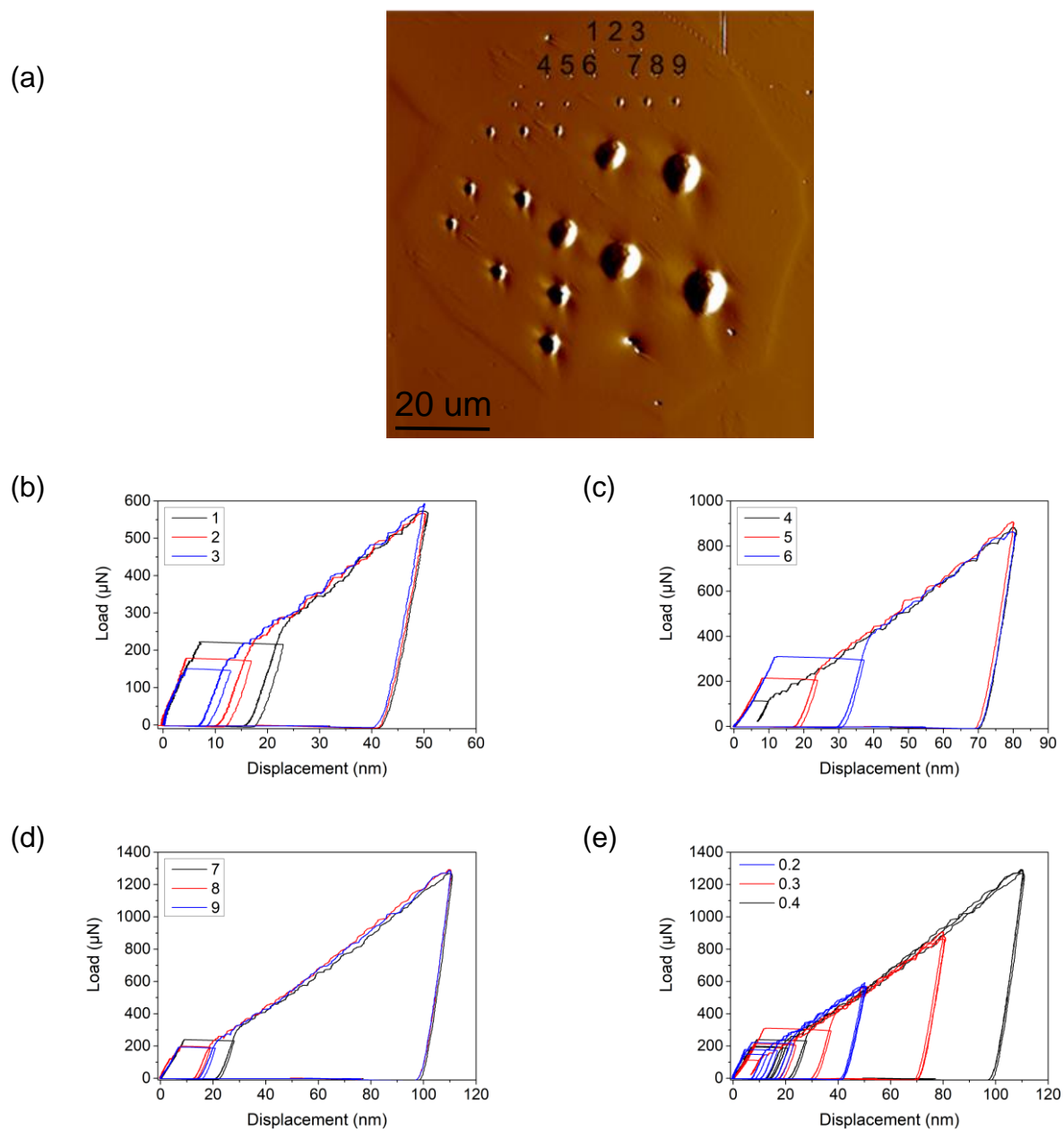


Fig. 5.2 Indentation tests in grain 4833 with 1 μm tip: (a) SPM image; (b) P-H curves with $a/R=0.2$; (c) P-H curves with $a/R=0.3$; (d) P-H curves with $a/R=0.4$; (e) Comparison of all P-H curves.

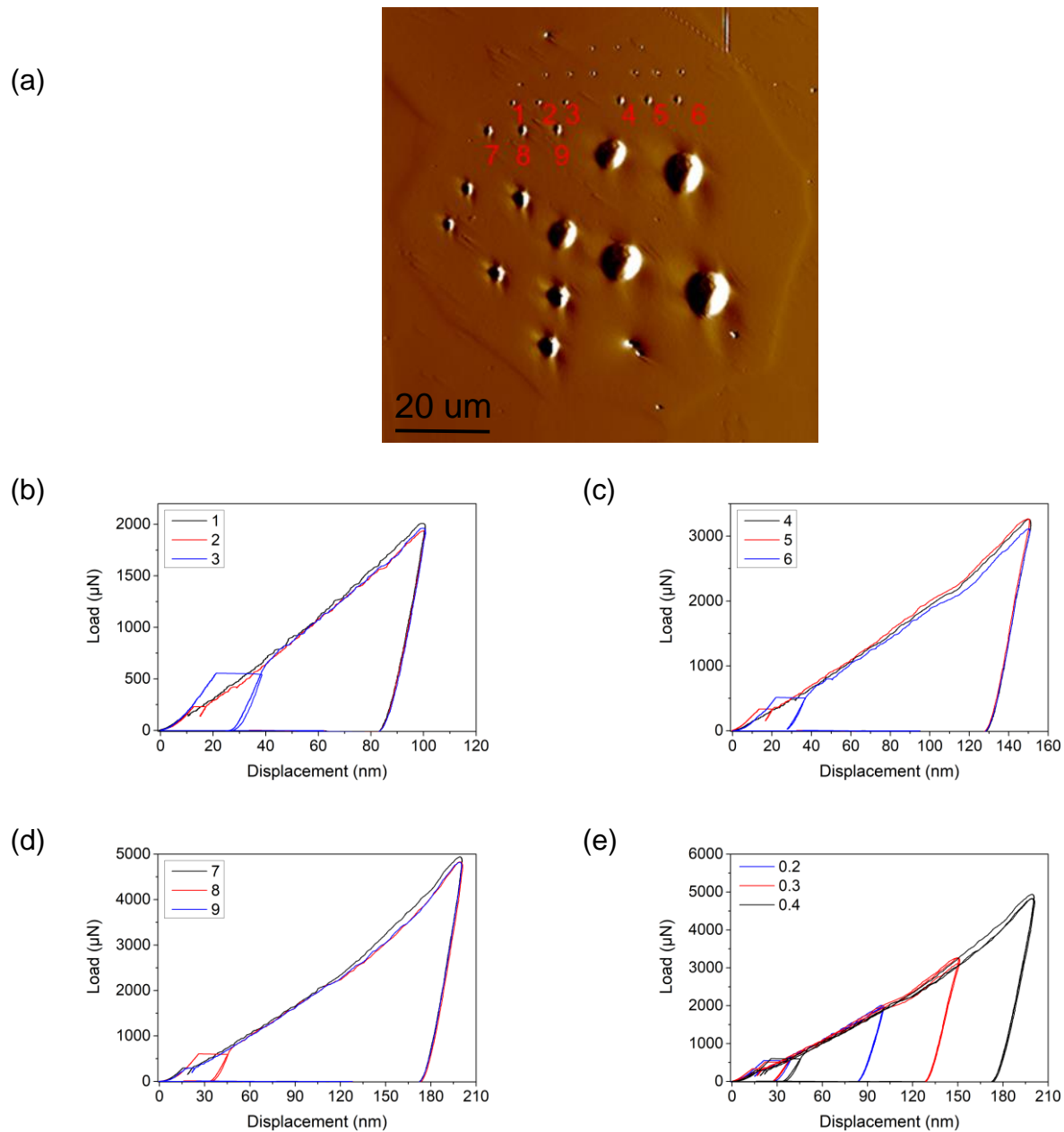


Fig. 5.3 Indentation tests in grain 4833 with 2 μm tip: (a) SPM image; (b) P-H curves with $a/R=0.2$; (c) P-H curves with $a/R=0.3$; (d) P-H curves with $a/R=0.4$; (e) Comparison of all P-H curves.

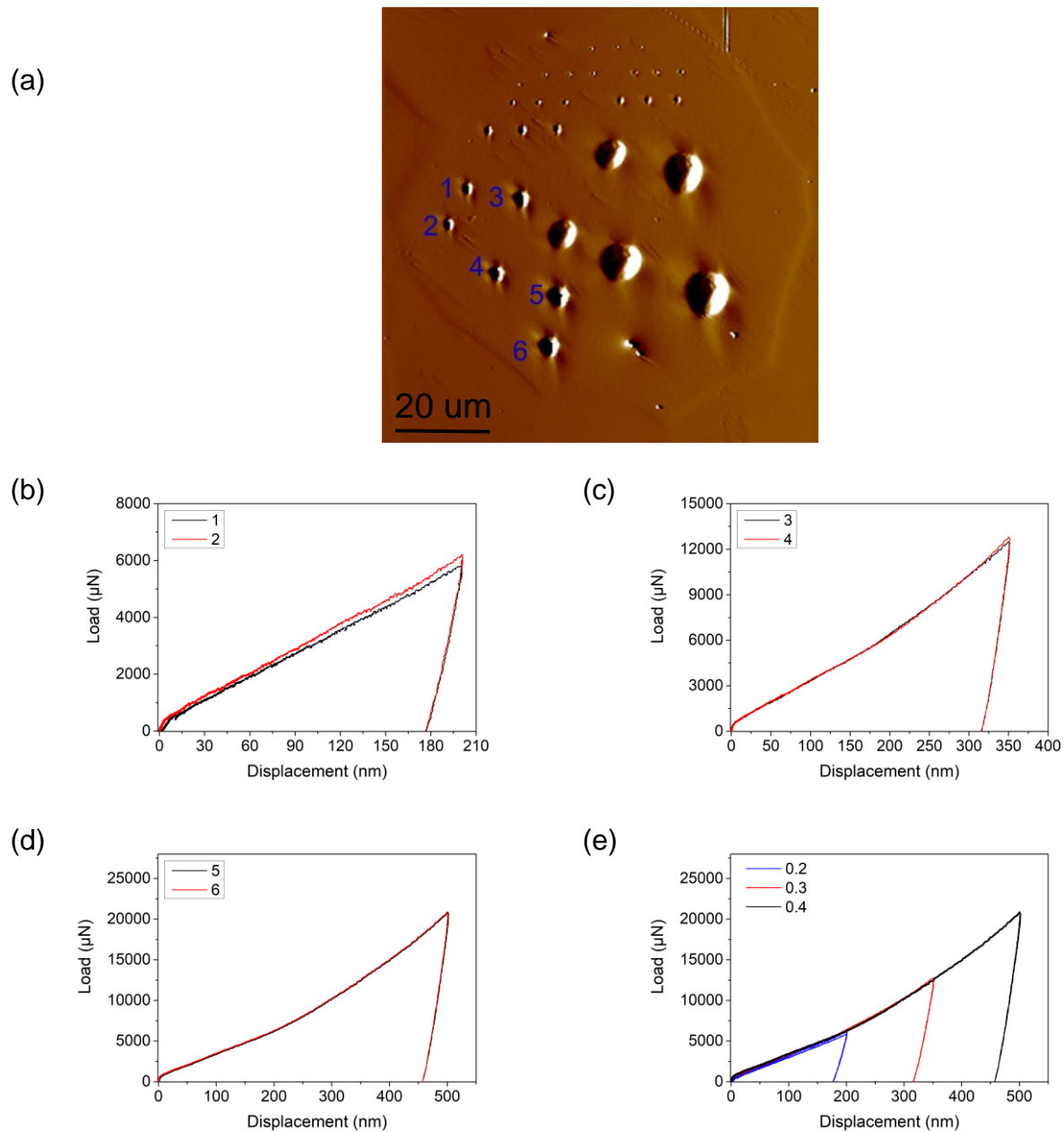


Fig. 5.4 Indentation tests in grain 4833 with 5 μm tip: (a) SPM image; (b) P-H curves with $a/R=0.2$; (c) P-H curves with $a/R=0.3$; (d) P-H curves with $a/R=0.4$; (e) Comparison of all P-H curves.

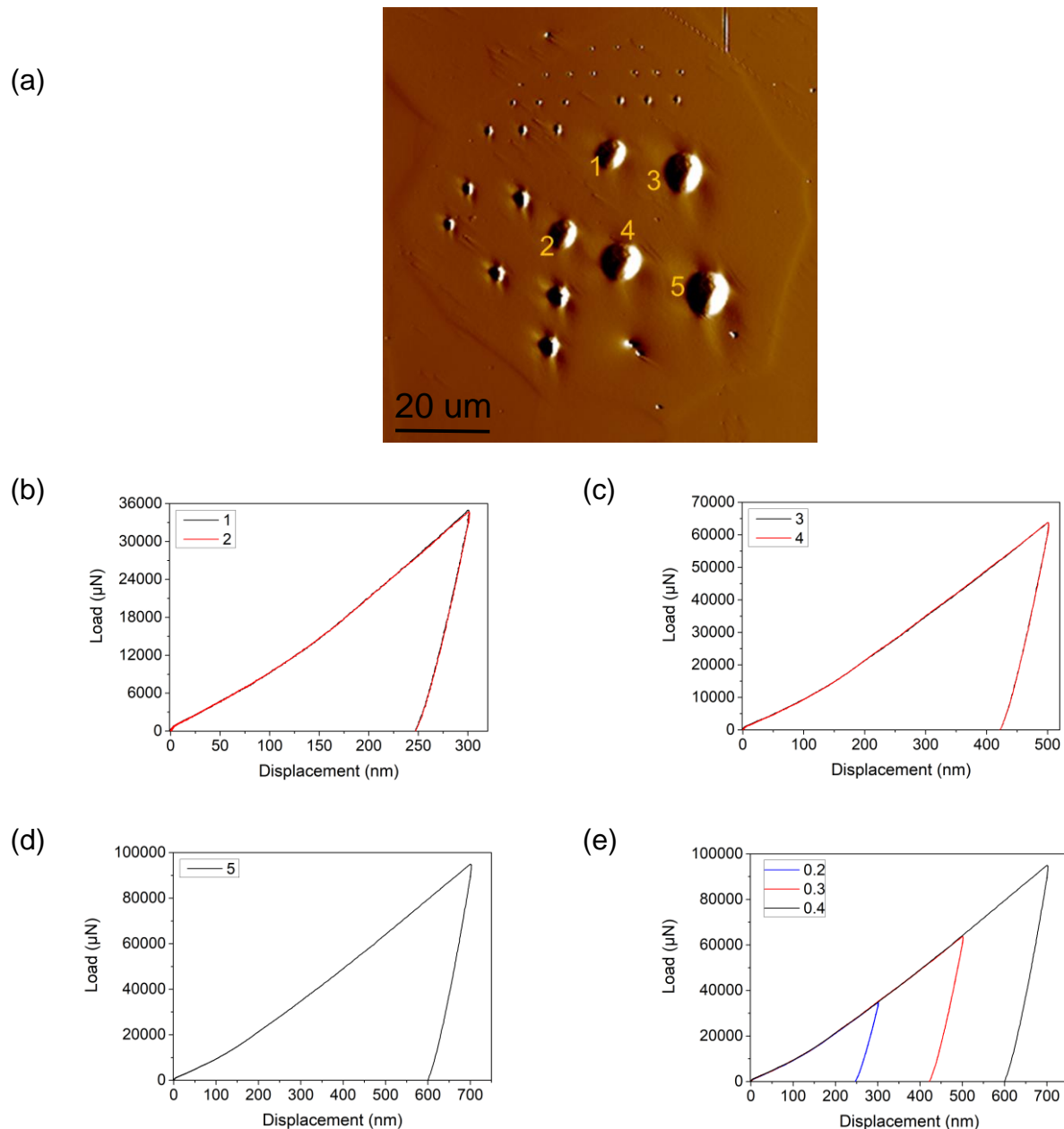


Fig. 5.5 Indentation tests in grain 4833 with 20 μm tip: (a) SPM image; (b) P-H curves with $a/R=0.2$; (c) P-H curves with $a/R=0.3$; (d) P-H curves with $a/R=0.4$; (e) Comparison of all P-H curves.

For 1 μm and 2 μm tips, three repeated indentation tests are performed at each indentation strain. As for 5 μm and 20 μm tips, two parallel tests are conducted due to the limitation of grain size. The spacing between indents should keep as big as possible to avoid the interaction among the plastic zones of indents. Only one test is performed

with the 20 μm tip at indentation strain of 0.4, as the residual imprints and the plastic zone of this test is relatively large.

It can be observed that all the tests are located within the grain. Generally, the P-H curves of the tests with the same loading function show good consistency. However, there are still some deviations among parallel tests, i.e. tests with 2 μm tip at indentation strain of 0.3 and 5 μm tip at indentation strain of 0.2. The deviations may originate from various reasons. Firstly, during sample preparation, there are some inclusions appeared on the sample surface during electro-polishing. Besides, AISI 439 possess small mass of carbides among ferrite phase, the indentation tests may locate right on the position of carbides, which leads to the difference. In addition, the 2D EBSD map and SPM image fail to offer the information along ND direction, as the grain shape can be arbitrary, the indenters can penetrate into other grains under the surface during indentation tests.

Fig. 5.6 to Fig. 5.9 give the P-H curves of the indentation tests within grain 4200 and their corresponding positions in post SPM images. The P-H curves show reproducibility on each tip, but the deviations still exit. It should be mentioned that for indentation tests with the 5 μm tip, due to the slight error in Optical-Tip probe offset calibration, the indents have some offset from the pre-set locations. The tests with tip radius 5 μm reach the grain boundaries, which slightly lower the P-H curves. The first test at indentation strain of 0.4 with 5 μm tip overlaps with the pre-performed 2 μm tip test at strain of 0.4, leads to the extremely high P-H curve. Due to the overlapping, the residual imprints of the 2 μm tip test are invisible in the SPM image.

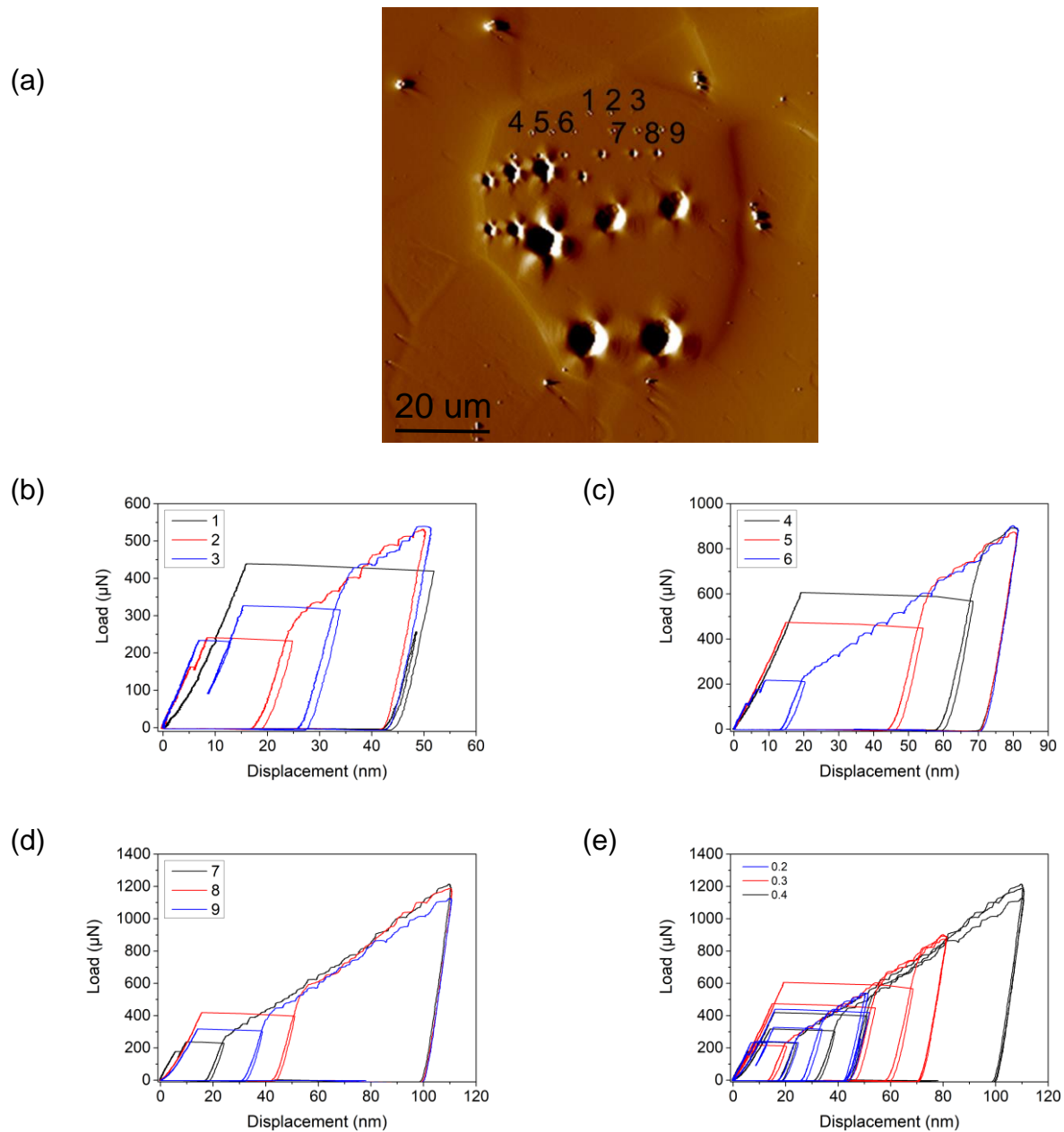


Fig. 5.6 Indentation tests in grain 4200 with 1 μm tip: (a) SPM image; (b) P-H curves with $a/R=0.2$; (c) P-H curves with $a/R=0.3$; (d) P-H curves with $a/R=0.4$; (e) Comparison of all P-H curves.

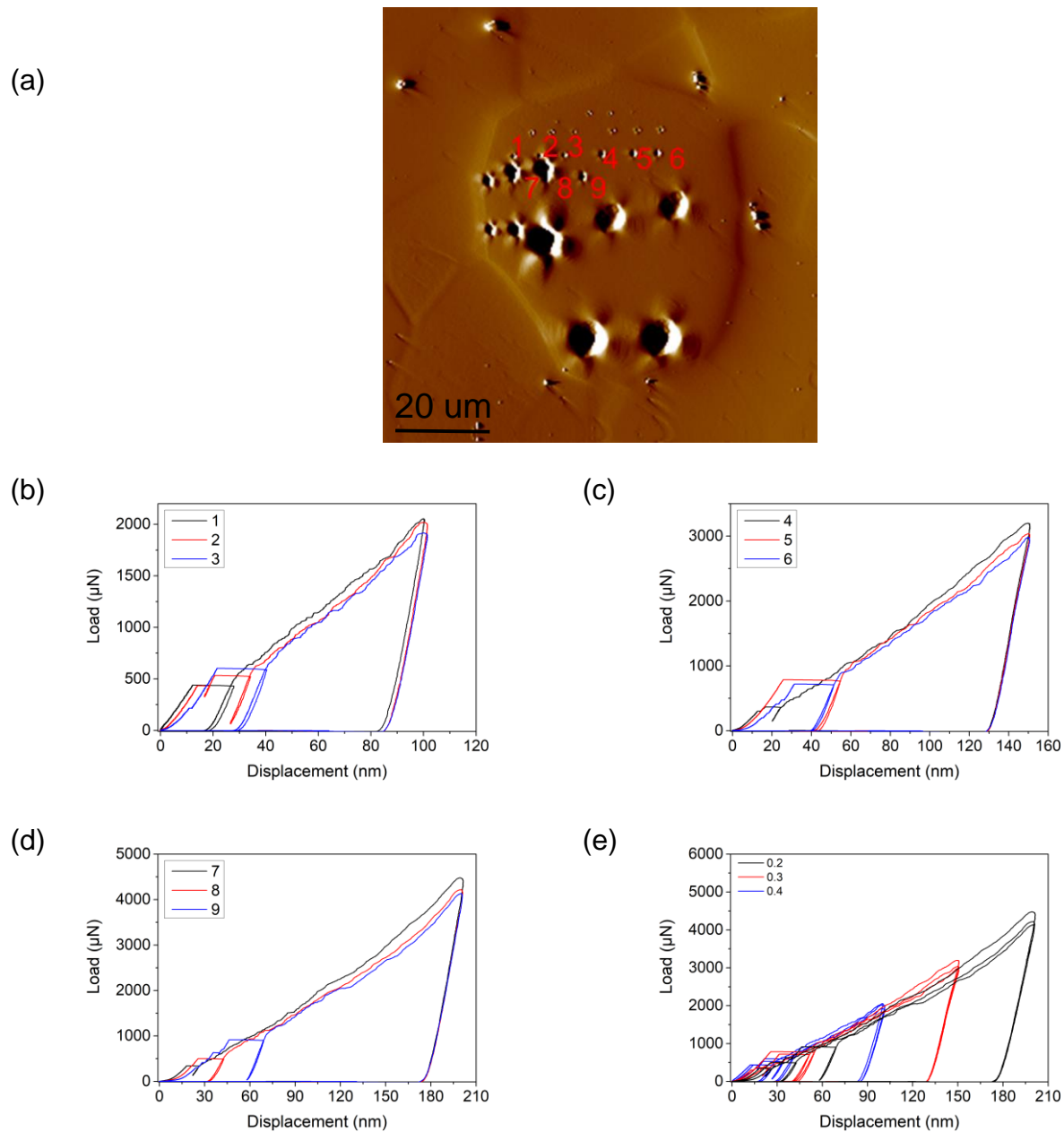


Fig. 5.7 Indentation tests in grain 4200 with 2 μm tip: (a) SPM image; (b) P-H curves with $a/R=0.2$; (c) P-H curves with $a/R=0.3$; (d) P-H curves with $a/R=0.4$; (e) Comparison of all P-H curves.

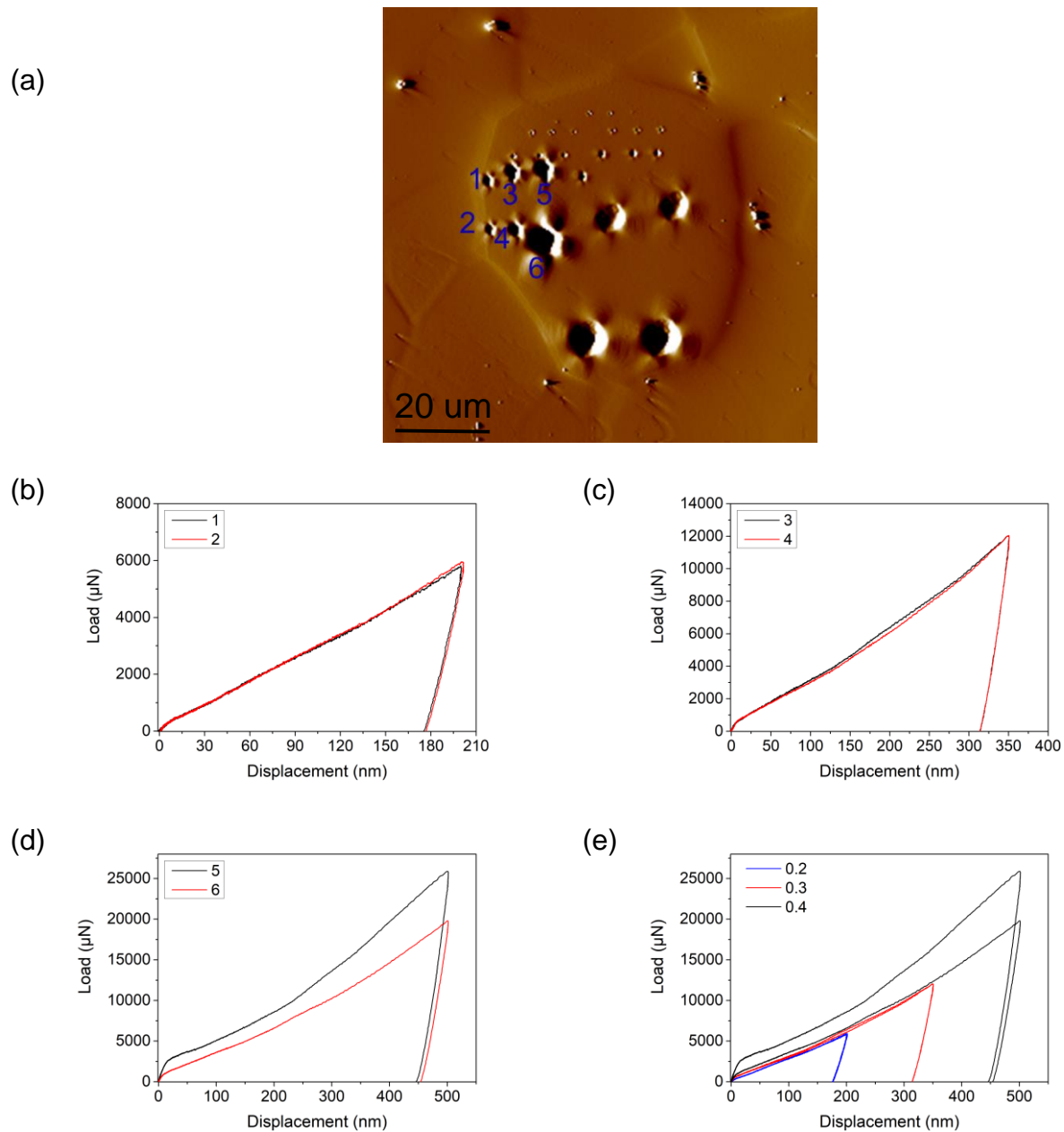


Fig. 5.8 Indentation tests in grain 4200 with $5 \mu\text{m}$ tip: (a) SPM image; (b) P-H curves with $a/R=0.2$; (c) P-H curves with $a/R=0.3$; (d) P-H curves with $a/R=0.4$; (e) Comparison of all P-H curves.

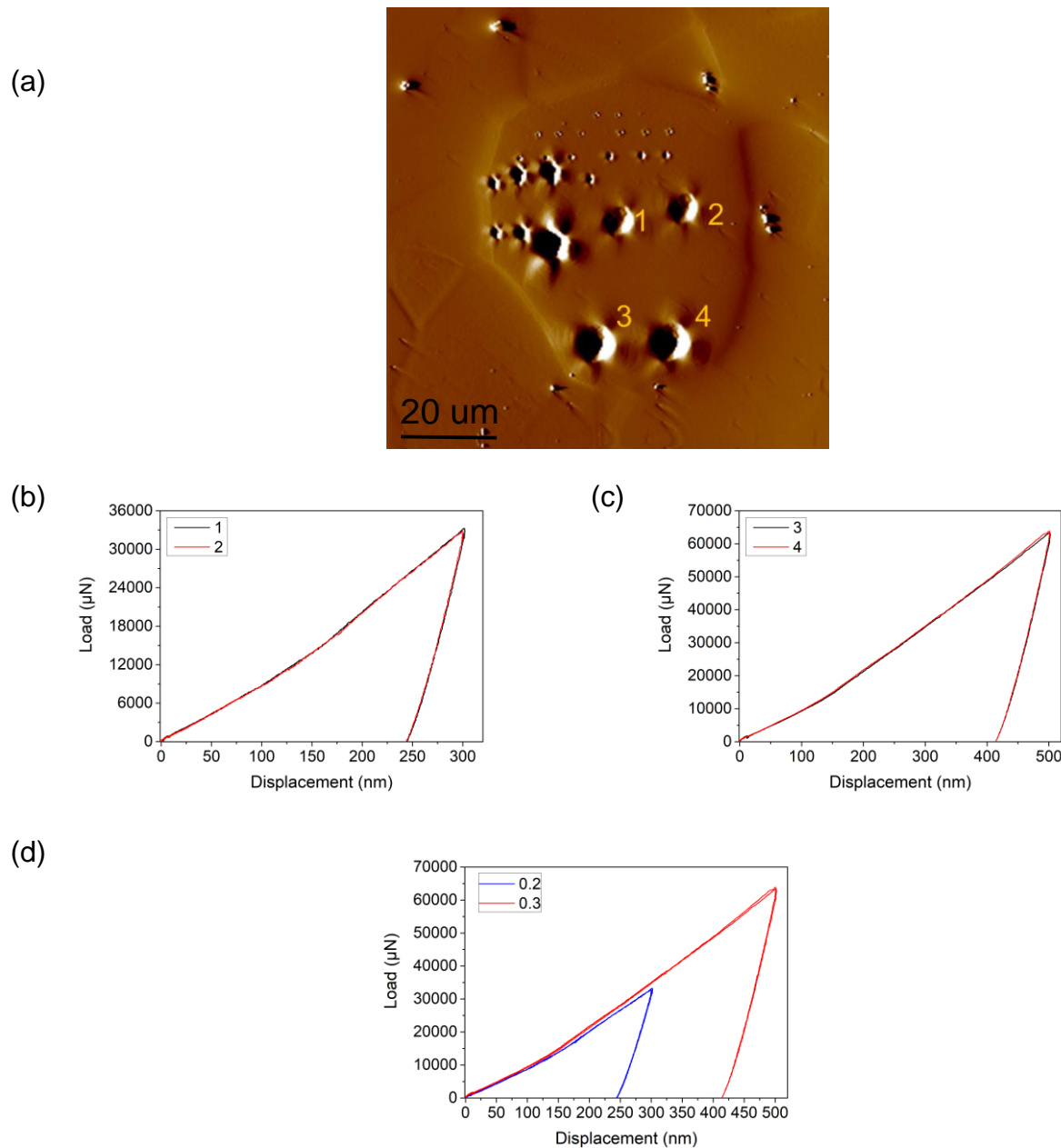


Fig. 5.9 Indentation tests in grain 4200 with 20 μm tip: (a) SPM image; (b) P-H curves with $a/R=0.2$; (c) P-H curves with $a/R=0.3$; (d) Comparison of all P-H curves.

The mechanical properties of crystalline metals are orientation dependent. From the peak loads between the two tested grains, as displayed in Fig. 5.10, it can be concluded that the peak loads of grain 4833 are higher than that of grain 4200 for all tips, which indicate the grains near $\{111\}$ orientation have higher strength and hardness than the grains near $\{100\}$. This experimental result is consistent with the theoretic result calculated based on Schmid's law. The $\{100\}$ orientation has a larger

Schmid factor when compression occurs along ND direction, the slip systems will be activated first and carries the plastic deformation. It should be mentioned that the stress field around the indenter is much more complex than in a uniaxial tensile or compression test, but the location where the initial yielding occurs coincides with that in compression along the loading direction.

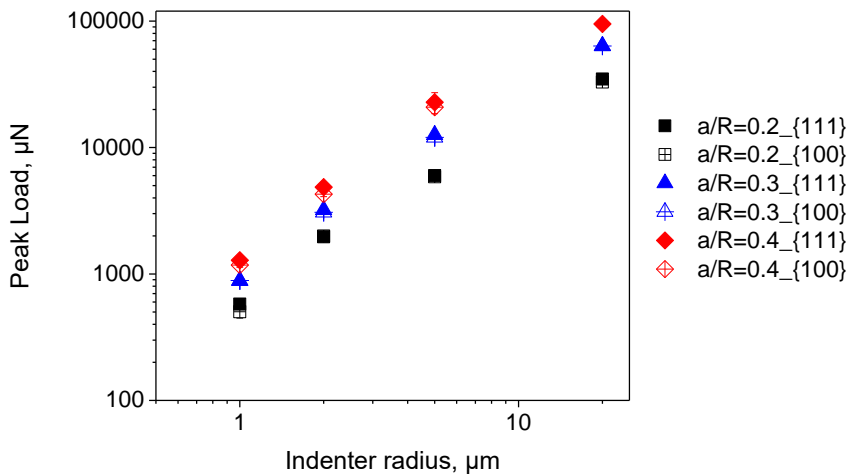


Fig. 5.10 Comparison of peak loads of grain 4833 and grain 4200.

There are noticeable displacement excursions and load drops in the P-H curves of 1 μm and 2 μm indentation tests. These events are called ‘pop-in’, which have been observed in many indentation tests. The displacement burst can be attributed to the sudden yielding of the material under load, which implies the onset of large scale dislocation motion or nucleation of dislocations. It can be observed that there are several successive pop-in events during one test. After the first pop-in, the deformation transfer from pure-elastic to plastic-elastic regime. In this experiment, all the tests are displacement-controlled, the controller of the machine detects the abnormal excursion of displacement and lift the indenter, which leads to the decrease of displacement and dramatical drop of load in the P-H curve. After a short response time, the displacement and the load arise in order to return to the defined displacement and continue the loading process. The pop-in events are difficult to observe in the experiments with 5

μm and $20 \mu\text{m}$, as the high-load transducer is controlled by a spring with ultra-high stiffness, the displacement and load recovery can be finished within a very short time. The force when pop-in occurs is called pop-in force. As seen in Fig. 5.11, the pop-in force increases with increasing indenter radius, which agrees with the Hertzian contact theory that the Peak load and indenter radius has a relationship of: $P \propto R^{\frac{1}{2}}$.

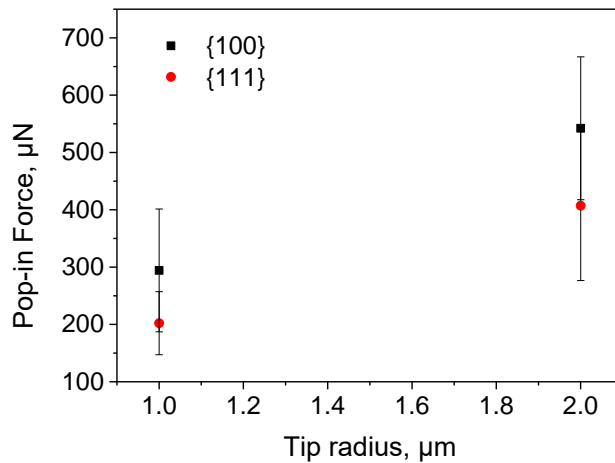


Fig. 5.11 Pop-in Force with increasing indenter radius.

5.2 Pile-up

From the post in-situ SPM images, the surface topography in 2D and 3D around the indents can be obtained as shown in Fig. 5.12 to Fig. 5.19. It is noticeable that the grain with $\{100\}$ orientation, grain 4200, displays symmetric four-fold pile-ups regardless of the tip radius. As for the grain 4833, whose orientation is near to $\{111\}$, the four-fold pile-up patterns are observable as well, but the pile-ups along three directions are stronger than another direction.

The 3D surface topography images give a more distinct view of the differences of pile-up patterns between the two orientations. The corresponding pile-up profiles are extracted from the 3D images as well. It can be concluded that the patterns of grain 4200 display higher degree of symmetry than grain 4833. The indenter radius has no influence on the topography of the pile up, as all the conical-spherical tips used here

are geometrically symmetric. The accumulated height increases with increasing penetration depth as more material is transported to the surface with larger penetration depth.

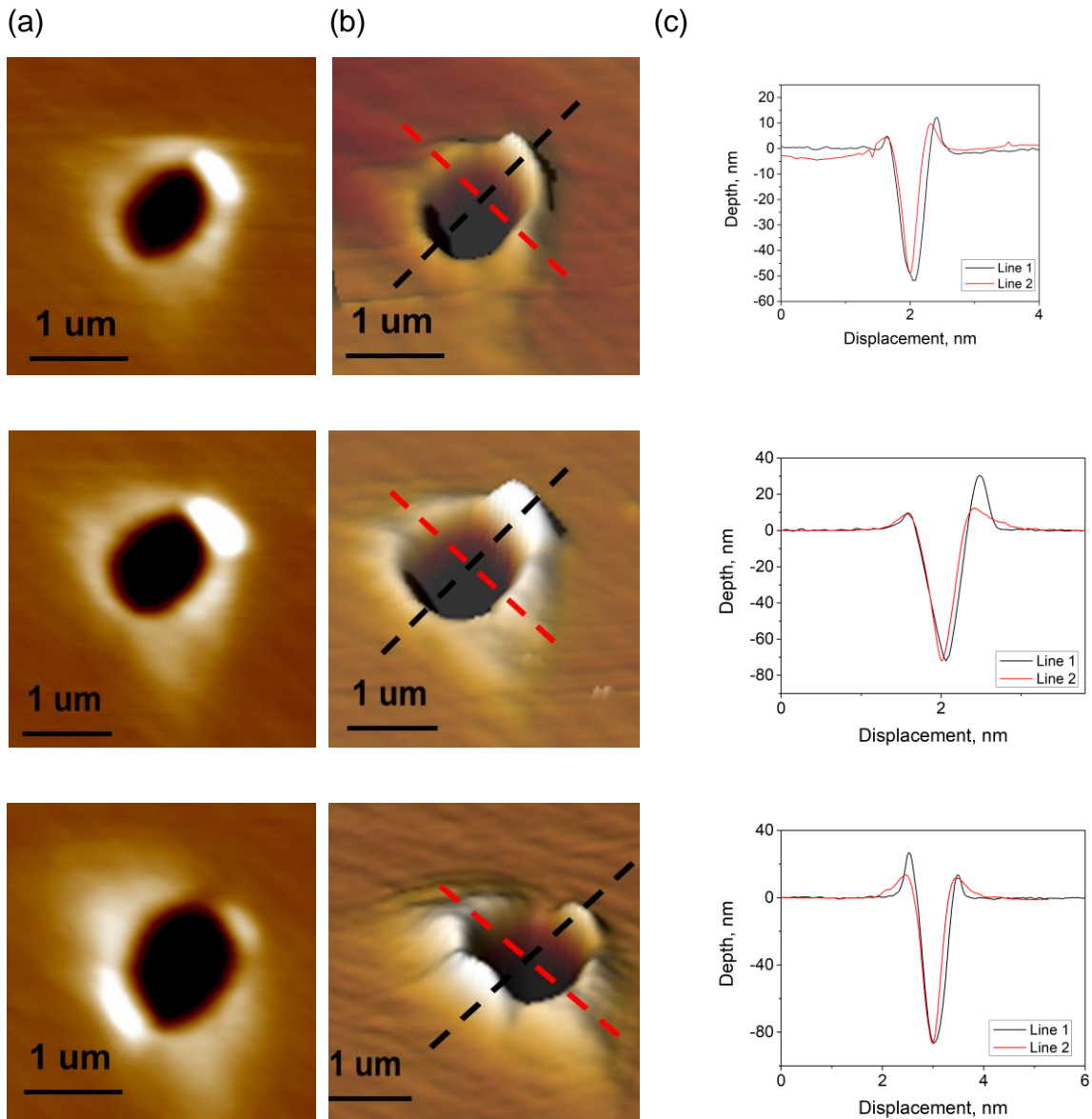


Fig. 5.12 Pile-ups around indents for grain 4833 with 1 μm indenter: (a) 2D SPM image (b) 3D SPM image; (c) Pile-up profiles. (First row: indentation strain of 0.2; Second row: indentation strain of 0.3; Third row: indentation strain of 0.4)

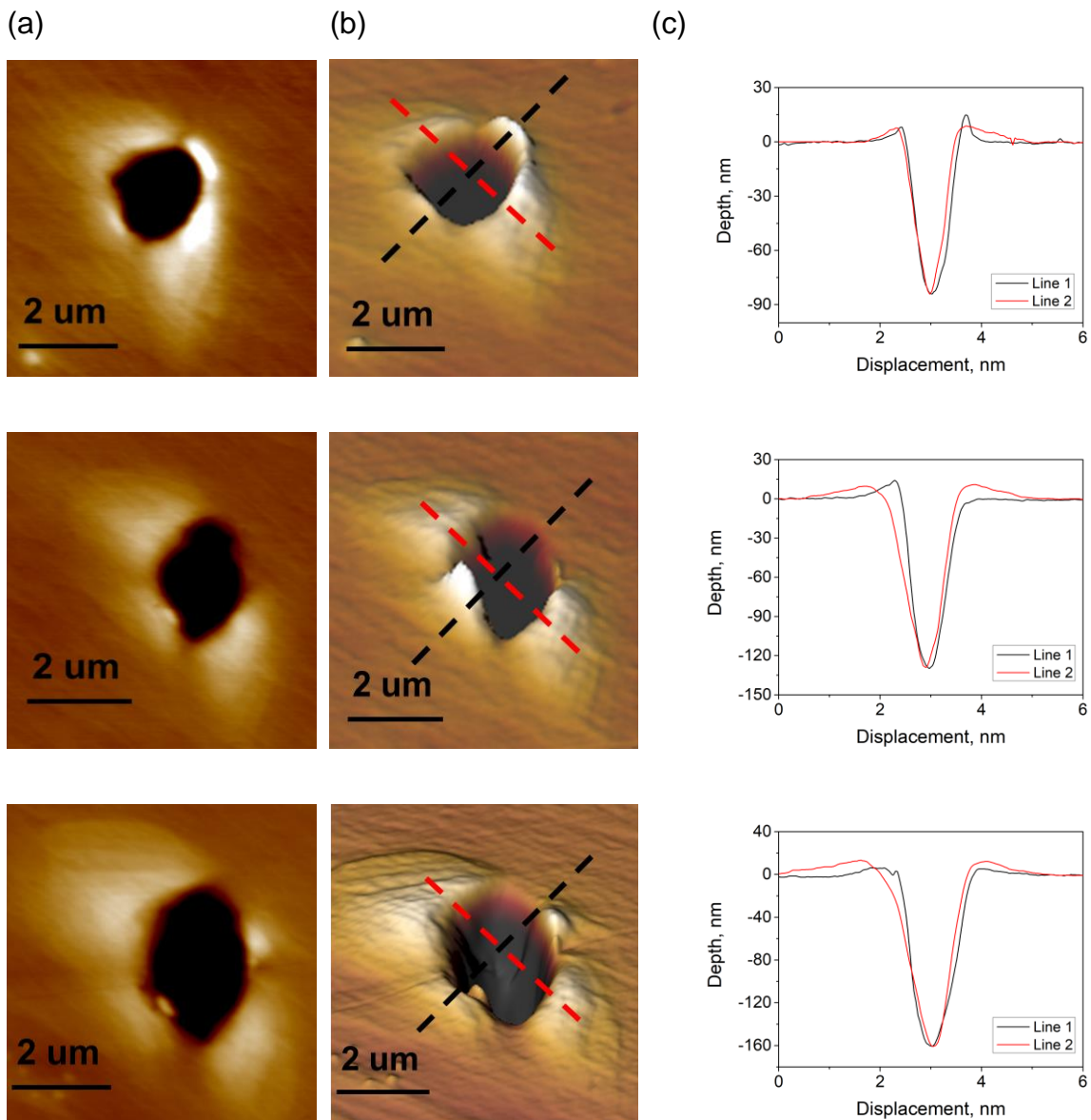


Fig. 5.13 Pile-ups around indents for grain 4833 with 2 μm indenter: (a) 2D SPM image (b) 3D SPM image; (c) Pile-up profiles. (First row: indentation strain of 0.2; Second row: indentation strain of 0.3; Third row: indentation strain of 0.4).

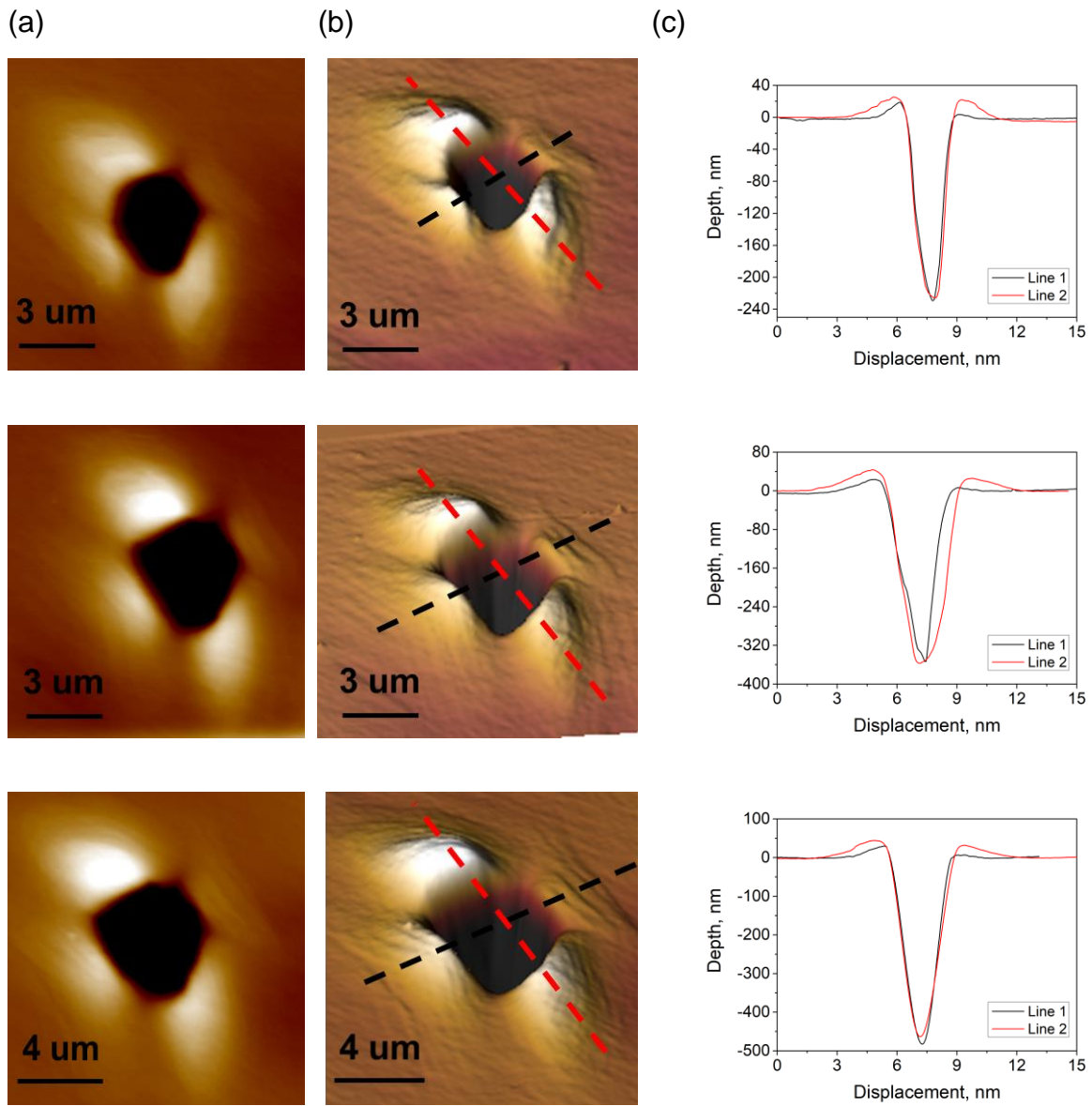


Fig. 5.14 Pile-ups around indents for grain 4833 with 5 μm indenter: (a) 2D SPM image (b) 3D SPM image; (c) Pile-up profiles. (First row: indentation strain of 0.2; Second row: indentation strain of 0.3; Third row: indentation strain of 0.4).

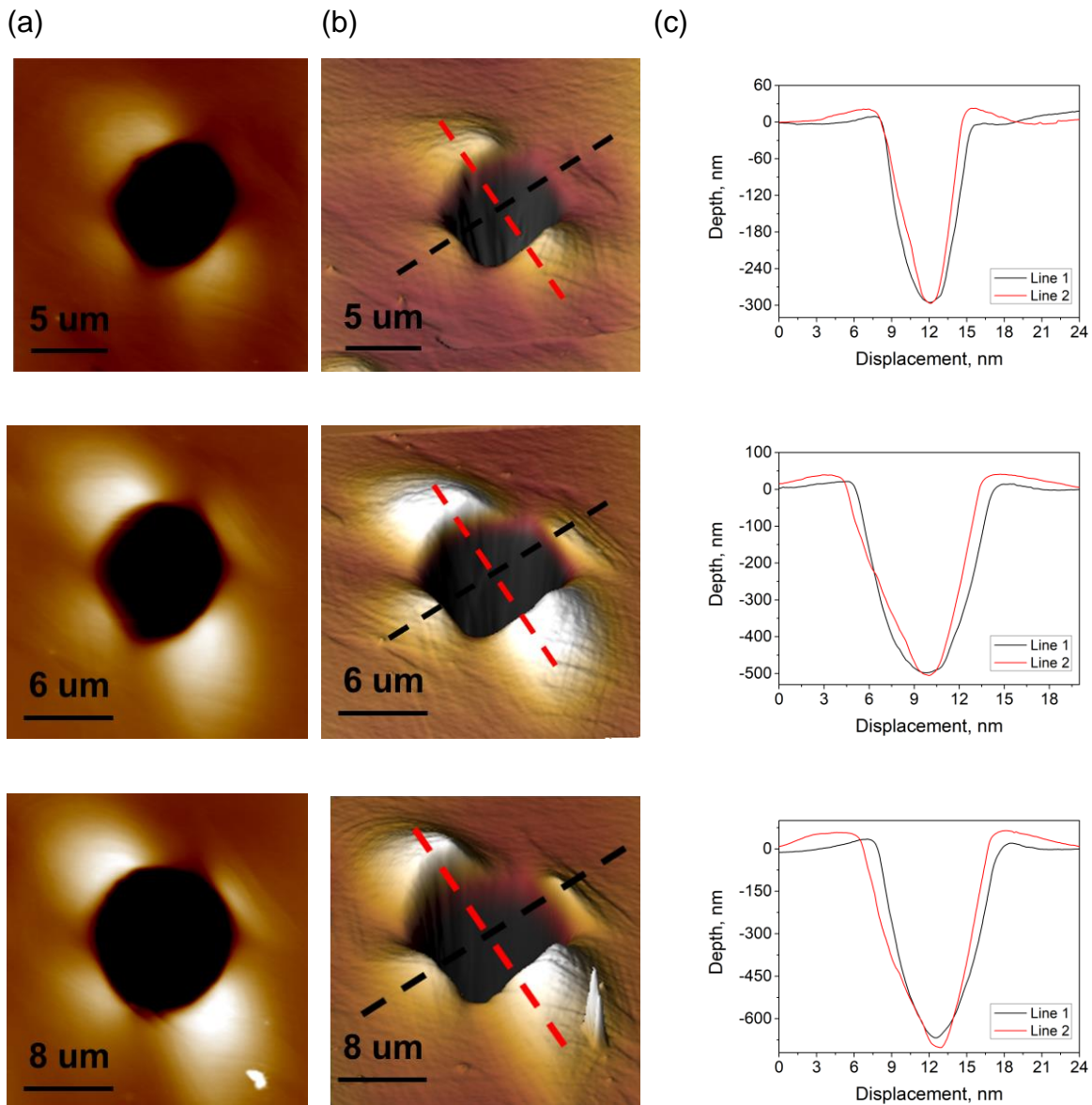
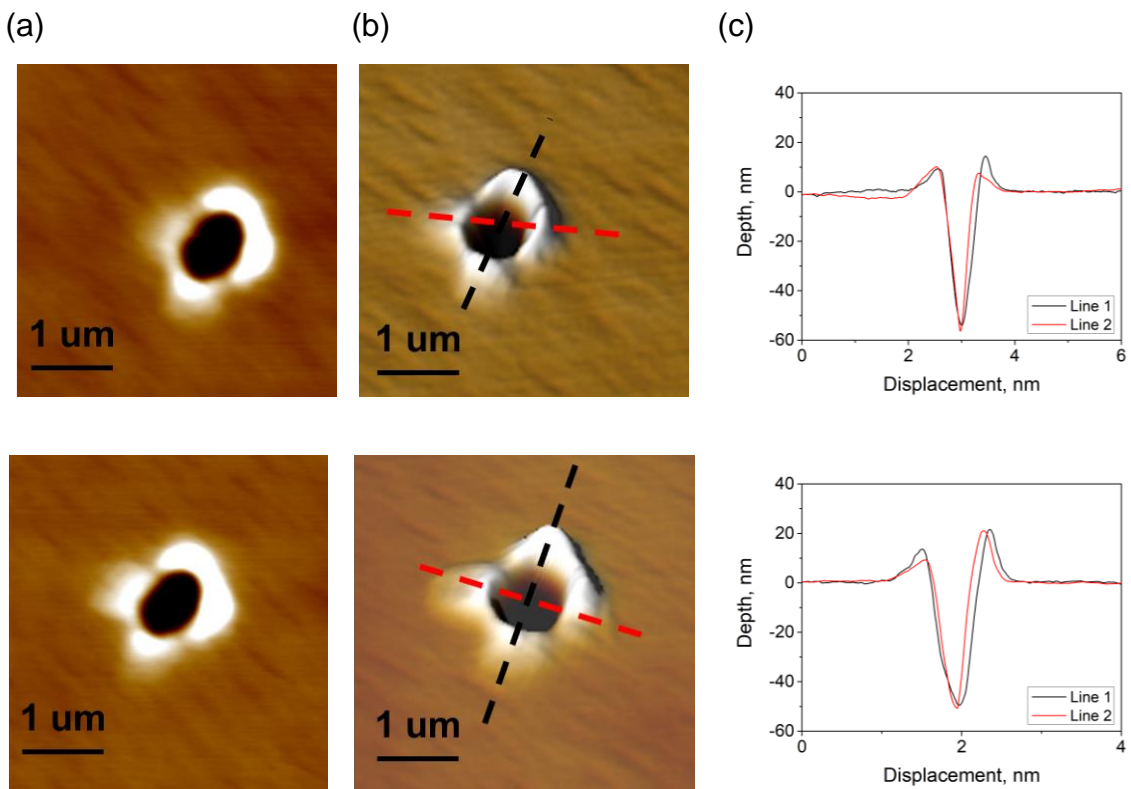


Fig. 5.15 Pile-ups around indents for grain 4833 with 20 μm indenter: (a) 2D SPM image (b) 3D SPM image; (c) Pile-up profiles. (First row: indentation strain of 0.2; Second row: indentation strain of 0.3; Third row: indentation strain of 0.4).

The distribution and symmetry of pile-up patterns are heavily dependent on the crystallographic orientation of the target grain due to activated slip systems. For BCC crystals, there are 12 $\{110\} < 111 >$ slip systems, 12 $\{112\} < 111 >$ slip systems and 24 $\{123\} < 111 >$ slip systems. The conical-spherical tip used here can avoid symmetries others than those of the crystal structure. For indentation in $\{100\}$ grain, there are four

out-of-plane slip directions on {110} slip direction which are firstly activated. The dislocation slip along the slip directions on the primary glide planes naturally produces excess material in the intersection areas between slip planes and indented surface, which leads to the formation of four-fold symmetry of surface pile-up. For indentation in grain near {111}, all the {110} slip direction on <111> slip plane are in-plane, in this case, the three out-of-plane {112} <111> slip systems are activated firstly, which leads to a three-fold symmetry pile-up patterns. But the grain 4833 is not perfectly located at {111} orientation. It locates between the {100} and {111} in the IPF triangle, which makes the activated slip systems more complex. The pile-up pattern is neither four-fold nor three-fold symmetry, but an intermediate shape. The abnormal shape of P-H curves at the bottom of indents, as seen in Fig. 5.9 (c) is either caused by the deviation of selected direction form the central bottom or by the signal feedback issues during scanning.



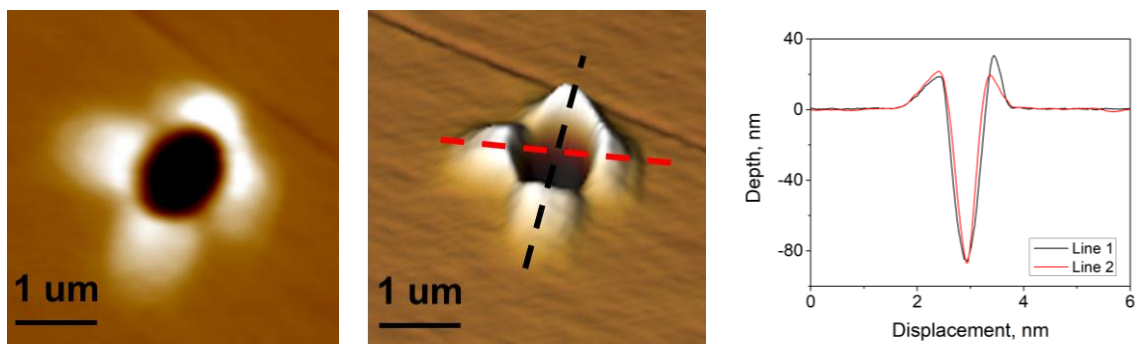
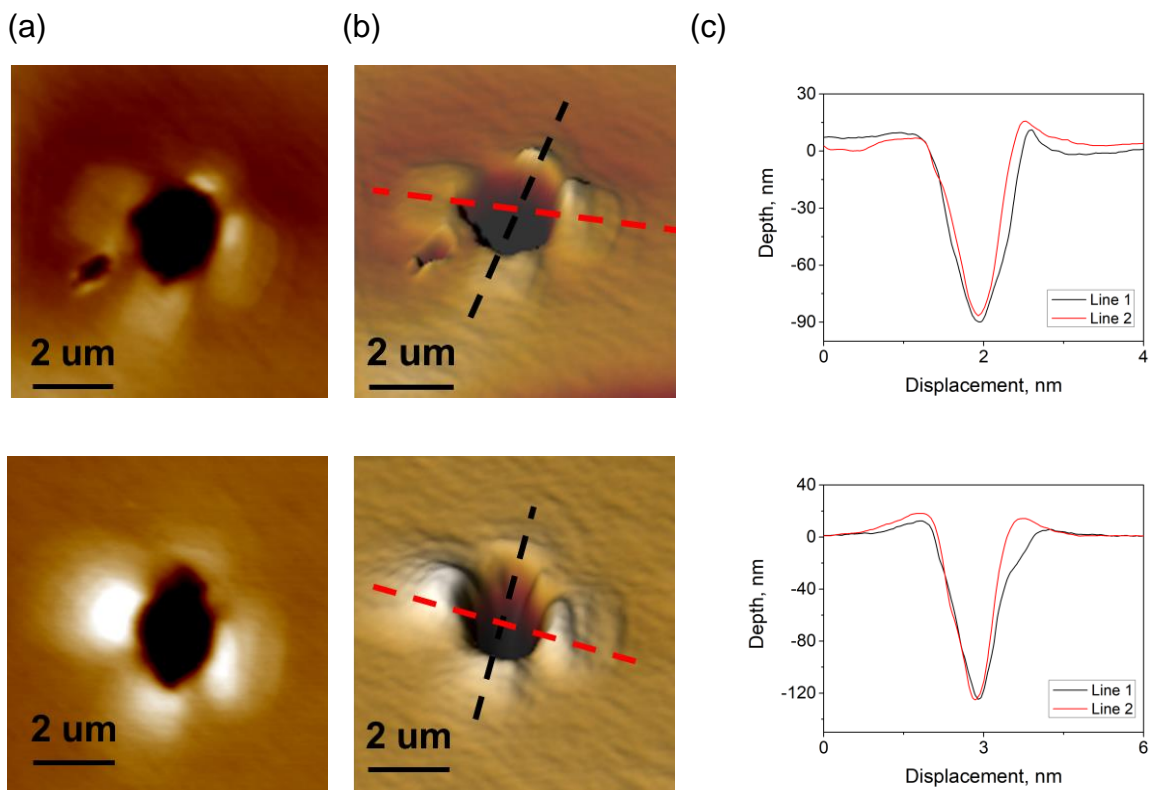


Fig. 5.16 Pile-ups around indents for grain 4200 with 1 μm indenter: (a) 2D SPM image (b) 3D SPM image; (c) Pile-up profiles. (First row: indentation strain of 0.2; Second row: indentation strain of 0.3; Third row: indentation strain of 0.4).



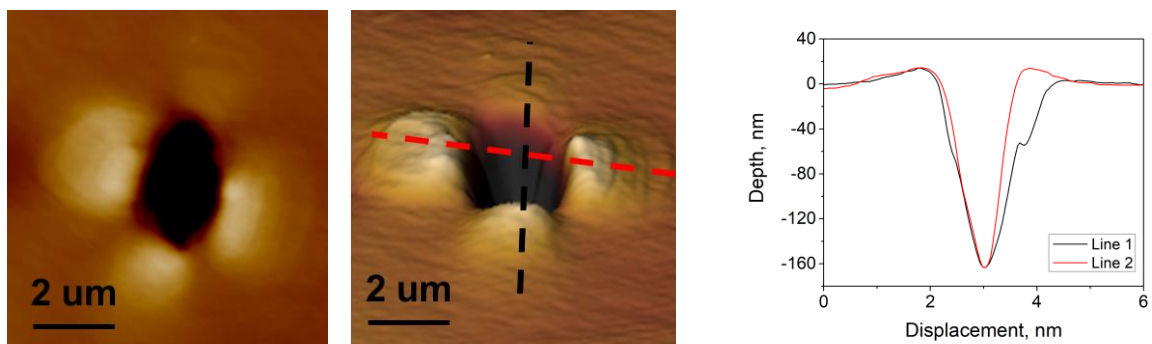


Fig. 5.17 Pile-ups around indents for grain 4200 with 2 μm indenter: (a) 2D SPM image (b) 3D SPM image; (c) Pile-up profiles. (First row: indentation strain of 0.2; Second row: indentation strain of 0.3; Third row: indentation strain of 0.4).

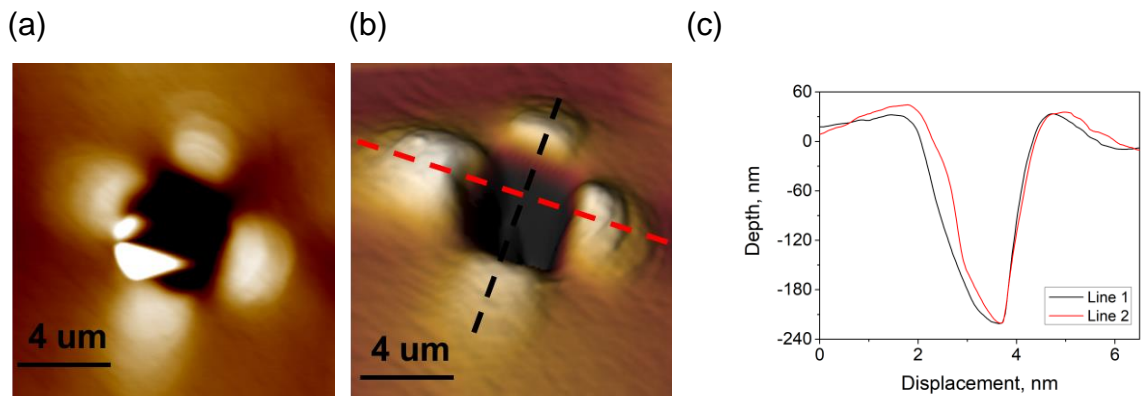


Fig. 5.18 Pile-ups around indents for grain 4200 with 5 μm indenter at indentation strain of 0.2: (a) 2D SPM image (b) 3D SPM image; (c) Pile-up profiles.

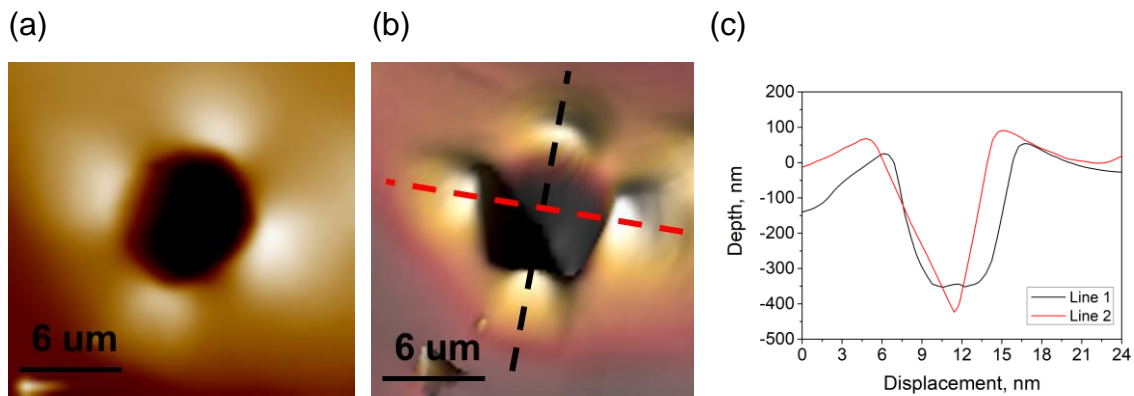


Fig. 5.19 Pile-ups around indents for grain 4200 with 20 μm indenter at indentation strain of 0.2: (a) 2D SPM image (b) 3D SPM image; (c) Pile-up profiles.

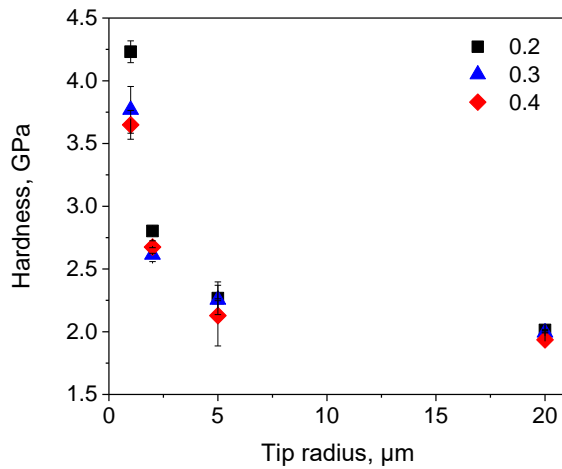
5.3 Hardness

After indentation tests, the hardness values can be extracted from the recorded P-H curves with Eq.2.1 to Eq.2.9. Fig. 5.20 provides the hardness values with various tip radius of two grains. A prominent size effect can be observed that the hardness values decrease with increasing indenter radius for the indentation strain from 0.2 to 0.4. This trend is observed in both grains. The results agree with the theory proposed by Swadener. The average density of the GNDs generated during compression is given by:

$$\rho_G = \frac{1}{bR} \quad \text{Eq. 5.1}$$

The increasing dislocation density with smaller indents leads to higher shear strength and hardness value.

(a)



(b)

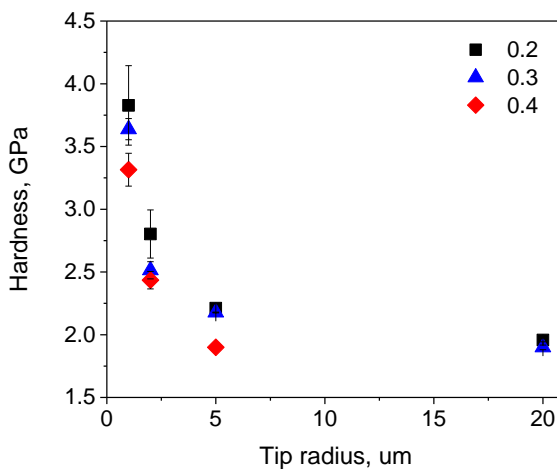


Fig. 5.20 Hardness with different tip radius at various indentation strain: (a) grain 4833; (b) grain 4200.

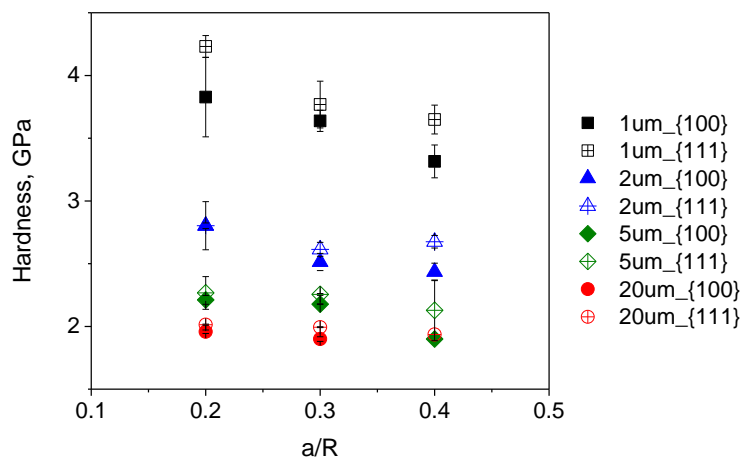


Fig. 5.21 Hardness with different indentation strain a/R at various tip radius.

It can be observed that the decrease of hardness has a trend to reach a plateau, the hardness of indentation tests with 5 μm and 20 μm are close. This can be explained by Eq. 2.20. The hardness will finally reach the microhardness H_0 with increasing indenter radius, and the ISE disappears.

Fig. 5.21 presents the hardness values with different indentation strain or penetration depth. It can be observed that the hardness decreases with increasing depth of penetration, which is also a size effect. The density of GNDs decreases with deeper penetration depth. However, as spherical indenter has no self-similarity, the strain induced in the material increase with penetration depth, leading to the work hardening of the steel. The density of SSDs increase, which compensate the decrease of hardness caused by GNDs. Therefore, the ISE observed with different penetration depth is much weaker compared to the variation of indenter radius.

6 Size effect study with crystal plasticity models

In this work, the nanoindentation model is built to simulate the experiment results by coupling to a local and a non-local crystal plasticity model via a user-defined material subroutine (UMAT) within Abaqus. The local and non-local crystal plasticity parameters are adapted to fit both load-displacement curves and residual surface topologies.

6.1 Simulation setup

There are four models built in total, which correspond to the four indenters used in the experiment (as shown in Fig. 6.1). The models consist of two parts, namely indenter and single crystal grain.

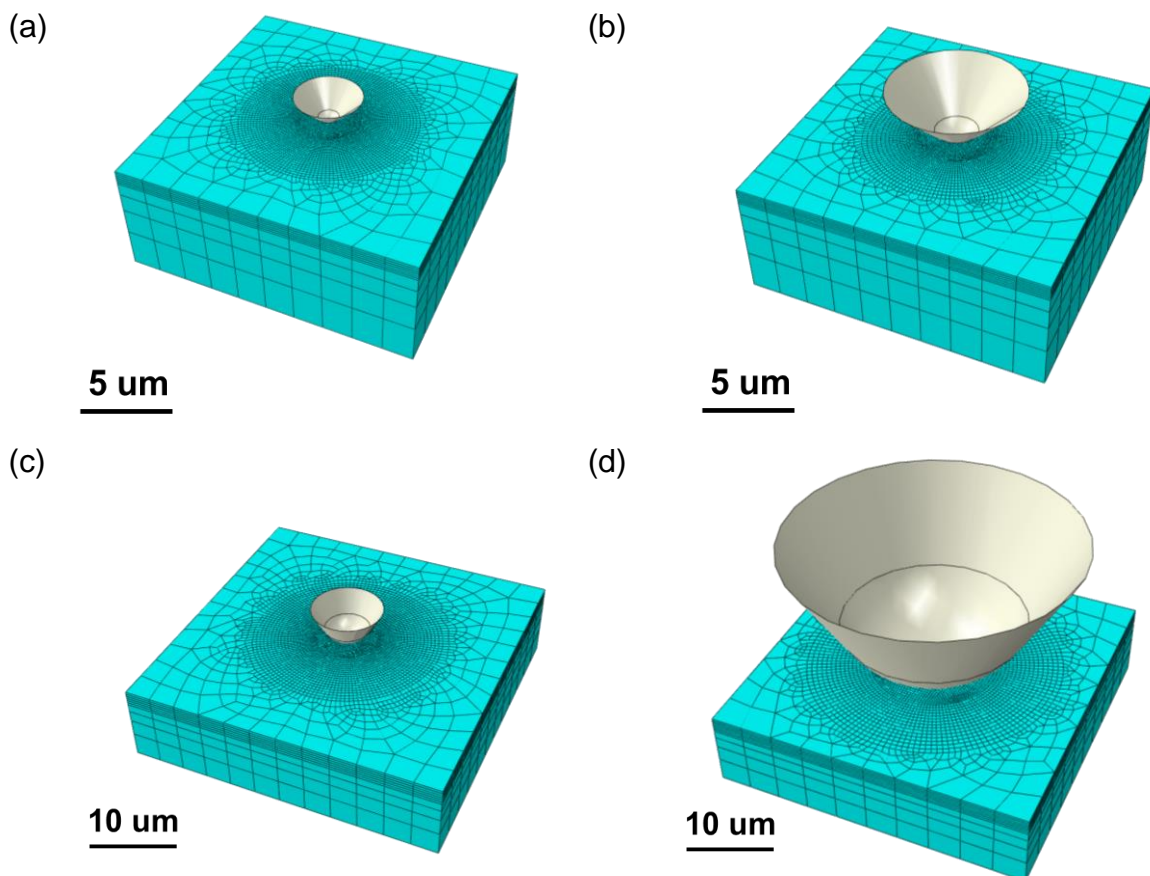


Fig. 6.1 3D nanoindentation models: (a) 1 μm tip; (b) 2 μm tip; (c) 5 μm tip; (d) 20 μm indenter.

The indenter part is a meshed discrete rigid body which has the same geometry as the indenter used in the experiment. The mesh size of the element is set differently with the four tips, but the size is always bigger than the mesh size of the grain part for each model, which can avoid mis-convergence problems during computation.

For the models with tip of 1, 2, and 5 μm , the dimensions of the grain are the same ($20 \times 20 \times 8 \mu\text{m}$). As for the 20 μm tip model, the grain part is relatively bigger ($60 \times 60 \times 15 \mu\text{m}$). The dimensions of the grain part are determined based on the dimensions of the plastic zone under the contact area at maximum penetration depth for different indentation tests.

The element type of the grain part is 8-node linear brick (C3D8). The grain is partitioned into center circle, outer circle and outer part, as demonstrated in Fig. 6.2. The center circle is ultra-fine meshed in order to capture the stress and strain field of the deformed area.

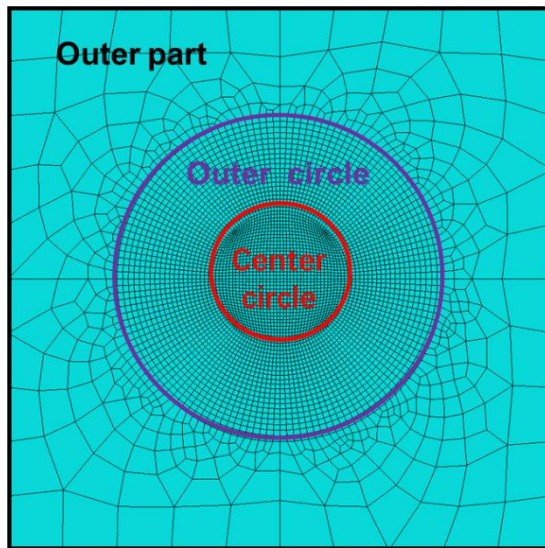


Fig. 6.2 Partitionion of the grain in the 3D model.

The diameter of the center circle and the mesh size of the element is different for the four models, as a bigger tip can lead to a larger deformed zone under contact area.

The total number of elements within the center circle are the same (1600 in total). The detailed size information of the model is listed in Tab. 6.1.

Tab. 6.1 Mesh size of the grain for all models.

Indenter radius (μm)	Total size (μm^3)	Diameter of center circle (μm)	Mesh size of center circle (μm)	Diameter of outer circle (μm)
1	20×20×8	4	0.1	12
2	20×20×8	5	0.125	12
5	60×60×15	12	0.3	36
20	60×60×15	24	0.6	48

The local CP model involves three group of parameters: strain rate related parameters ($\dot{\gamma}_0$, m), work hardening behavior related parameters (τ_s^c , a , h_0) and initial resolved shear strength τ_0 . The strain rate related parameters $\dot{\gamma}_0$ and m are set to 0.000278 ms^{-1} and 0.05 respectively in this work. Therefore, only the work hardening related parameters and τ_0 are calibrated in this study. For the non-local model, besides the local CP parameters, two additional non-local CP parameters, ℓ and Z , should be calibrated.

6.2 Local model

6.2.1 Parameterization

In this work, the working hardening parameters τ_s^c , a , h_0 should keep constant despite of the various of indenter or penetration depth. Only τ_0 should be changed with different indenter radius. Therefore, the working hardening parameters should first be calibrated and confirmed. By comparing the P-H curves of simulation and experiment results from grain 4833, the CP parameters are calibrated. The results from grain 4200 are used for validation of parameters.

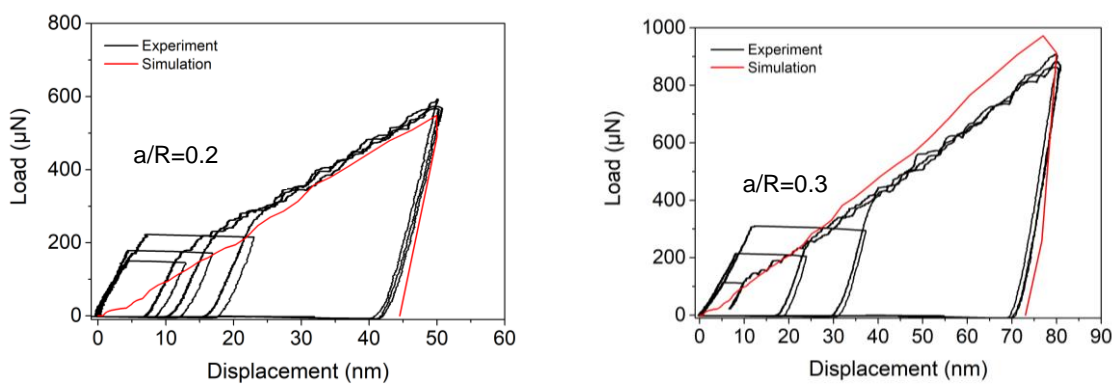
The calibrated CP parameters for different indenters are listed in Tab. 6.2. The comparison of experiment and numerical results are given in Fig. 6.3.

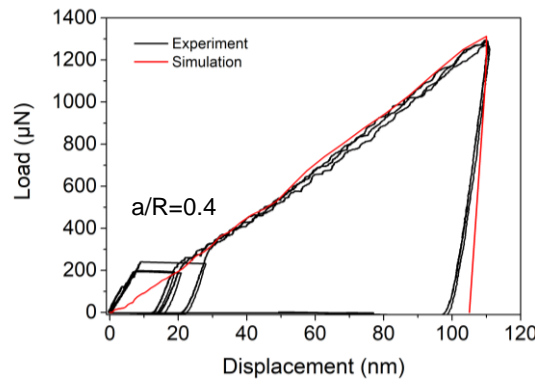
Tab. 6.2 Calibrated CP parameters.

Indenter	radius (μm)	τ_0 (MPa)	τ_s^c (MPa)	a	h_0 (MPa)	$\dot{\gamma}_0$ (ms^{-1})	m
1	165						
2	130						
5	68	240	1.2	550	0.00028	0.05	
20	62						

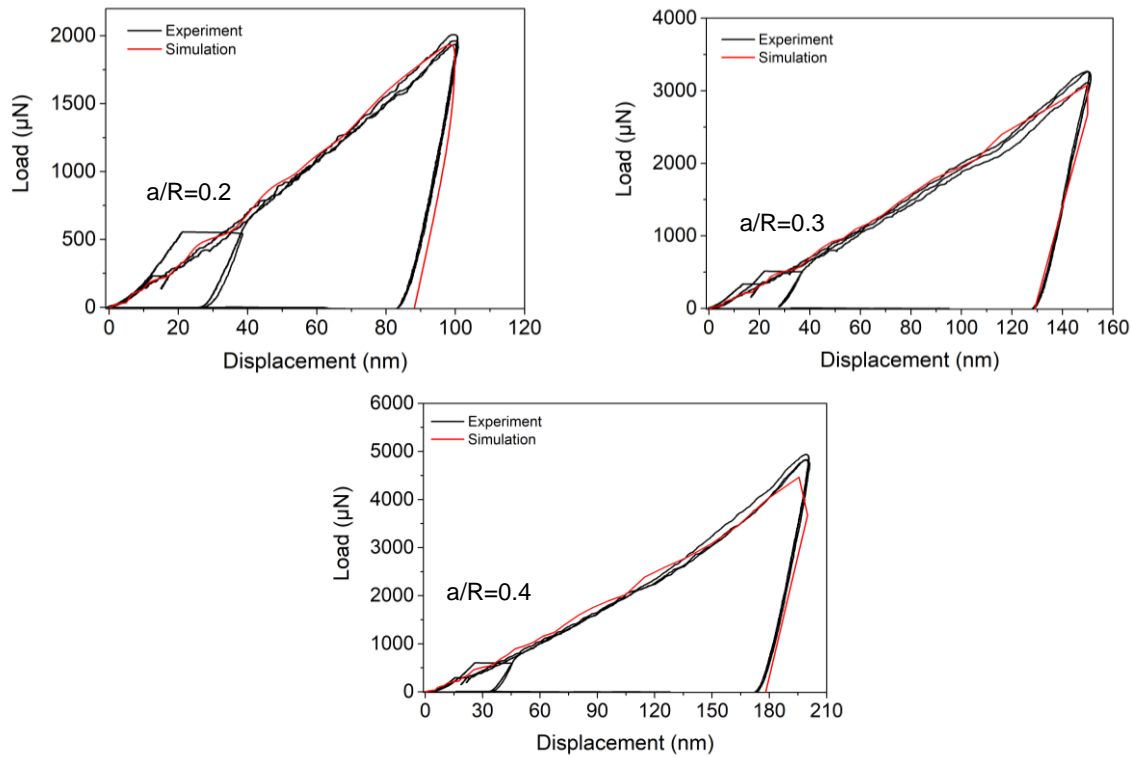
The simulation results reach the good agreement with the experimental P-h curves for various indenters. This proves that the ISE has been successfully captured by varying τ_0 in local model. The calibrated τ_0 decreases with increasing indenter radius, which has the same trend with the hardness. For the same indenter with different indentation strain, some deviations can be observed between simulation and experimental results. In this work, the CP parameters keep constant for the same indenter, which neglect the ISE with penetration depth. But the decrease of hardness caused by penetration depth is much smaller than the indenter radius, so the neglection is acceptable.

(a)

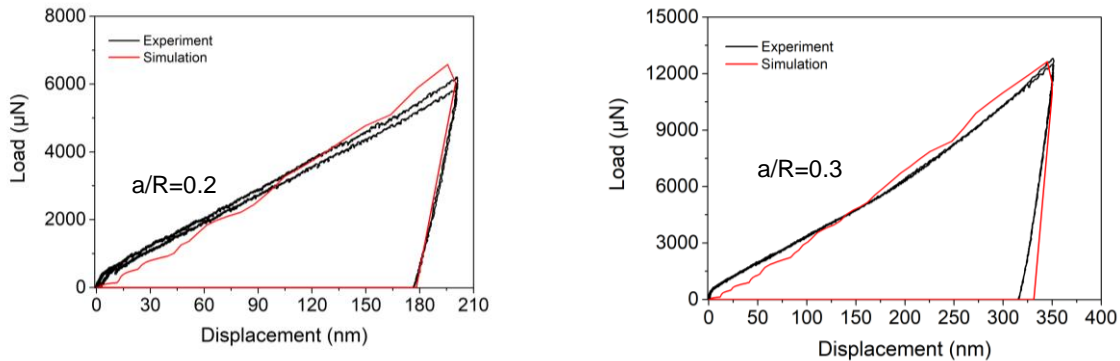




(b)



(c)



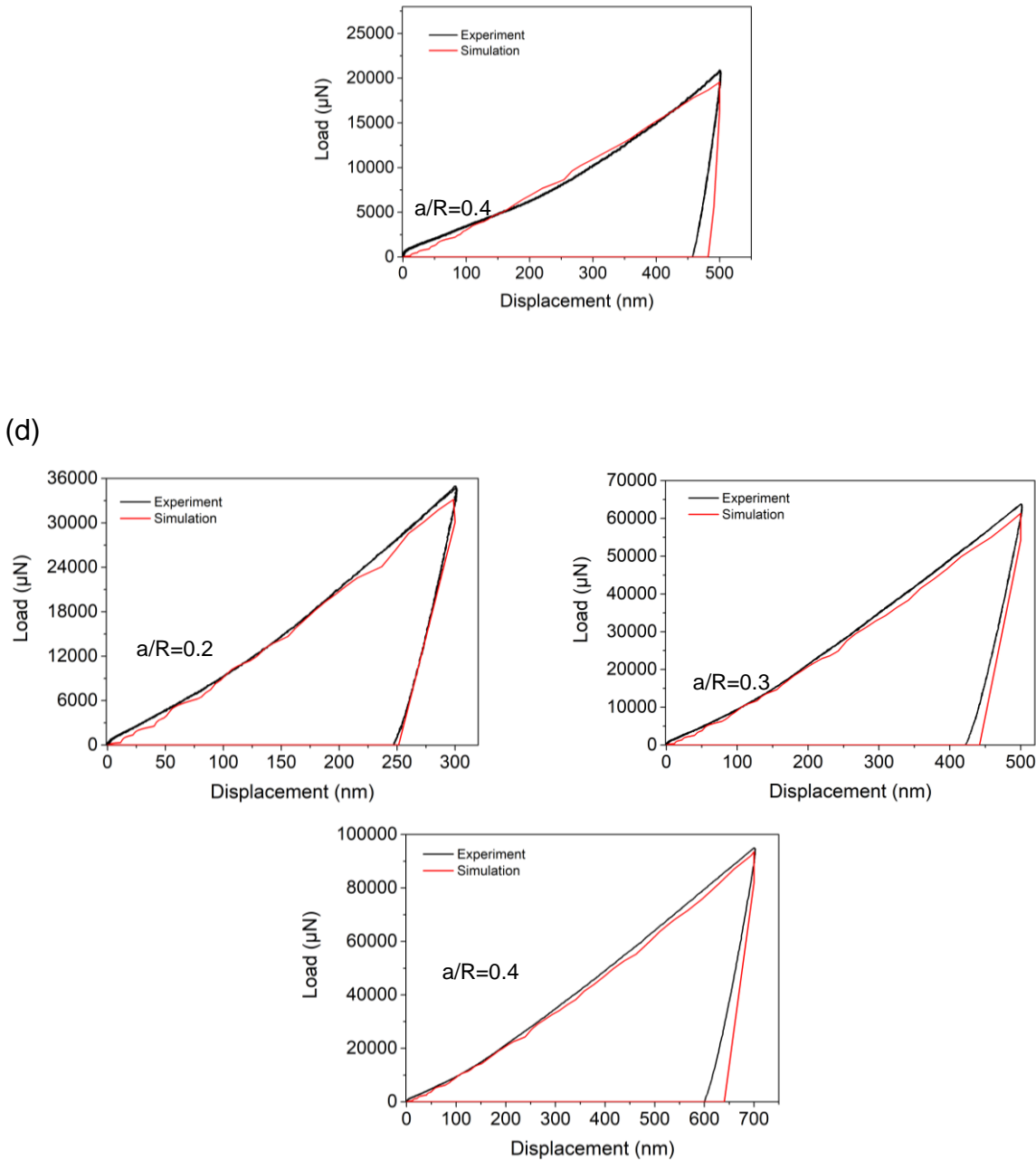
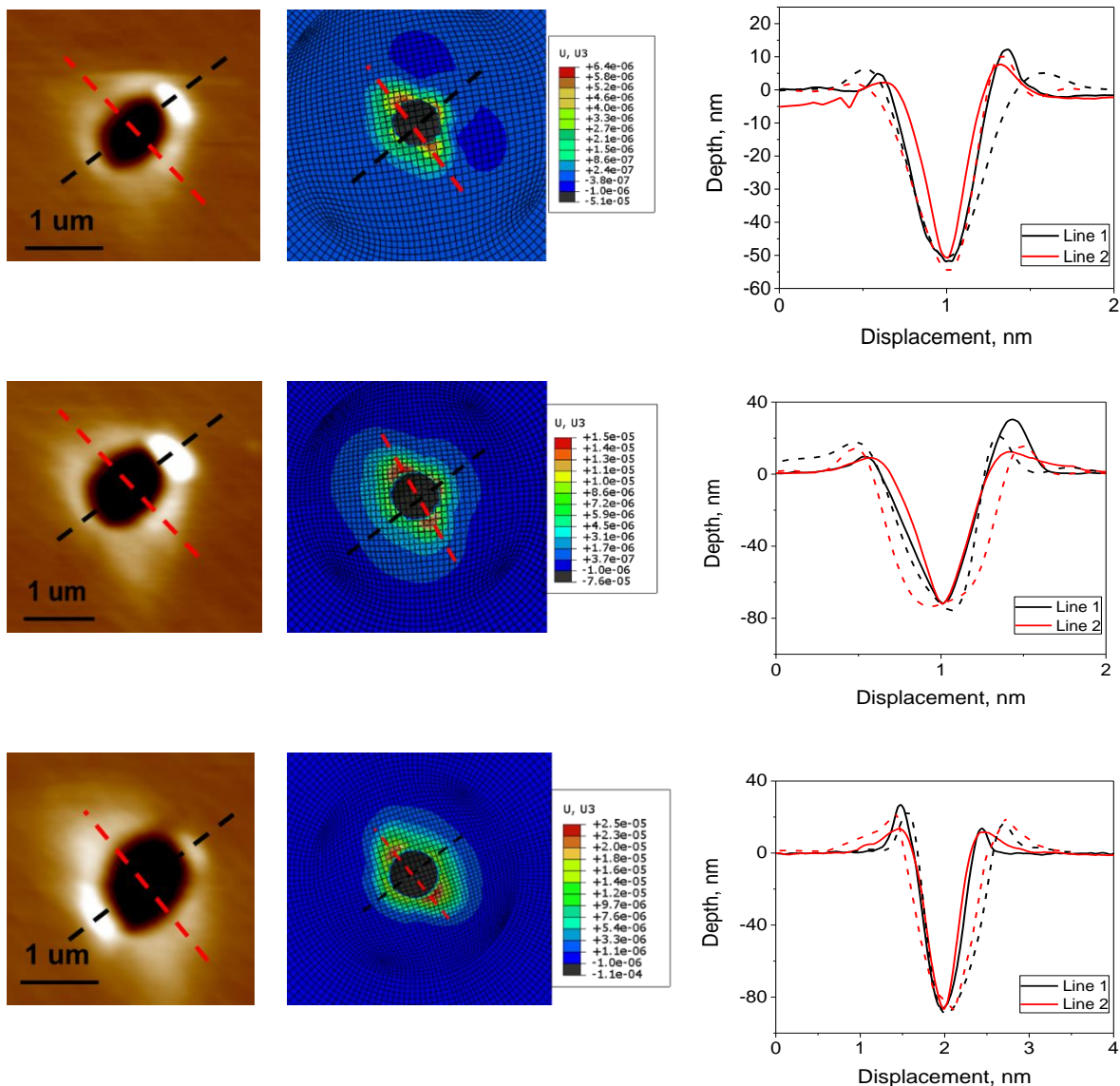


Fig. 6.3 The P-h curves of experiment and simulation of grain 4833: (a) 1 μm indenter; (b) 2 μm indenter; (c) 5 μm indenter; (d) 20 μm indenter.

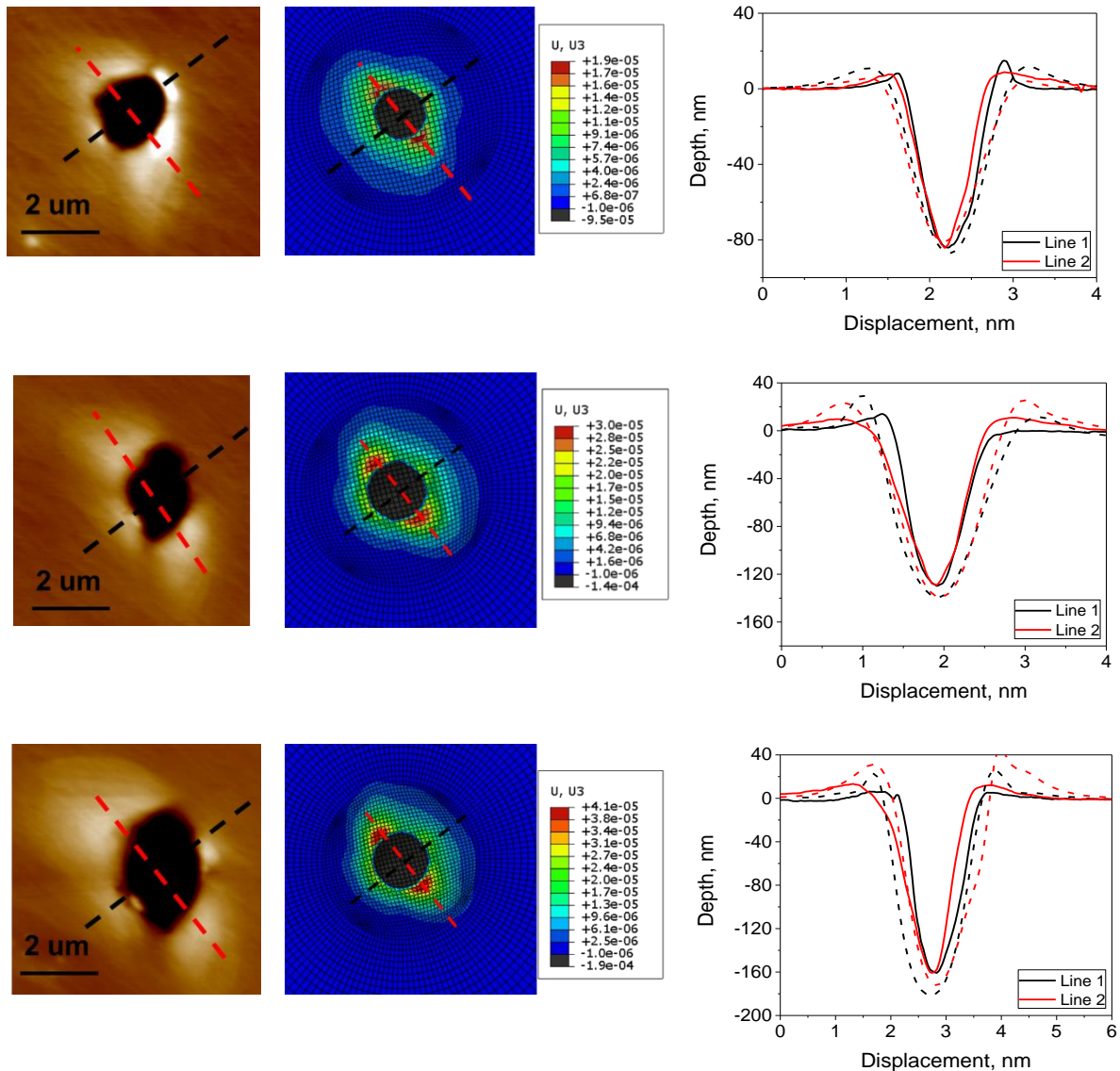
Fig. 6.4 shows the surface topography and pile-up patterns of numerical and experimental results. The topography around the indents are similar. This can also be concluded from the shape of pile-up profiles. However, the height of pile-ups from simulation results are larger than that from experiments. The difference is more obvious for 1 and 2 μm indenter. There are several reasons leading to the deviations. As all the indents are arranged closely within the grain during the experiment, the pile-

ups of different indents can interact. In addition, it can be observed that the radii of the residual impressions from experiment are slightly smaller than the simulation results, which indicates the real radius of the indenter is smaller than the theory value. Besides, due to the mechanical wearing after long-time usage, the top of the indenter is no longer a perfect sphere. The pile-up patterns are highly dependent on the shape of the indenter, a non-perfect sphere can influence the activated slip systems during deformation and lead to a different pile-up behavior.

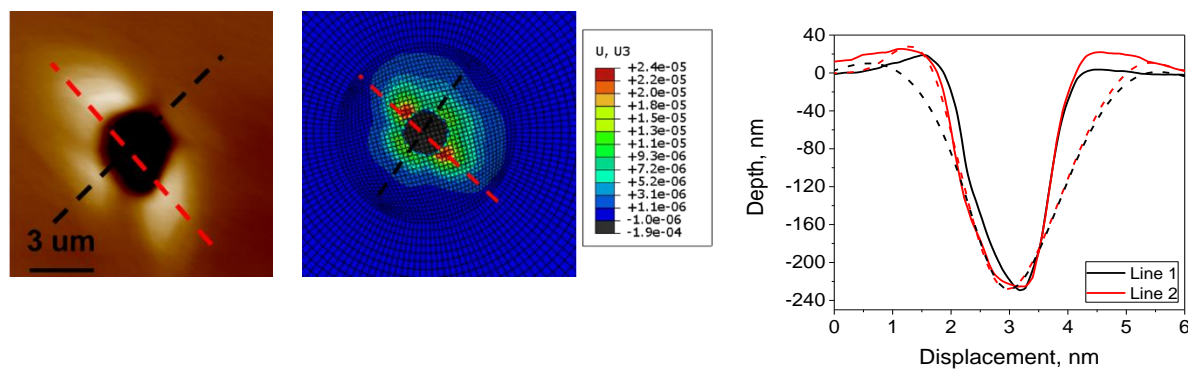
(a)

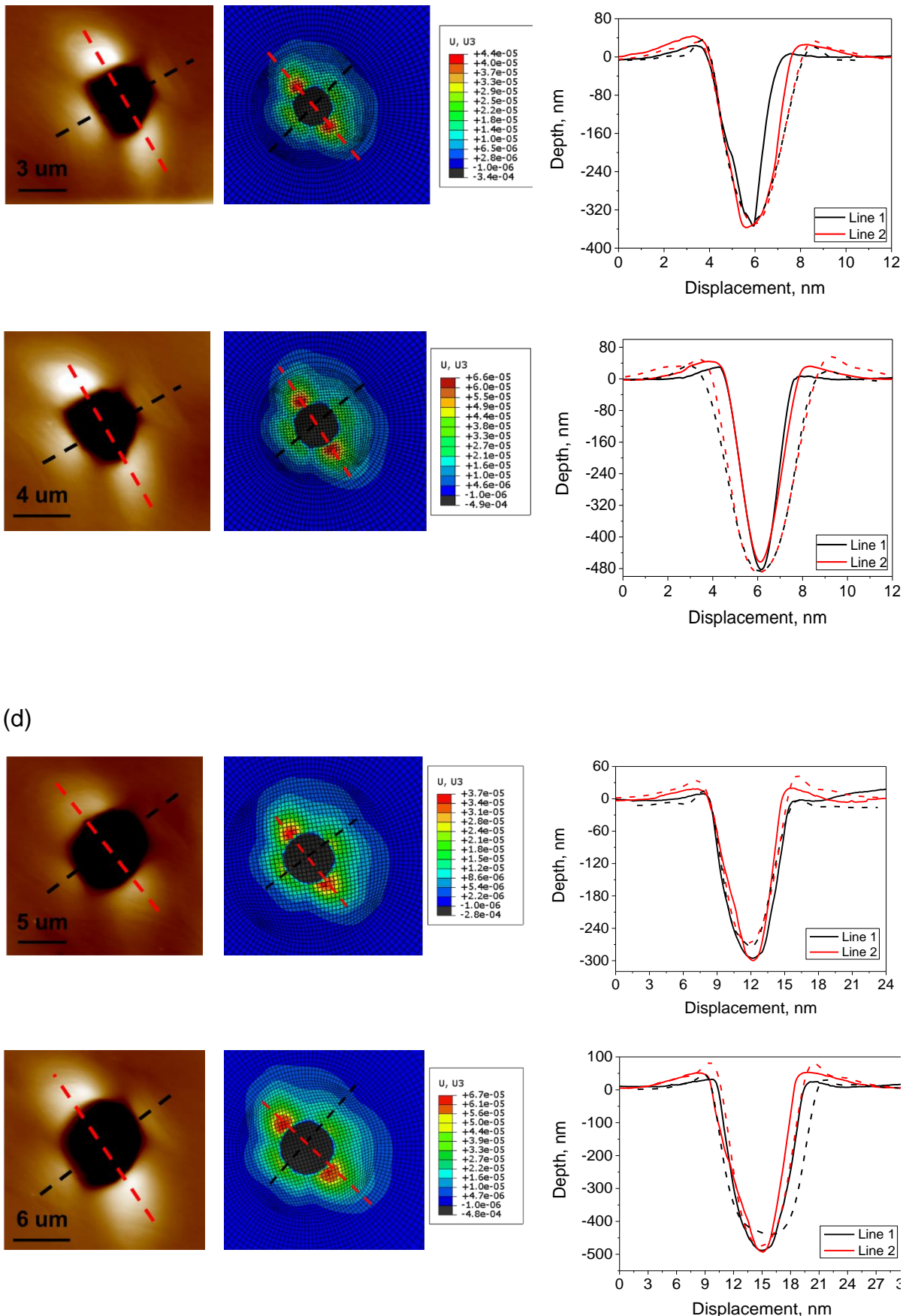


(b)



(c)





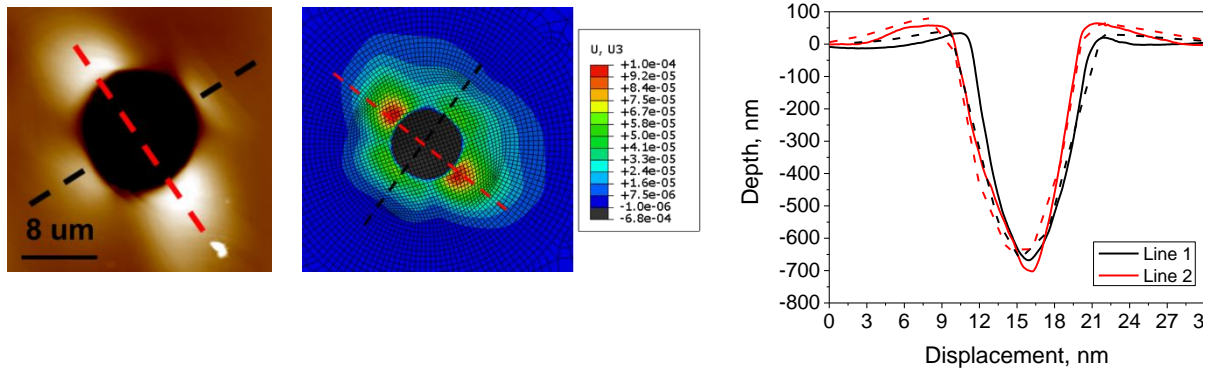
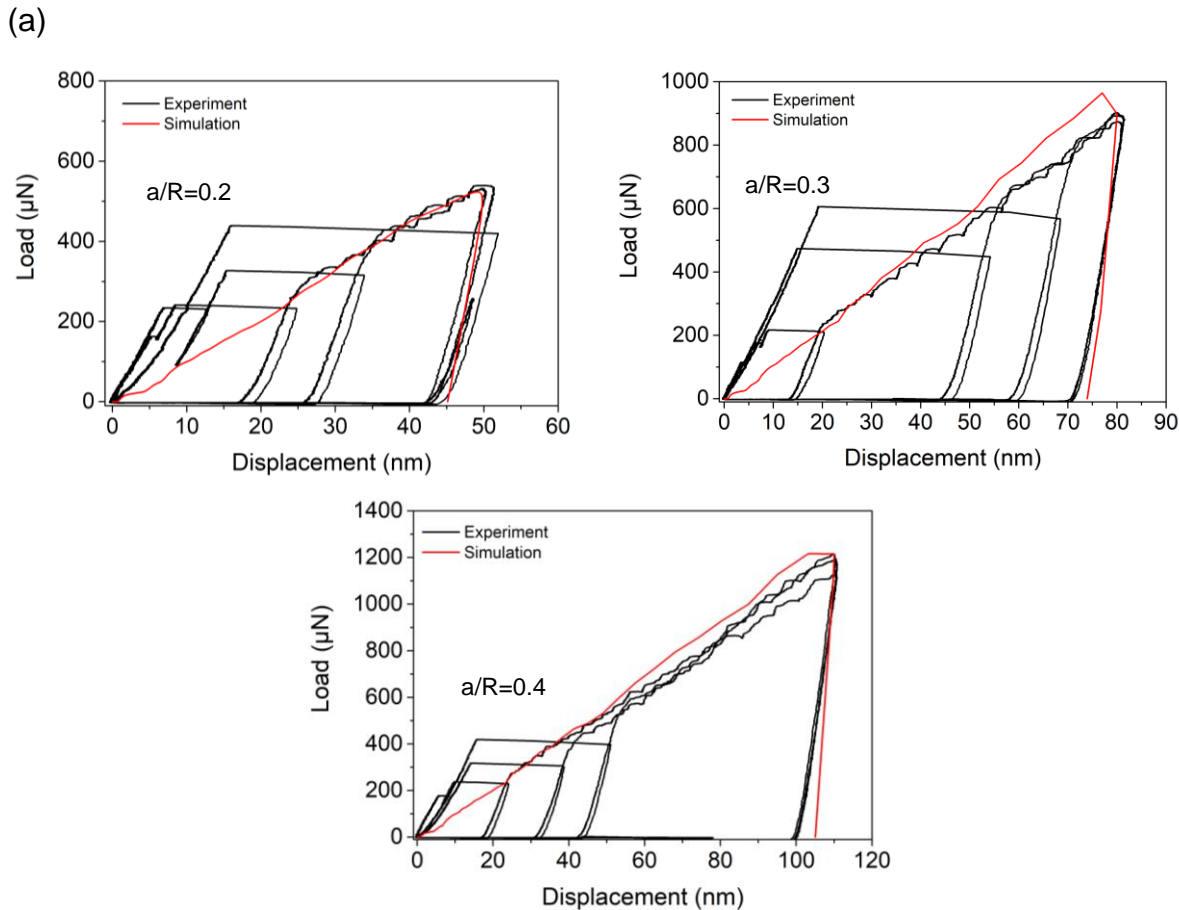


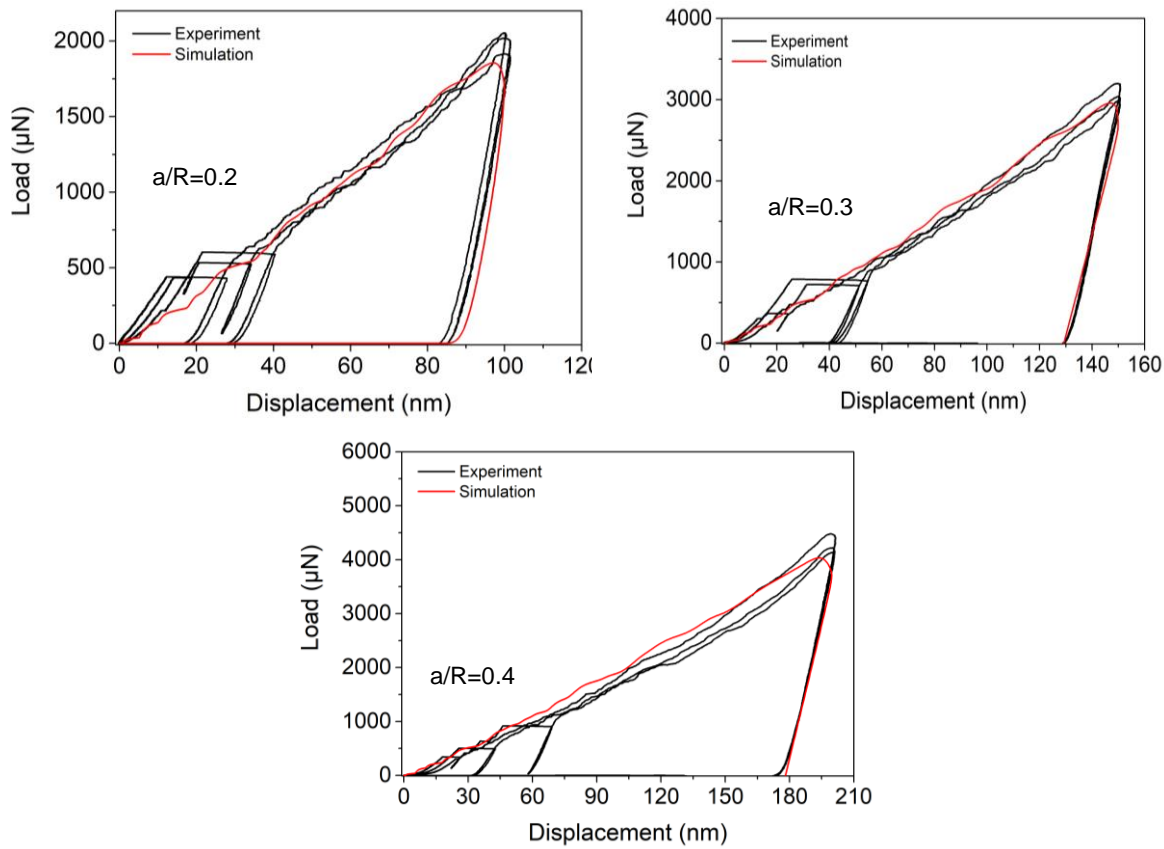
Fig. 6.4 Surface topography and P-H profiles of experimental and simulation results:
 (a) 1 um indenter; (b) 2 um indenter; (c) 5 um indenter; (d) 20 um indenter.
 (Experimental results in solid lines, simulation results in dash lines)

6.2.2 Validation

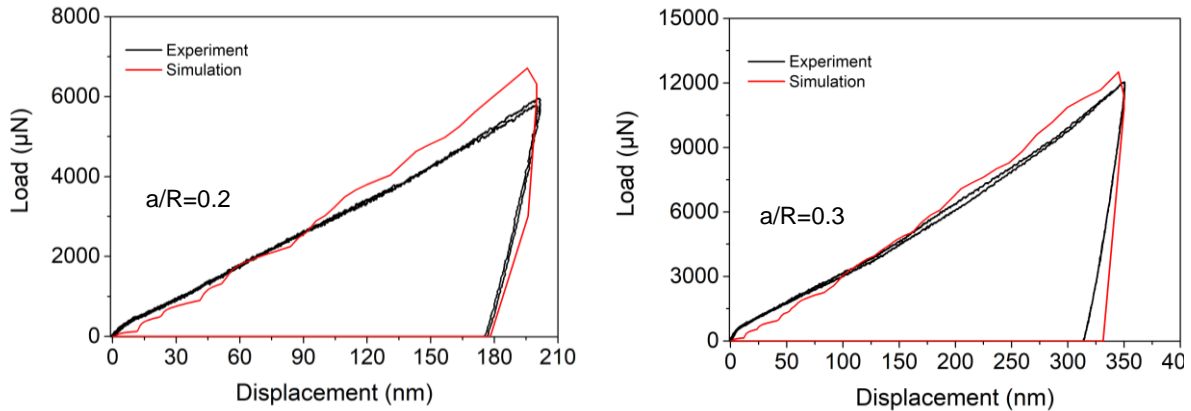
After calibration, the material parameters are applied in the simulation of grain 4200. The comparison of P-H curves and surface topography between experiment and simulation are given in Fig. 6.5 and Fig. 6.6.



(b)



(c)



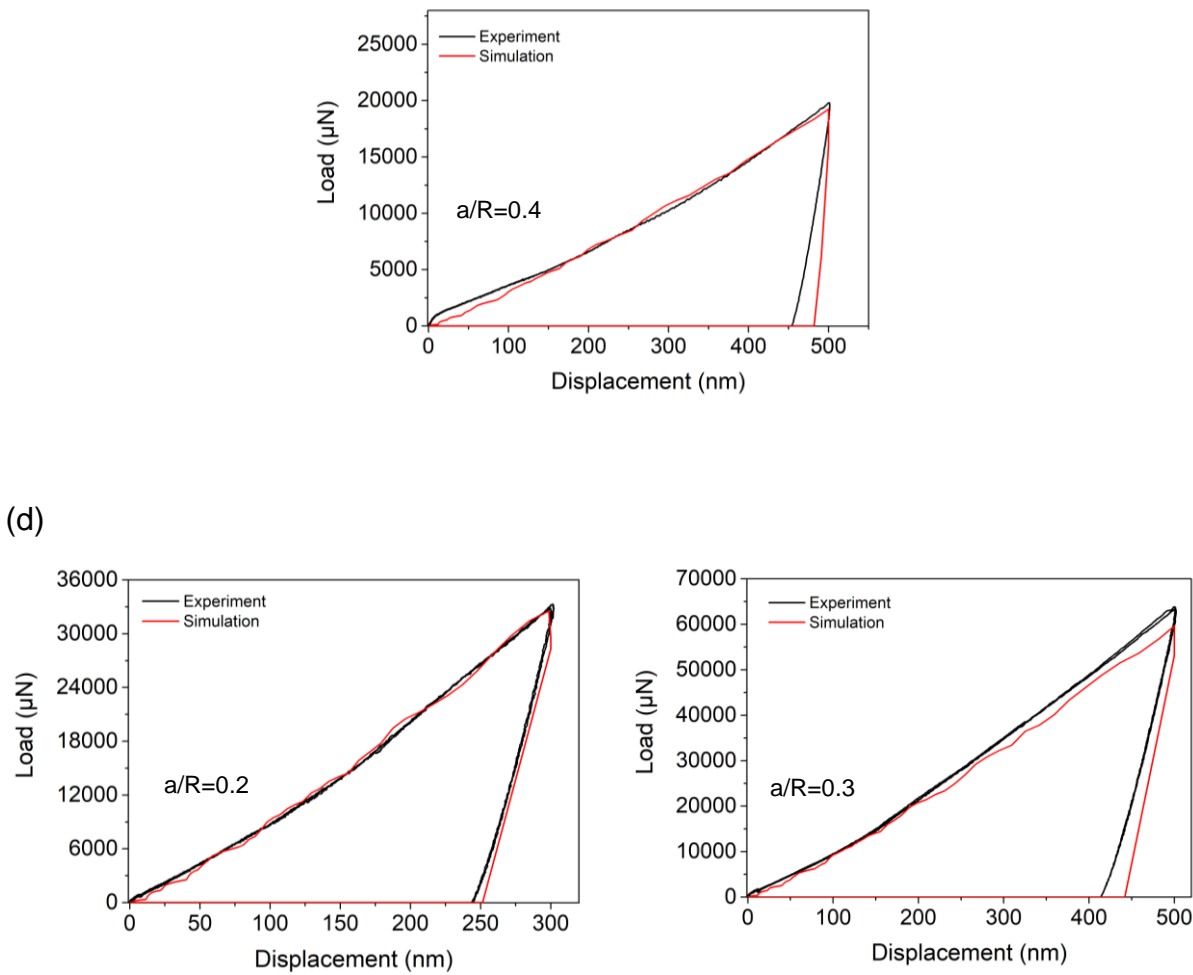
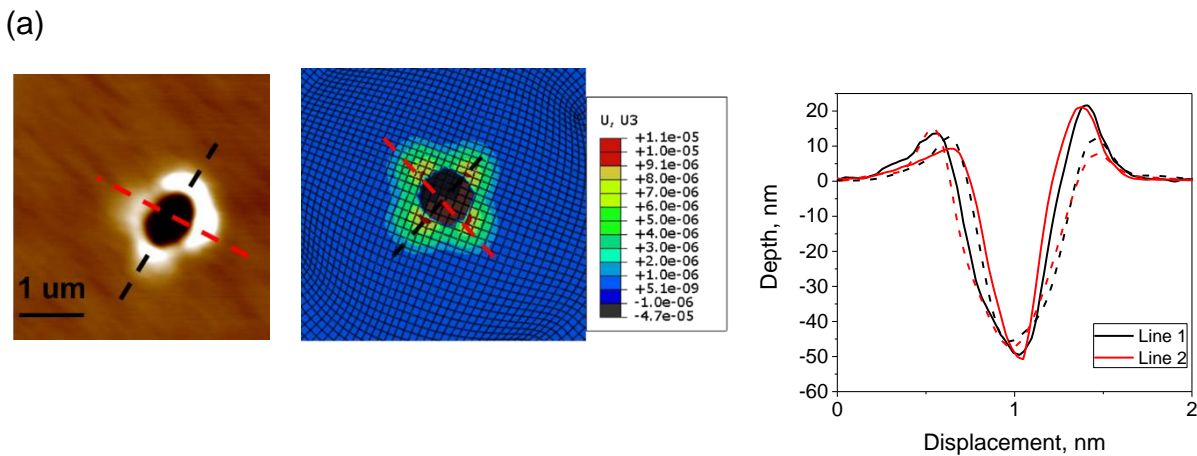
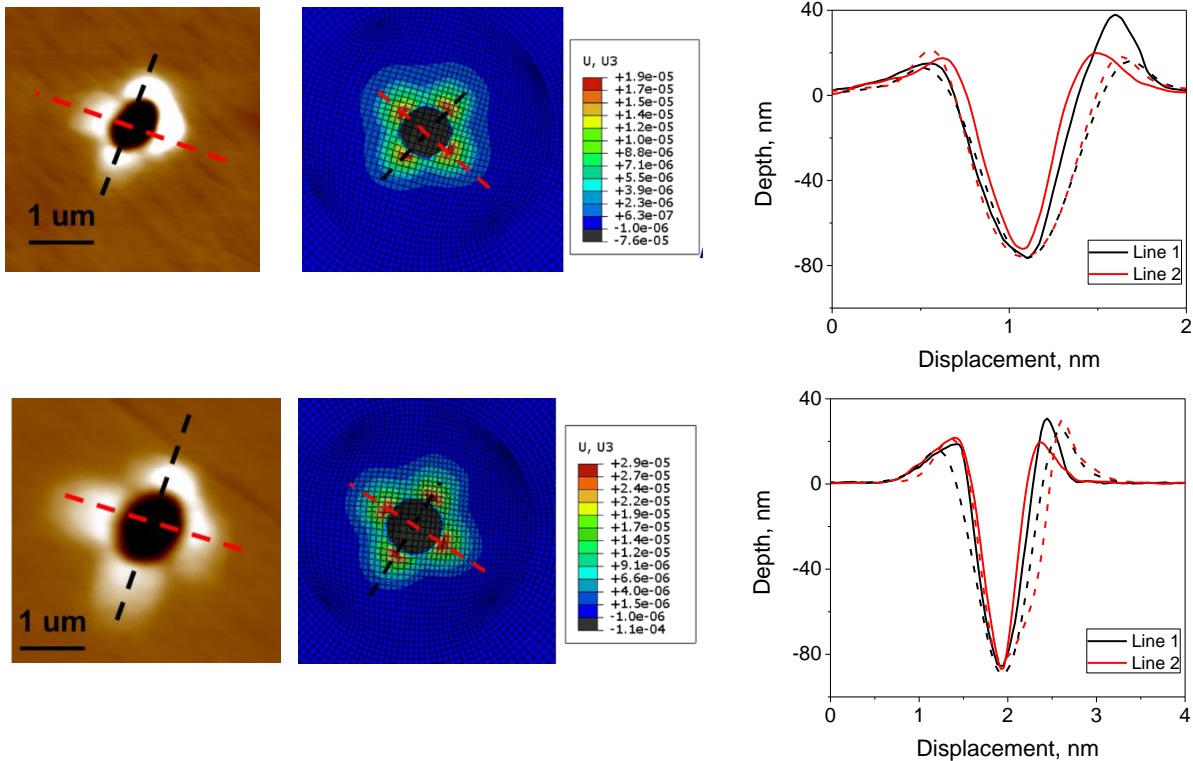
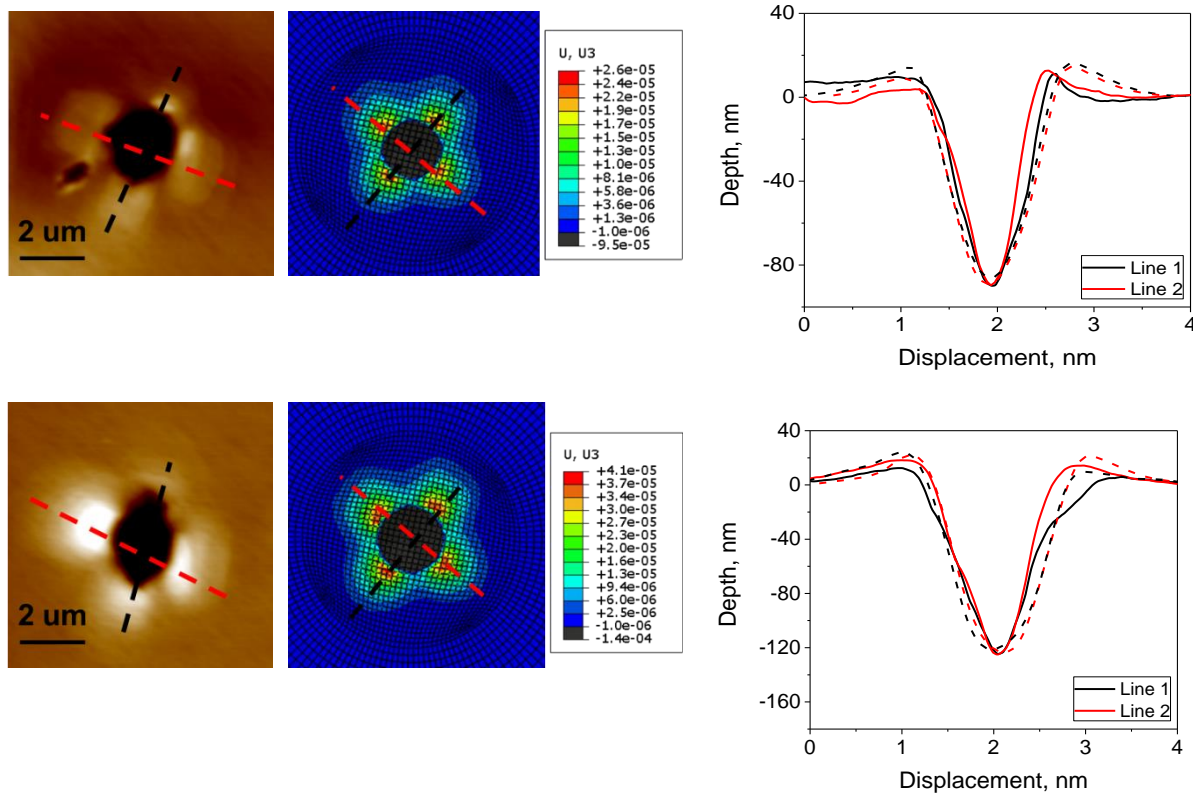


Fig. 6.5 The P-h curves of experiment and simulation of grain 4833: (a) 1 μm indenter; (b) 2 μm indenter; (c) 5 μm indenter; (d) 20 μm indenter.





(b)



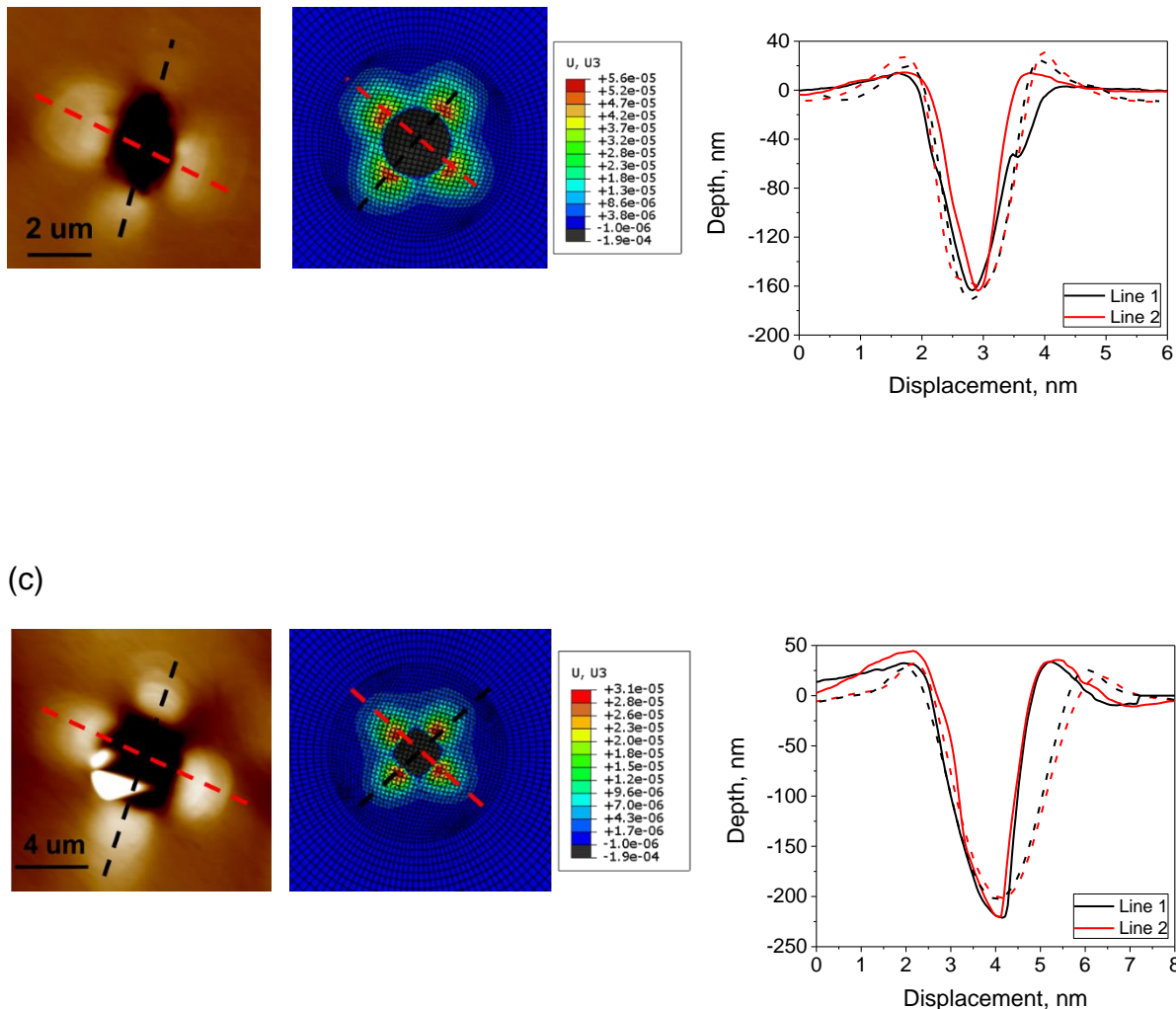


Fig. 6.6 Surface topography and P-H profiles of experimental and simulation results: (a) 1 um indenter; (b) 2 um indenter; (c) 5 um indenter. (Experimental results in solid lines, simulation results in dash lines)

6.2.3 Formulation

According to the calibrated τ_0 value listed in Tab. 6.2, the relationship between the indenter radius and τ_0 is fitted, and the fitted curve is given in Boltzmann model as:

$$\tau_0 = 62 + \frac{148.77287}{1+\exp(R-1.85335)/0.99723} \quad \text{Eq. 6.1}$$

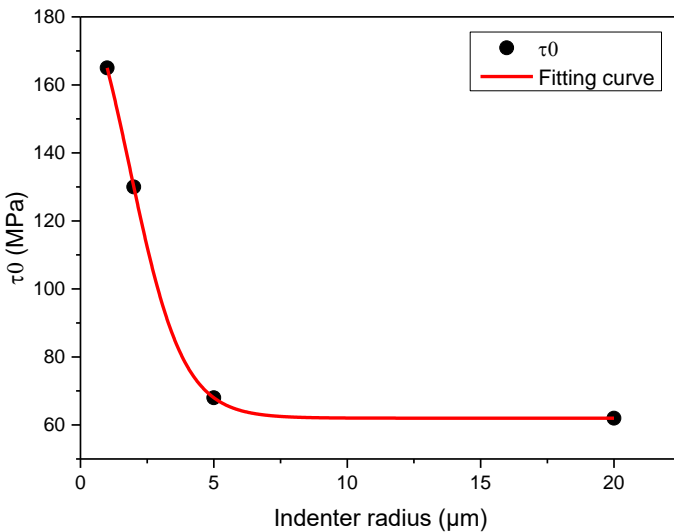


Fig. 6.7 Fitting curve of τ_0 vs Indenter radius.

The fitted curve matches the data point very well, proving the reliability of the formulation. With the formulation, the suitable τ_0 for a spherical indenter with any radius in the range from 1 to 20 μm can be determined. To validate that, nanoindentation tests with indenters of other radii should be performed.

6.3 Non-local model

The nanoindentation model is couple with the non-local crystal plasticity model via a user defined material subroutine (UMAT) within Abaqus. The boundary condition plays an important role in the behavior of the solution of the non-local formulations. In this model, there are mainly two kinds of boundaries conditions given by the non-local plastic strain $\dot{\gamma}$: $\dot{\gamma} = 0$ and $\frac{\partial \dot{\gamma}}{\partial n} = 0$. The first one is called micro-hardness, where the non-local parameters are implemented into the mode. The latter one is called micro-free boundary condition, where the non-local hardening vanishes.

To begin with, the influences of the non-local parameters are studied by varying the parameters. The results are given in Fig. 6.8.

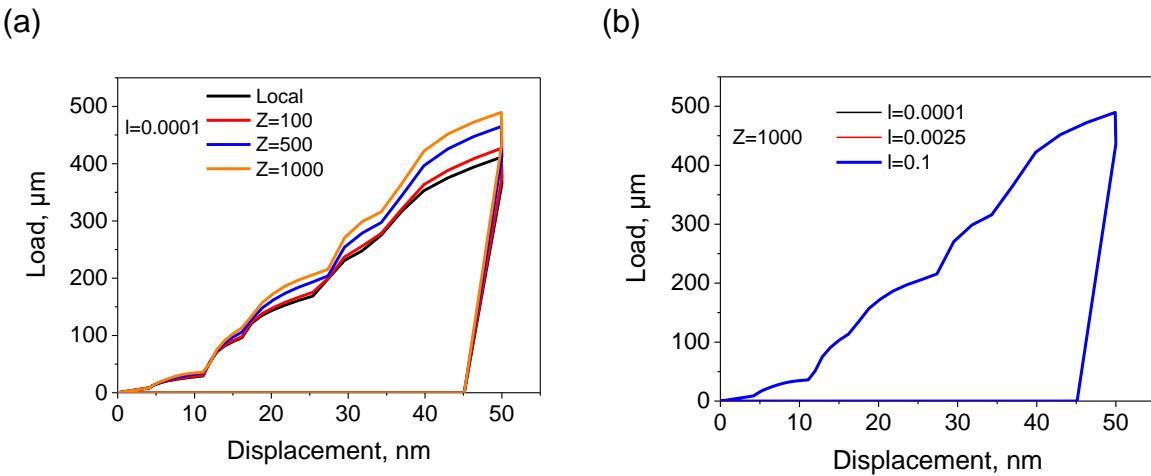


Fig. 6.8 Influence of non-local parameters on the P-H curves with micro-hard boundary conditions.

The stress related parameter Z has an obvious influence on the P-H curves. Higher Z leads to higher load. However, the length scale parameter l has no influence on the results as all the curves overlap with each other. Further study is carried by varying parameters under the micro-free boundary condition. The results (as shown in Fig. 6.9.) reveals the same result as in micro-hardness boundary condition, only Z has an impact while variation of l does not work in the single-crystal nanoindentation simulation.

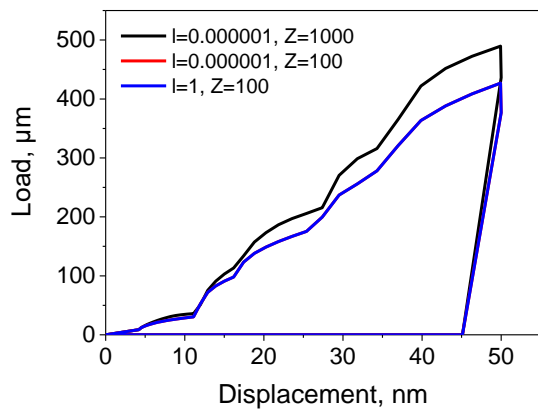


Fig. 6.9 Influence of non-local parameters on the P-H curves with micro-free boundary conditions.

The parameter study above proves the non-local model used here is not suitable for ISE study in nanoindentation tests. The model is principally a phenomenological

constitutive model just like a local model. The non-local part is simply added through an additional stress field controlled by non-local parameters. An internal variable, which related to the plastic strain gradient or dislocation densities, is missing in the constitutive equation. The length parameter ℓ works only in a polycrystal model, where ℓ is expressed by the relationship between the size of the grains and the whole model. The nanoindentation model used here is generated based on a single crystal, which cannot present the function of ℓ . As for Z, it plays the same role as the local parameters in this case, so varying Z leads to different results.

7 Conclusions

In this thesis, the size effect of spherical indenters is studied in experimental and numerical methods. The experiments are performed in a ferritic-stainless steel AISI439 with indenters with the indenter radii of 1, 2, 5 and 20 μm . For each indenter, indentation tests with indentation strain of 0.2, 0.3 and 0.4 are designed. It can be concluded from the experiment results:

- The size effect has been observed in the experiments that the hardness value shows an obvious increase with decreasing indenter radius at the same indentation strain.
- For the same indenter, a decrease of hardness with increasing indentation strain indicates the size effect displays when varying penetration depth as well.
- The size effect is observed in both grains with orientation closed to {111} and {100}. The {111} grain has a higher hardness value than the {100} grain. The pile-up patterns for the {100} and {111} grains are approximately four-fold symmetry.

By coupling the nanoindentation model with a local CPFEM model, the numerical investigation of size effect is performed. The results indicate:

- The simulation results match the experimental results greatly for different indenter by varying the CP parameter τ_0 . The size effect is well captured through the model, which proves τ_0 has a connection with the size effect.
- A relationship between indenter radius and τ_0 is given in a Boltzmann equation. The determination of suitable τ_0 for an indenter whose radius is between 1 to 20 μm from the formulation is possible.

Further works need to be done for a deeper understanding of the size effect that:

- The calibrated parameters should be incorporated into a mesoscale model like the representative volume element for the purpose of validation on micromechanical properties.
- The ISE can only be expressed by adapted material parameters in the local model. A non-local model which is built based on plasticity strain gradient or GNDs should be used for the numerical study.

Appendices

Appendices I : Hardness values of nanoindentation tests.

I.1 Hardness value of grain 4833 and grain 4200.

Indenter	Grain 4833			Grain 4200		
	Indentation strain			Indentation strain		
	0.2	0.3	0.4	0.2	0.3	0.4
1 µm	3.60	3.73	3.21	4.71	3.63	3.73
	4.05	3.62	3.28	4.29	3.98	3.70
	1.93	3.57	3.46	4.17	3.70	3.52
2 µm	3.01	2.59	2.51	2.83	2.63	2.73
	2.76	2.50	2.41	2.80	2.66	2.63
	2.64	2.46	2.38	2.78	2.55	2.67
5 µm	2.19	2.18	2.52	2.17	2.25	1.96
	2.24	2.17	1.90	2.36	2.26	2.30
20 µm	1.97	1.89		2.02	1.99	1.94
	1.95	1.91		2.01	2.00	

Literature

- [1] N. Fleck, G.M. Muller, M. Ashby, J.W. Hutchinson, Strain Gradient Plasticity – Theory and Experiment, *Acta Metallurgica et Materialia*, 42 (1994) 475-487.
- [2] W.D. Nix, H. Gao, Indentation size effects in crystalline materials: A law for strain gradient plasticity, *Journal of the Mechanics and Physics of Solids*, 46(3) (1998) 411-425.
- [3] J.G. Swadener, E.P. George, G.M. Pharr, The correlation of the indentation size effect measured with indenters of various shapes, *Journal of the Mechanics and Physics of Solids*, 50(4) (2002) 681-694.
- [4] Y. Huang, F. Zhang, K.C. Hwang, W.D. Nix, G.M. Pharr, G. Feng, A model of size effects in nano-indentation, *Journal of the Mechanics and Physics of Solids*, 54(8) (2006) 1668-1686.
- [5] C.A. Schuh, Nanoindentation studies of materials, *Materials Today*, 9(5) (2006) 32-40.
- [6] A.C. Fischer, Nanoindentation, 2nd ed., New York, Springer-Verlag, 2004.
- [7] M.S. Technologies, Nano Indenters from MICRO STAR TECHNOLOGIES Huntsville, USA, <https://www.microstartech.com>.
- [8] W.C. Oliver, G.M. Pharr, Measurement of hardness and elastic modulus by instrumented indentation: Advances in understanding and refinements to methodology, *Journal of Materials Research*, 19(1) (2011) 3-20.
- [9] W.C. Oliver, G.M. Pharr, An improved technique for determining hardness and elastic modulus using load and displacement sensing indentation experiments, *Journal of Materials Research*, 7(6) (2011) 1564-1583.
- [10] J. Menčík, Opportunities and problems in nanoindentation with spherical indenters, *Chemicke Listy*, 105 (2011) 680-683.
- [11] L. Ma, L. Levine, R. Dixson, D. Smith, D. Bahr, Effect of the Spherical Indenter Tip Assumption on the Initial Plastic Yield Stress, 1st ed., London, IntechOpen, 2012.

- [12] J.-i. Jang, B.-G. Yoo, J.-Y. Kim, Rate-Dependent Inhomogeneous-to-Homogeneous Transition of Plastic Flows During Nanoindentation of Bulk Metallic Glasses: Fact or Artifact?, *Applied Physics Letters*, 90 (2007) 211906-211906.
- [13] C.A. Schuh, A.C. Lund, Application of nucleation theory to the rate dependence of incipient plasticity during nanoindentation, *Journal of Materials Research*, 19(7) (2011) 2152-2158.
- [14] C. Schuh, J. Mason, A.C. Lund, Quantitative insight into dislocation nucleation from high-temperature nanoindentation experiments, *Nature materials*, 4 (2005) 617-621.
- [15] T.G. Nieh, C. Schuh, J. Wadsworth, Y. Li, Strain rate-dependent deformation in bulk metallic glasses, *Intermetallics*, 10(11) (2002) 1177-1182.
- [16] M. Hardiman, T. Vaughan, C. McCarthy, The effects of pile-up, viscoelasticity and hydrostatic stress on polymer matrix nanoindentation, *Polymer Testing*, 52 (2016) 157-166.
- [17] J. Menčík, Nanoindentation in Materials Science, 1st ed., London, IntechOpen, 2012.
- [18] K.L. Johnson, Contact Mechanics, 1st ed., Cambridge, Cambridge University Press, 1985.
- [19] Bruker GmbH., TI980 TribolIndenter Brochure, Minneapolis, USA, <https://www.bruker.com/products/surface-and-dimensional-analysis/nanomechanical-test-instruments/standalone-nanomechanical-test-instruments/ti-980-triboindenter>.
- [20] E.O. Hall, The Deformation and Ageing of Mild Steel: III Discussion of Results, *Proceedings of the Physical Society. Section B*, 64(9) (1951) 747-753.
- [21] Q. Ma, D.R. Clarke, Size dependent hardness of silver single crystals, *Journal of Materials Research*, 10(4) (2011) 853-863.
- [22] N.A. Stelmashenko, M.G. Walls, L.M. Brown, Y.V. Milman, Microindentations on W and Mo oriented single crystals: An STM study, *Acta Metallurgica et Materialia*, 41(10) (1993) 2855-2865.

- [23] N.A. Fleck, J.W. Hutchinson, A phenomenological theory for strain gradient effects in plasticity, *Journal of the Mechanics and Physics of Solids*, 41(12) (1993) 1825-1857.
- [24] D. Tabor, *The Hardness of Metals*, 1st ed., Oxford, Clarendon Press, 1951.
- [25] Y. Huang, S. Qu, K.C. Hwang, M. Li, H. Gao, A conventional theory of mechanism-based strain gradient plasticity, *International Journal of Plasticity*, 20(4) (2004) 753-782.
- [26] A. Ruiz-Moreno, P. Hähner, Indentation size effects of ferritic/martensitic steels: A comparative experimental and modelling study, *Materials & Design*, 145 (2018) 168-180.
- [27] S. Qu, Y. Huang, G.M. Pharr, K.C. Hwang, The indentation size effect in the spherical indentation of iridium: A study via the conventional theory of mechanism-based strain gradient plasticity, *International Journal of Plasticity*, 22(7) (2006) 1265-1286.
- [28] F. Roters, P. Eisenlohr, L. Hantcherli, D.D. Tjahjanto, T.R. Bieler, D. Raabe, Overview of constitutive laws, kinematics, homogenization and multiscale methods in crystal plasticity finite-element modeling: Theory, experiments, applications, *Acta Materialia*, 58(4) (2010) 1152-1211.
- [29] J.F.W. Bishop, R. Hill, A theory of the plastic distortion of a polycrystalline aggregate under combined stresses, *The London, Edinburgh, and Dublin Philosophical Magazine and Journal of Science*, 42(327) (1951) 414-427.
- [30] J.F.W. Bishop, R. Hill, A theoretical derivation of the plastic properties of a polycrystalline face-centred metal, *The London, Edinburgh, and Dublin Philosophical Magazine and Journal of Science*, 42(334) (1951) 1298-1307.
- [31] G. Gottstein, *Physical Foundations of Materials Science*, 2004 ed., Heidelberg, Springer-Verlag Berlin, 2004.
- [32] F. Roters, P. Eisenlohr, T.R. Bieler, D. Raabe, *Crystal Plasticity Finite Element Methods: in Materials Science and Engineering*, 1st ed., Weinheim, Wiley VCH Verlag, 2010.

- [33] S. Wulfinghoff, Equivalent plastic strain gradient enhancement of single crystal plasticity: Theory and numerics, Royal Society of London Proceedings Series A, 468 (2012) 2682-2703.
- [34] R.A.B. Engelen, M.G.D. Geers, F.P.T. Baaijens, Nonlocal implicit gradient-enhanced elasto-plasticity for the modelling of softening behaviour, International Journal of Plasticity, 19(4) (2003) 403-433.
- [35] R.H.J. Peerlings, M.G.D. Geers, R. de Borst, W.A.M. Brekelmans, A critical comparison of nonlocal and gradient-enhanced softening continua, International Journal of Solids and Structures, 38(44) (2001) 7723-7746.
- [36] J.K. Engels, S. Gao, W. Amin, A. Biswas, A. Kostka, N. Vajragupta, A. Hartmaier, Indentation size effects in spherical nanoindentation analyzed by experiment and non-local crystal plasticity, Materialia, 3 (2018) 21-30.
- [37] A. Ma, A. Hartmaier, On the influence of isotropic and kinematic hardening caused by strain gradients on the deformation behaviour of polycrystals, Philosophical Magazine, 94(2) (2014) 125-140.
- [38] Z. Wang, J. Zhang, H.u. Hassan, J. Zhang, Y. Yan, A. Hartmaier, T. Sun, Coupled effect of crystallographic orientation and indenter geometry on nanoindentation of single crystalline copper, International Journal of Mechanical Sciences, 148 (2018) 531-539.
- [39] C. Reuber, P. Eisenlohr, F. Roters, D. Raabe, Dislocation density distribution around an indent in single-crystalline nickel: Comparing nonlocal crystal plasticity finite-element predictions with experiments, Acta Materialia, 71 (2014) 333-348.
- [40] C. Zambaldi, C. Zehnder, D. Raabe, Orientation dependent deformation by slip and twinning in magnesium during single crystal indentation, Acta Materialia, 91 (2015) 267-288.
- [41] N. Zaafarani, D. Raabe, F. Roters, S. Zaeferer, On the origin of deformation-induced rotation patterns below nanoindents, Acta Materialia, 56(1) (2008) 31-42.
- [42] C.C. Tasan, J.P.M. Hoefnagels, M. Diehl, D. Yan, F. Roters, D. Raabe, Strain localization and damage in dual phase steels investigated by coupled in-situ

deformation experiments and crystal plasticity simulations, International Journal of Plasticity, 63 (2014) 198-210.

[43] O. Engler, V. Randle, Introduction to Texture Analysis: Macrotexuture, Microtexture, and Orientation Mapping, 2nd ed., Boca Raton, CRC Press, 2009.